NUREG/CR-1197
ORNL/NUREG/TM-370

ornl

OAK RIDGE NATIONAL LABORATORY

UNION CARBIDE

Heavy-Section Steel Technology Program Quarterly Progress Report for July-September 1979

G. D. Whitman
R. H. Bryan

Prepared for the U.S. Nuclear Regulatory Commission
Office of Nuclear Regulatory Research
Under Interagency Agreements DOE 40-551-75 and 40-552-75

OPERATED BY
UNION CARBIDE CORPORATION
FOR THE UNITED STATES
DEPARTMENT OF ENERGY

Printed in the United States of America. Available from
National Technical Information Service
U.S. Department of Commerce
5285 Port Royal Road, Springfield, Virginia 22161

Available from

GPO Sales Program
Division of Technical Information and Document Control
U.S. Nuclear Regulatory Commission
Washington, D.C. 20555

NUREG/CR-1197
ORNL/NUREG/TM-370
Dist. Category RF

Contract No. W-7405-eng-26

Engineering Technology Division

HEAVY-SECTION STEEL TECHNOLOGY PROGRAM QUARTERLY PROGRESS REPORT FOR JULY-SEPTEMBER 1979

G. D. Whitman R. H. Bryan

Manuscript Completed – March 18, 1980
Date Published – April 1980

Prepared for the
U.S. Nuclear Regulatory Commission
Office of Nuclear Regulatory Research
Under Interagency Agreements DOE 40-551-75 and 40-552-75

NRC FIN No. B0119

Prepared by the
OAK RIDGE NATIONAL LABORATORY
Oak Ridge, Tennessee 37830
operated by
UNION CARBIDE CORPORATION
for the
DEPARTMENT OF ENERGY

Contents

PREFACE

The Heavy-Section Steel Technology (HSST) Program, which is sponsored by the Nuclear Regulatory Commission (NRC), is an engineering research activity devoted to extending and developing the technology for assessing the margin of safety against fracture of the thick-walled steel pressure vessels used in light-water-cooled nuclear power reactors. The program is being carried out in close cooperation with the nuclear power industry. This report covers HSST work performed in July through September 1979, except for subcontractor contributions which may cover the three-month period ending in August. The work performed by Oak Ridge National Laboratory (ORNL) and by subcontractors is managed by the Engineering Technology Division. Major tasks at ORNL are carried out by the Engineering Technology Division and the Metals and Ceramics Division. Prior progress reports on this program are ORNL-4176, ORNL-4315, ORNL-4377, ORNL-4463, ORNL-4512, ORNL-4590, ORNL-4653, ORNL-4681, ORNL-4764, ORNL-4816, ORNL-4855, ORNL-4918, ORNL-4971, ORNL/TM-4655 (Vol. II), ORNL/TM-4729 (Vol. II), ORNL/TM-4805 (Vol. II), ORNL/TM-4914 (Vol. II), ORNL/TM-5021 (Vol. II), ORNL/TM-5170, ORNL/NUREG/TM-3, ORNL/NUREG/TM-28, ORNL/NUREG/TM-49, ORNL/NUREG/TM-64, ORNL/NUREG/TM-94, ORNL/NUREG/TM-120, ORNL/NUREG/TM-147, ORNL/NUREG/TM-166, ORNL/NUREG/TM-194, ORNL/NUREG/TM-209, ORNL/NUREG/TM-239, NUREG/CR-0476 (ORNL/NUREG/TM-275), NUREG/CR-0656 (ORNL/NUREG/TM-298), NUREG/CR-0818 (ORNL/NUREG/TM-324), and NUREG/CR-0980 (ORNL/NUREG/TM-347).

SUMMARY*

1. PROGRAM ADMINISTRATION AND PROCUREMENT

The Heavy-Section Steel Technology (HSST) Program is an engineering research activity conducted by the Oak Ridge National Laboratory (ORNL) for the Nuclear Regulatory Commission (NRC) in coordination with other research sponsored by the federal government and private organizations. The program comprises studies relating to all areas of the technology of the materials fabricated into thick-section primary-coolant containment systems of light-water-cooled nuclear power reactors. The principal area of investigation is the behavior and structural integrity of steel pressure vessels containing cracklike flaws. Current work is organized into the following tasks: (1) program administration and procurement, (2) fracture mechanics analyses and investigations, (3) effect of high-temperature primary reactor water on the subcritical crack growth of reactor vessel steels, (4) investigations of irradiated materials, (5) pressure vessel investigations, and (6) thermal shock investigations.

The work performed under the existing research and development subcontracts is included in this report.

Fifteen program briefings, reviews, or presentations were made during the quarter.

2. FRACTURE MECHANICS ANALYSES AND INVESTIGATIONS

Several problems of different geometries were run with the NOZ-FLAW computer code automatic mesh generator to verify that this feature produces the mesh parameters correctly. Also, solutions to thermal shock trial problems in cylindrical geometry were found by NOZ-FLAW and compared with solutions obtained independently.

Work was initiated by Materials Research Laboratory (MRL) to establish a standard testing method for determining crack-arrest toughness of pressure vessel steels. A wedge-loaded compact-type specimen has been selected on the basis of a cooperative test program involving about 30 laboratories. Notch preparation and procedures for data reduction will be evaluated in preparation for a round-robin test program involving three types of steel.

3. EFFECT OF HIGH-TEMPERATURE PRIMARY REACTOR WATER ON THE SUBCRITICAL CRACK GROWTH OF REACTOR VESSEL STEELS

Fatigue testing of 13 specimens was completed; 7 specimens were of weld or heat-affected-zone material. Typically, growth rates initially accelerated rapidly and slowed down to remain above the air data scatter band below the upper limit of the scatter band for base metal in a pressurized-water reactor (PWR) environment.

Further investigations of starting effects were made, with comparisons made of tests having different starting ΔK and initial cyclic frequency. A preliminary indication is that starting a test at a high frequency, as a practical matter, is a better way to initiate crack growth than imposing a high starting ΔK. A tentative explanation was developed for the effect of frequency and ΔK during the observed incubation that occurs before environmentally accelerated growth is achieved.

---

*Conversions from SI to English units for all SI quantities are listed on a foldout page at the end of this report.

A test of a large specimen at high ΔK was completed after 18 months. The period of accelerated growth was briefly interrupted only once; however, accelerated growth never resumed. This experience suggests that a different testing procedure needs to be employed to obtain useful data from large specimens on environmentally enhanced crack growth.

4. INVESTIGATIONS OF IRRADIATED MATERIAL

Charpy V-notch impact tests of irradiated and unirradiated specimens of the three welds in the second irradiation series show that the objective of irradiating to an upper-shelf energy of 68 J was attained. The loss of upper-shelf energy is noted to be less than that predicted by Regulatory Guide 1.99. Irradiation parameters for all the specimens in the third irradiation series have been tabulated. The first capsule of the fourth irradiation series was assembled and is being tested.

Fracture properties of irradiated welds 61W, 62W, and 63W were investigated by a J-integral method; welds were from the second HSST 4T irradiation experiment. The irradiation fluence range was 0.7×10^{19} neutrons/cm^2 ($E > 1$ MeV), and the irradiation temperature ranged from 260 to 315° C. Fracture toughness from room temperature to 260° C was evaluated to develop transition through upper-shelf toughness curves for each weld material.

5. PRESSURE VESSEL INVESTIGATIONS

Preliminary plans were made for testing an intermediate vessel with a flaw in low-upper-shelf material. The onset and progression of stable tearing will be observed and compared with predictions by elastic-plastic fracture mechanics. Specifications were written for repair of vessel V-8 and placement of a low toughness weld in the vessel.

Further studies of possible intermediate vessel tests with combined pressure and thermal shock or cyclic thermal loads led to the preliminary conclusion that such tests are feasible.

6. THERMAL SHOCK INVESTIGATIONS

The test cylinder for thermal shock experiment TSE-5 was prepared and tested in the liquid nitrogen facility. The cylinder was tempered at 613° C to obtain the specified toughness value at −18° C. A long axial inside-surface flaw 16 mm deep was prepared by electron-beam welding and hydrogen charging.

The actual thermal shock was somewhat more severe than planned. The crack initiated and arrested three times, attaining depths of 20, 63, and 80% of the wall thickness. Test data indicate that the cylinder toughness at temperatures above 0° C is substantially less than was expected from compact specimen tests.

From post-test analysis, warm prestressing apparently prevented a fourth initiation event, but this is uncertain because the K ratio at the final crack depth is only slightly greater than 1.0. A crack velocity of ~180 m/s was estimated from crack-opening displacement (COD) and ultrasonic test (UT) data. Secondary cracks extending entirely around the cylinder and to both ends apparently originated at a single site on the initial flaw. Some cracks were as deep as 35% of the wall thickness.

HEAVY-SECTION STEEL TECHNOLOGY PROGRAM QUARTERLY PROGRESS REPORT FOR JULY-SEPTEMBER 1979

G. D. Whitman R. H. Bryan

ABSTRACT

The Heavy-Section Steel Technology Program is an engineering research activity conducted by the Oak Ridge National Laboratory for the Nuclear Regulatory Commission. The program comprises studies related to all areas of the technology of the materials fabricated into thick-section primary-coolant containment systems of light-water-cooled nuclear power reactors. The principal area of investigation is the behavior and structural integrity of steel pressure vessels containing cracklike flaws. Current work is organized into six tasks: (1) program administration and procurement, (2) fracture mechanics analyses and investigations, (3) effect of high-temperature primary reactor water on the subcritical crack growth of reactor vessel steels, (4) investigations of irradiated materials, (5) pressure vessel investigations, and (6) thermal shock investigations.

A finite-element computer program for calculating mixed-mode stress-intensity factors for nozzle-corner flaws of arbitrary shape is being checked. A standard crack-arrest toughness testing method is being developed. Charpy impact and J-integral test data were obtained for irradiated weld metal. Preparations for an intermediate vessel test of low-upper-shelf material commenced. The first large-cylinder thermal shock test was performed.

---

1. PROGRAM ADMINISTRATION AND PROCUREMENT

G. D. Whitman

The Heavy-Section Steel Technology (HSST) Program, a major safety program sponsored by the Nuclear Regulatory Commission (NRC), is concerned with the structural integrity of the primary systems (particularly the reactor pressure vessels) of light-water-cooled nuclear power reactor stations. The structural integrity of these vessels is ensured by designing and fabricating them according to standards set by the code for nuclear pressure vessels, by detecting flaws of significant size that occur during fabrication and in service, and by developing methods capable of producing quantitative estimates of conditions under which fractures could occur. The program is concerned mainly with developing pertinent fracture technology, including knowledge of the material used in these thick-walled vessels, the flaw growth rate, and the combination of flaw size and load that would cause fracture and thus limit the life and/or operating conditions for this type of reactor plant.

The program is coordinated with other government agencies and the manufacturing and utility sectors of the nuclear power industry in the United States and abroad. The overall objective is a quantification of safety assessments for regulatory agencies, professional code-writing bodies, and the nuclear power industry. Several activities are conducted under subcontracts by research facilities in the United States and through informal cooperative efforts on an international basis. Five research and development subcontracts are currently in force. These include a subcontract with Materials Research Laboratory (MRL) to work on development of a standard test for measuring a crack-arrest toughness parameter.

Administratively, the program is organized into six tasks, as reflected in this report: (1) program administration and procurement, (2) fracture mechanics analyses and investigations, (3) effect of high-temperature primary water on the subcritical crack growth of reactor vessel steels, (4) investigations of irradiated material, (5) pressure vessel investigations, and (6) thermal shock investigations.

During this quarter, 15 program briefings, reviews, or presentations were made by the HSST staff at technical meetings and at program reviews for the NRC staff or visitors.

2. FRACTURE MECHANICS ANALYSES AND INVESTIGATIONS*

2.1 Computer Program (NOZ-FLAW) for Direct Evaluation of K-Factors for Arbitrarily Shaped Cracks at Pressure Vessel Nozzle Corners†

Satya N. Atluri‡ K. Kathiresan‡

Work continues on the development of a finite-element computer program (NOZ-FLAW) for the calculation of stress-intensity factors along arbitrarily shaped flaw fronts at pressure vessel nozzle corners. A paper describing and presenting results to date from this work was presented at the Fifth International Conference on Structural Mechanics in Reactor Technology, August 13–17, 1979, held in Berlin, Federal Republic of Germany.[1]

2.1.1 Automatic mesh generator for NOZ-FLAW computer program

The mesh generator program, which can generate the appropriate finite-element mesh patterns for analyzing nozzle-corner cracks in boiling-water reactor (BWR) vessels, is now operational in a fully automatic mode. This automatic mesh generation program has been inserted into the main structural analysis program (which contains the special 3-D hybrid crack elements) as a separate overlay. The input for the NOZ-FLAW program simply would be data such as the dimensions of the vessel, the nozzle, description of the crack-front geometry, and the number of elements the user wishes to have in each of the three directions of the grid breakdown. These input data will be explained and illustrated more fully in a detailed user's manual. With the above data as input to the mesh generation overlay of NOZ-FLAW, the vessel-nozzle geometry is automatically converted into a finite-element mesh. In addition, finite-element nodal points, nodal connectivities, and boundary conditions are automatically identified. These are then fed as input data to the main structural analysis program. Thus, if needed, the flexibility of using the main structural analysis program independently (without using the automatic mesh generator) is maintained.

The output from the main NOZ-FLAW program is the solution for stress-intensity factors along the crack front as well as stresses at various points in the structure, as specified by the user. The automatic mesh generation overlay also gives (as its output) the details of the input given to it, along with any parameters assumed by the program by default. In addition, this output also contains details such as the total numbers of finite elements, nodes, and degrees of freedom. If the data supplied to the automatic mesh generator are insufficient, if there is an error in the input data, or if the parameters defined are outside the allowable range, the program automatically prints out an error message with a brief description of the problem encountered; further execution is then stopped. Each error message is assigned a number, and a detailed description of each error message is given in the user manual.

Several problems with different geometries of the structure and crack were tested by generating the finite-element breakdown using the automatic mesh generator. This was done to check whether the program generates the finite-element breakdown, element nodal connectivities, and boundary conditions (displacement, including rigid body mode suppression, and traction boundary conditions)

---

*Conversions from SI to English units for all SI quantities are listed on a foldout page at the end of this report.

†Work sponsored by HSST Program under UCCND Subcontract 7565 between Union Carbide Corporation Nuclear Division and Georgia Institute of Technology.

‡Center for the Advancement of Computational Mechanics, School of Civil Engineering, Georgia Institute of Technology, Atlanta, Ga. 30332.

correctly. All the possible bugs in the program were located and remedied. Checking of the finite-element breakdown was done through an extensive use of the graphics facilities and by manual spot-checking. The structural analysis program can be executed at two different levels: (1) to process all the input data from the mesh generator and prepare the data so the finite-element grid breakdown can be viewed through a graphics facility or (2) to carry out the entire stress analysis and output the solution. Further debugging of the mesh generation overlay is currently under way. Note that the program generates a large number of pages of output if the user chooses to print out the stress-intensity factors along with the displacements and stress solutions in the entire structure. If the user is interested only in the stress-intensity factor solution, such instructions should be included in the input to the automatic mesh generation scheme overlay.

A subroutine that generates the traction boundary conditions has been completed and added to the main program. Some of the traction boundary conditions that may be generated are: application of uniform pressure on surfaces such as the crack surface and vessel wall application of any line loads and equivalent traction boundary conditions to simulate hemispherical caps at the ends of the pressure vessel. Provisions have been made for the user to specify any other special boundary conditions through a special boundary condition command. The program has been designed so that the user may specify stress-free conditions at the (longitudinal) ends of the cylindrical vessel, the condition of zero axial displacements at the ends of the cylinder, or the simulation of end caps at the ends of the cylinder. As mentioned in the previous progress report, the program is also capable of solving thermal shock problems in cylinders where the temperature distribution is specified *a priori*.

The mesh generator is now capable of breaking the structure into finite elements for the following four major categories of problems: (1) plates, (2) plates with through-the-thickness holes, (3) cylinders, and (4) cylinders with nozzles. The program is capable of considering through-the-thickness, corner, surface, and buried cracks. Mathematical or experimentally observed "natural" shapes of the crack front may be considered. Different options for the traction boundary conditions are also provided. Note here that the mesh generated by the present automatic mesh generation program for corner cracks at nozzle pressure vessel junctions is slightly different in the arrangement of elements from that of the semiautomatic version of the program used to solve several BWR nozzle-corner crack problems, as reported in prior progress reports.

2.1.2 Thermal loading capability

The NOZ-FLAW code is presently capable of accepting nodal temperature values for the thermal analysis of a pressure vessel nozzle configuration. It was modified this quarter to also compute the actual temperature distribution due to thermal shock (i.e., the Bessel function solution) for cylindrical pressure vessels only. K_I values were calculated for two different meridional beltline, elliptical, inside surface flaws and for one meridional beltline, semicircular, inside surface flaw in cylindrical vessels subjected to a thermal shock applied at the inside surface. Good agreement was obtained between the calculated values and those obtained by Kobayashi et al.,[2] as evidenced in Figs. 2.1 through 2.3. Note that the "normalized" values shown have a unit of stress because σ_o is a nondimensional stress.

The current version of NOZ-FLAW is operational on a CDC 7600 computer. Next quarter the program will be delivered to Oak Ridge National Laboratory (ORNL) at which time work will begin to make NOZ-FLAW operational on the Union Carbide Corporation Nuclear Division (UCCND) IBM computers.

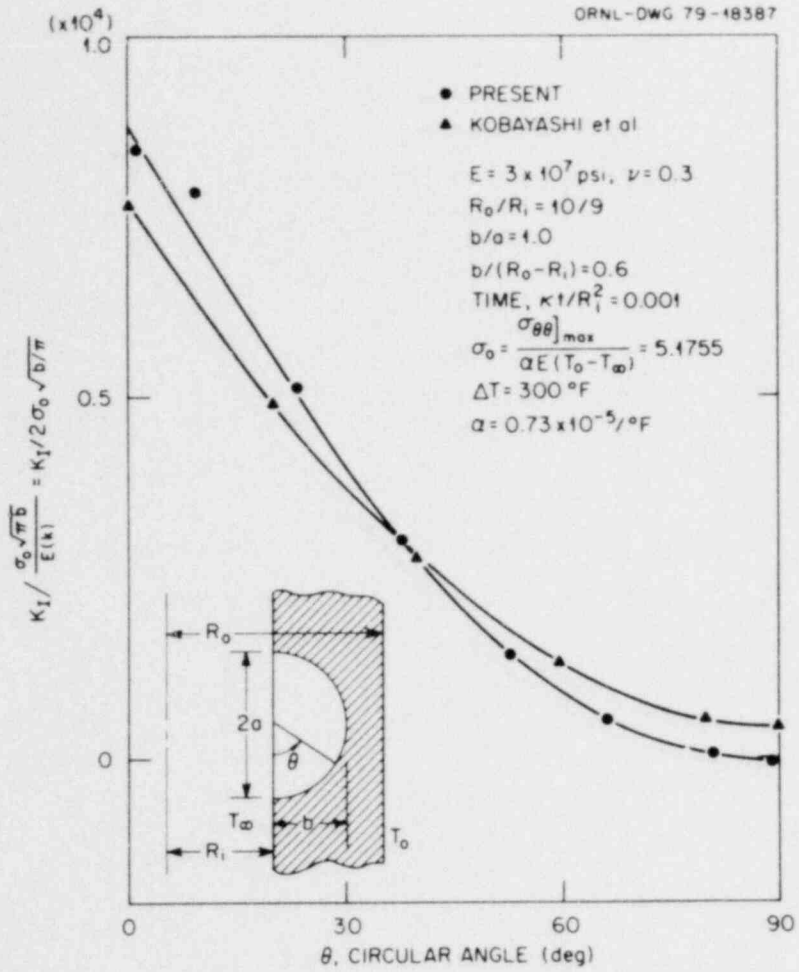

Fig. 2.1. Solution of stress-intensity magnification for a semicircular internal surface flaw in a cylinder subjected to thermal shock [(b/R₀ − Rᵢ) = 0.6; (b/a) = 1.0].

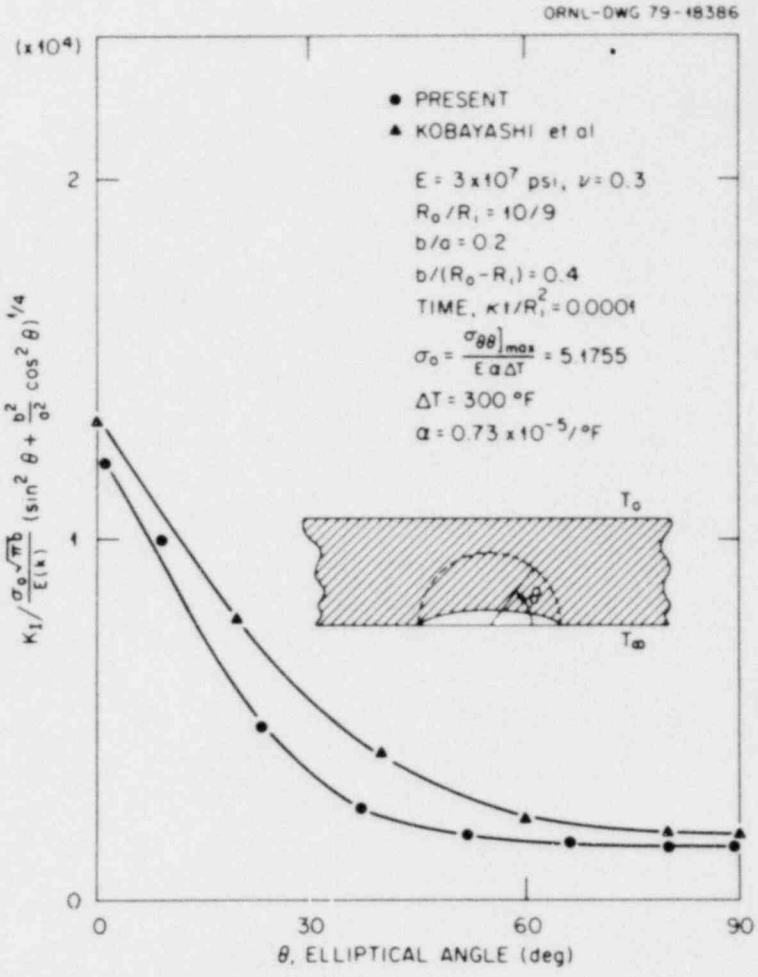

Fig. 2.2. Solution of stress-intensity magnification for a semielliptical internal surface flaw in a cylinder subjected to thermal shock [(b/R₀ − Rᵢ) = 0.4; (b/a) = 0.2].

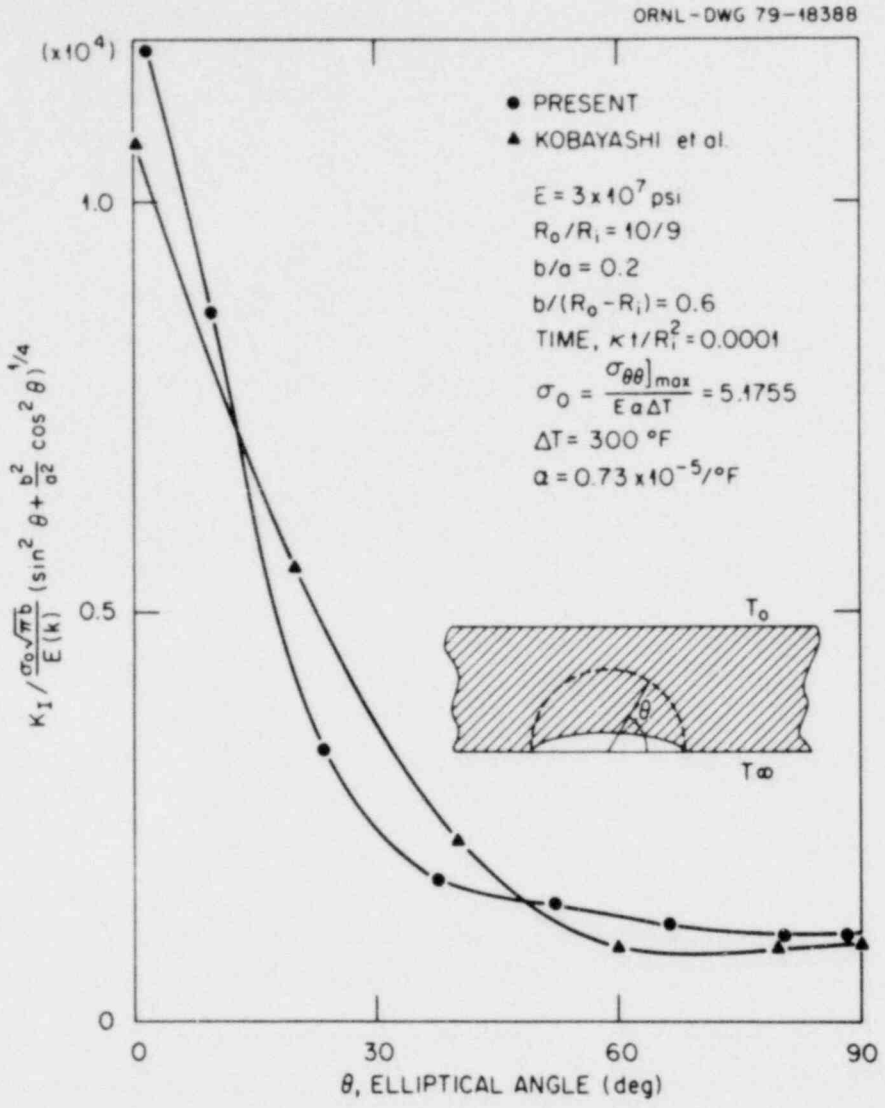

Fig. 2.3. Solution of stress-intensity magnification for a semielliptical internal surface flaw in a cylinder subjected to thermal shock [(b/R$_o$ − R$_i$) = 0.6; (b/a) = 0.2].

2.2 Standard Method of Crack-Arrest Toughness Testing*

P. B. Crosley† E. J. Ripling†

2.2.1 Introduction

The goal of the program being conducted at (MRL) is a standard test method for measuring crack-arrest toughness. The method will employ a wedge-loaded compact specimen based on a design developed at MRL and used recently in a cooperative test program involving some 30 different

*Work sponsored by HSST Program under UCCND subcontract 7755 between Union Carbide Corporation Nuclear Division and Materials Research Laboratory, Inc.

†Materials Research Laboratory, Inc.

laboratories. The standardization effort is being carried out within American Society for Testing and Materials (ASTM) Committee E24 on Fracture Testing; a specific task group in ASTM, E24.01.06, has been charged with setting up and conducting a round-robin test program. Before a round-robin test can be run, more preliminary experiments must be conduc ⁻ to establish test parameters. Conducting such experiments, as well as following through with the round-robin testing, falls within the scope of the MRL program.

2.2.2 Current status

Some ten years ago, Crosley and Ripling began characterizing crack arrest in terms of the parameter K_{Ia}, the stress-intensity factor in the static condition following a run-arrest segment of crack extension.[3] A large number of tests made on HSST Plate 02 with tapered double cantilever beam (TDCB) specimens defined K_{Ia} as a function of temperature for A533 grade B class 1 steel.[4] Tests on electron-beam-welded single-edge notch specimens were in good agreement with the results on TDCB specimens.[5] More recently, a compact test specimen was developed for K_{Ia} testing. Tests made with this specimen gave results in agreement with TDCB results.[6] Measurments of K_{Ia} made on the cooperative test program were also in agreement with earlier results on A533 grade B class 1 steel, and a large body of data showed no dependence of K_{Ia} on test parameters—particularly on the K level at crack initiation preceding the crack arrest—as might be expected if dynamic effects had invalidated the K_{Ia} crack characterization methodology.[7] Thus, the compact K_{Ia} test specimen and test procedure are the starting point for the development of a standard crack-arrest test.

2.2.3 Problem areas

In the specimens provided for the cooperative crack-arrest test program, the crack starter region consisted of a brittle weld deposit with a machined notch. To lower the load required to initiate the crack, the specimens were precompressed. While this two-step method worked well in the cooperative program, it is a cumbersome procedure. Also, some of the success may be because all compact K_{Ia} specimens on the cooperative program were welded and machined at one facility. Further, the amount of precompression required to produce a crack initiation load in the desired range must be determined experimentally for each material. Thus, simplifying the crack starter preparation by eliminating the brittle welding step or the precompression step or both would be extremely desirable. It may be that some (but not all) materials will allow a streamlining of the crack preparation procedure. The possibility of using simpler procedures for candidate materials for the round-robin test program will be studied experimentally.

The formulas previously used for calculating K_{Ia} from displacement and crack length measurements made in a K_{Ia} test were based on analytical results for configurations somewhat different from the compact K_{Ia} specimen. Analysis results for geometries closer to the wedge-loaded compact K_{Ia} specimen should be consulted and an experimental calibration based on a shape identical to the test specimen should be carried out. More accurate calibration results are not likely to result in values of K_{Ia} significantly different from the older formulas. However, the results of the cooperative test program have been called into question on the basis of putative inaccuracies in the expressions used to reduce test data. An experimental calibration of the K_{Ia} compact specimen, therefore, is being carried out, and analytical expressions that appear most relevant will be reviewed in terms of the experimental results.

2.2.4 Round-robin test program

In the cooperative crack-arrest test program, two materials were tested—AISI 1018 steel and SA533 grade B class 1 steel. The former material was included only to give the participants some experience with the test procedure before the material of interest, the pressure vessel steel, was used. All the 30 participants had an interest in nuclear pressure vessels. A standard test method should apply to more than one class of material and should be of interest to a wider technical community. The round-robin program, which will underlie the development of a standard crack-arrest test method, will include a pressure vessel steel material, SA533 grade B class 1. In addition, the structural steels, A36 and A514, will be tested. Arrangements for obtaining the test materials are being made. Participants in the cooperative test program have been invited to take part in the round-robin program, and others who may have an interest in crack-arrest characterization of the pressure vessel steels or the structural steels have also been contacted. At present, ~30 laboratories apparently will participate in the round-robin program.

References

1. S. N. Atluri and K. Kathiresan, "Stress Intensity Factor Solutions for Arbitrarily Shaped Flaws in Reactor Pressure Vessel Nozzle Corners," paper G4/6 presented at the Fifth Conference on Structural Mechanics in Reactor Technology, West Berlin, Federal Republic of Germany, August 1979.

2. A. S. Kobayashi et al., "Surface Flaw in a Pressurized and Thermally-Shocked Hollow Cylinder," *Int. J. Pressure Vessels and Piping*, **5**, 103–22 (1977).

3. P. B. Crosley and E. J. Ripling, "Dynamic Fracture Toughness of A533 Steel," *J. Basic Eng.*, **91** (Series D, No. 3), 525 (September 1969).

4. P. B. Crosley and E. J. Ripling, "Crack Arrest Toughness of Pressure Vessel Steels," *Nucl. Eng. Des.* **17**, 32–45 (1971).

5. P. B. Crosley and E. J. Ripling, "Crack Arrest in an Increasing K-Field," *Proceedings of the Second International Conference on Pressure Vessel Technology, Part II, Materials Fabrication and Inspection, San Antonio, Texas, October 1–4*, 1973, ASME, p. 995.

6. P. B. Crosley and E. J. Ripling, "Significance of Crack Arrest Toughness (K_{Ia}) Testing," paper presented at the ASTM Symposium on Crack Arrest Methodology and Applications, Philadelphia, Pa., November 6–7, 1978.

7. P. B. Crosley and E. J. Ripling, "Comparison of Crack Arrest Methodologies," paper presented at the ASTM Symposium on Crack Arrest Methodology and Application, Philadelphia, Pa., November 6–7, 1978.

3. EFFECT OF HIGH-TEMPERATURE PRIMARY REACTOR WATER ON THE SUBCRITICAL CRACK GROWTH OF REACTOR VESSEL STEELS*†

W. H. Bamford‡
D. M. Moon‡ L. J. Ceschini‡

The objective of this continuing program is to characterize the fatigue crack growth rate properties of ferritic vessel steels exposed to pressurized-water reactor (PWR) primary coolant environments. Four environmental chambers are being used, and the following areas are being investigated:

Weld and heat-affected-zone materials, starting conditions (2T-WOL, 2T CT specimens)	3 chambers (14 MPa, 288°C)
Crack growth rate at high K (4T-WOL, 4T CT specimens)	1 chamber (14 MPa, 288°C)

During this report period, 13 specimens were completed, including the 101.6-mm-thick specimen recently completed at an R ratio equal to 0.7. Considerable progress was made in characterizing weld and heat-affected-zone (HAZ) behavior, as well as the mechanisms of environmental enhancement as they affect starting conditions. This is the last report to be presented under this cover because the contract has expired with this report period. The work will be continued under subcontract to the Naval Research Laboratory and will be reported as a chapter in their progress reports titled *Structural Integrity of Water Reactor Pressure Boundary Components*, edited by F. J. Loss.

3.1 Crack Growth Rate Behavior of Welds and Heat-Affected Zones

Tests of seven additional weld and HAZ specimens were completed during this report period, which doubled the number of specimens of these materials tested thus far. A summary of all specimens now completed, along with conditions of testing, is provided in Table 3.1. Individual plots of the results for each of the specimens tested are provided in Appendix A.

Results have now been obtained for two pressure vessel weld materials as well as for the associated HAZs. The first class of welds studied was made with a Linde 124 flux, typical of welds made in SA533 grade B class 1 plate. The second class of welds was made with a Linde 80 flux, typical of that often used in SA508 class 2 forging material prior to 1977.

A summary of the test results obtained for the Linde 124 weld and HAZ at R (K_{min}/K_{max}) = 0.7 is provided in Fig. 3.1. As seen from Fig. 3.1, crack growth is very difficult to sustain in welds at high R ratio. In all of the tests except specimen C10 and the HAZ specimen, crack growth could not be sustained at rates greater than 5×10^{-4} mm/cycle. Study of the individual test results in Appendix A reveals that the growth rate increases at the beginning of the test but then seems to slow down before increasing steeply again, giving a seesaw or saw-tooth effect. Specimen C10 shows a similar increasing-decreasing effect, but the changes are more gradual. In this specimen, the crack began to grow quickly almost immediately at the start of the test. The growth rate then slowed down and finally increased

*Conversions from SI to English units for all SI quantities are listed on a foldout page at the end of this report.

†Work sponsored by HSST Program under UCCND Subcontract 3290 between Union Carbide Corporation Nuclear Division and Westinghouse Electric Corporation.

‡Westinghouse Electric Corporation.

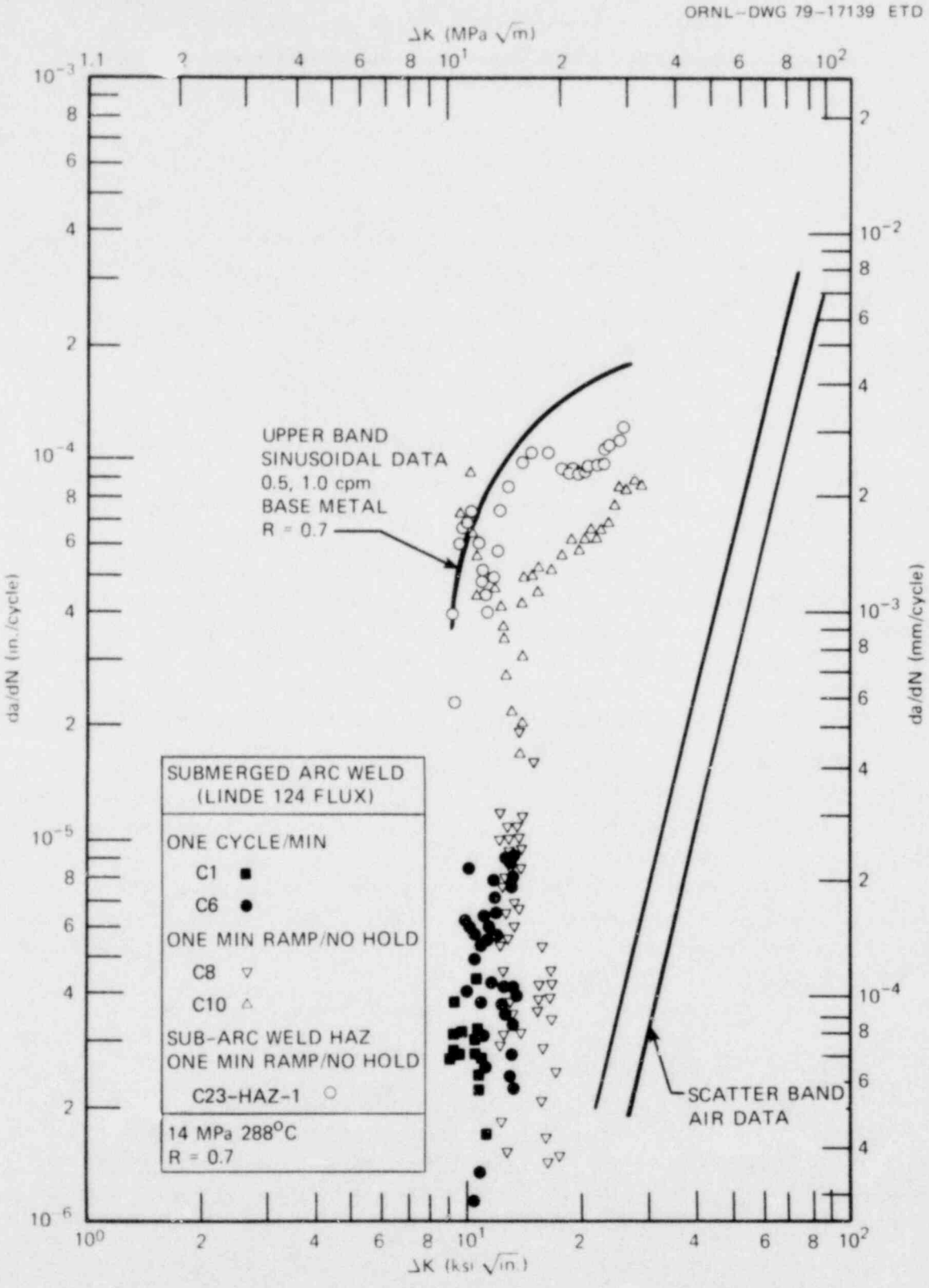

Fig. 3.1 Summary of behavior at high R ratio; Linde 124 weld and HAZ.

Table 3.1. Test specimens from welds and HAZs

Material	Test conditions			
	R = 0.2		R = 0.7	
	One cycle per min	1-min ramp no hold	One cycle per min	1-min ramp no hold
Linde 124 weld	C2 (2T-WOL) C3 (2T-WOL)	C7 (2T-WOL) C9 (2T-WOL)	C1 (2T-WOL) C6 (2T-WOL)	C8 (2T-WOL) C10 (2T-WOL)
Linde 124 weld HAZ (in A533 grade B class 1 plate)		C24 HAZ-1 (2T CT)		C23 HAZ-1 (2T CT)
Linde 80 weld	C3 WLD (2T CT)	C1 WLD (2T CT)		C2 WLD (2T CT)
Linde 80 weld HAZ (in A508 class 2 forging)		C1 HAZ (2T CT)		

again gradually as the test reached a conclusion. A significant difference between test C10 and the other three welds is that the others all tended to reach a maximum value of growth rate, after which the rate slowed down. This maximum value of growth rate did not increase with ΔK, as most of the base metal specimens do. Behavior such as this results in very long test times. For example, specimen C8 was tested for four months (138,000 cycles), and the crack grew 18.3 mm, while specimen C10 was tested for only about six weeks (44,000 cycles) and the crack grew 48 mm, almost three times as much. There were no known differences between the specimens or the test methods used, so the conclusion reached from these results is that cracks generally are exceedingly difficult to propagate in this type of weld at high R ratio.

The behavior of the HAZ specimen was slightly more like the behavior of base metal specimens, as denoted by the line in the figure. Arrests also occurred in the HAZ specimen, but they were milder than those in the weld specimens.

For completeness, a summary of crack growth rate results for this same Linde 124 weld at a low R ratio is provided in Fig. 3.2. These results were presented in the previous report[1] and show a different overall behavior. At low R ratio, the weld specimens and the HAZ specimen behaved similarly to the base metal specimens, with only minor arrest events occurring.

Results of the tests completed to date on Linde 80 weld and HAZ specimens tested at low R ratio are shown in Fig. 3.3, which shows that the behavior of these welds is different from the Linde 124 welds at the same R ratio because each of the weld specimens and the single HAZ specimen show an arrest in the growth rate that occurs within the same range of applied ΔK values. Figure 3.3 indicates that the specimens all begin propagating almost immediately at the beginning of the test, and each specimen then begins to arrest shortly after, with the growth rate behavior tending to revert to air crack growth rates. Two specimens, C1 WLD and C1 HAZ, revert to air crack growth rate behavior almost immediately, while specimen C3 WLD continues accelerated crack growth for a much longer period of time and length of cracking.

The HAZ specimen behavior is nearly identical to that of one weld specimen tested, as seen in Fig. 3.3. This behavior is in marked contrast to that of the HAZ specimen from the plate material, which showed only very mild arrest events, as seen more clearly in Fig. 3.4. The HAZ specimen from the plate (C24 weld HAZ-1) gradually reverts to the air behavior but only at a high value of applied ΔK. The

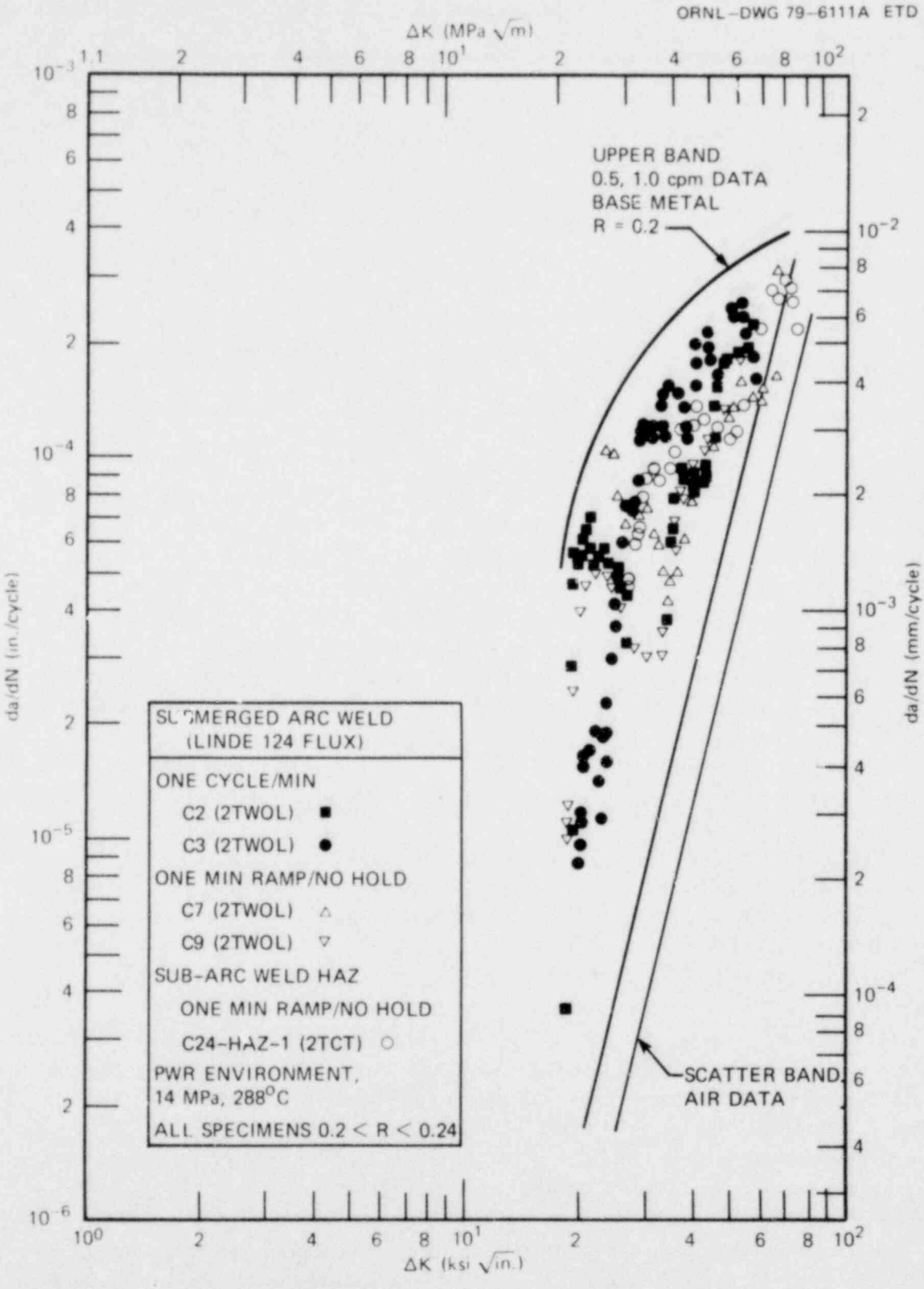

Fig. 3.2. Summary of fatigue crack growth rate results; Linde 124 welds tested at low R ratio.

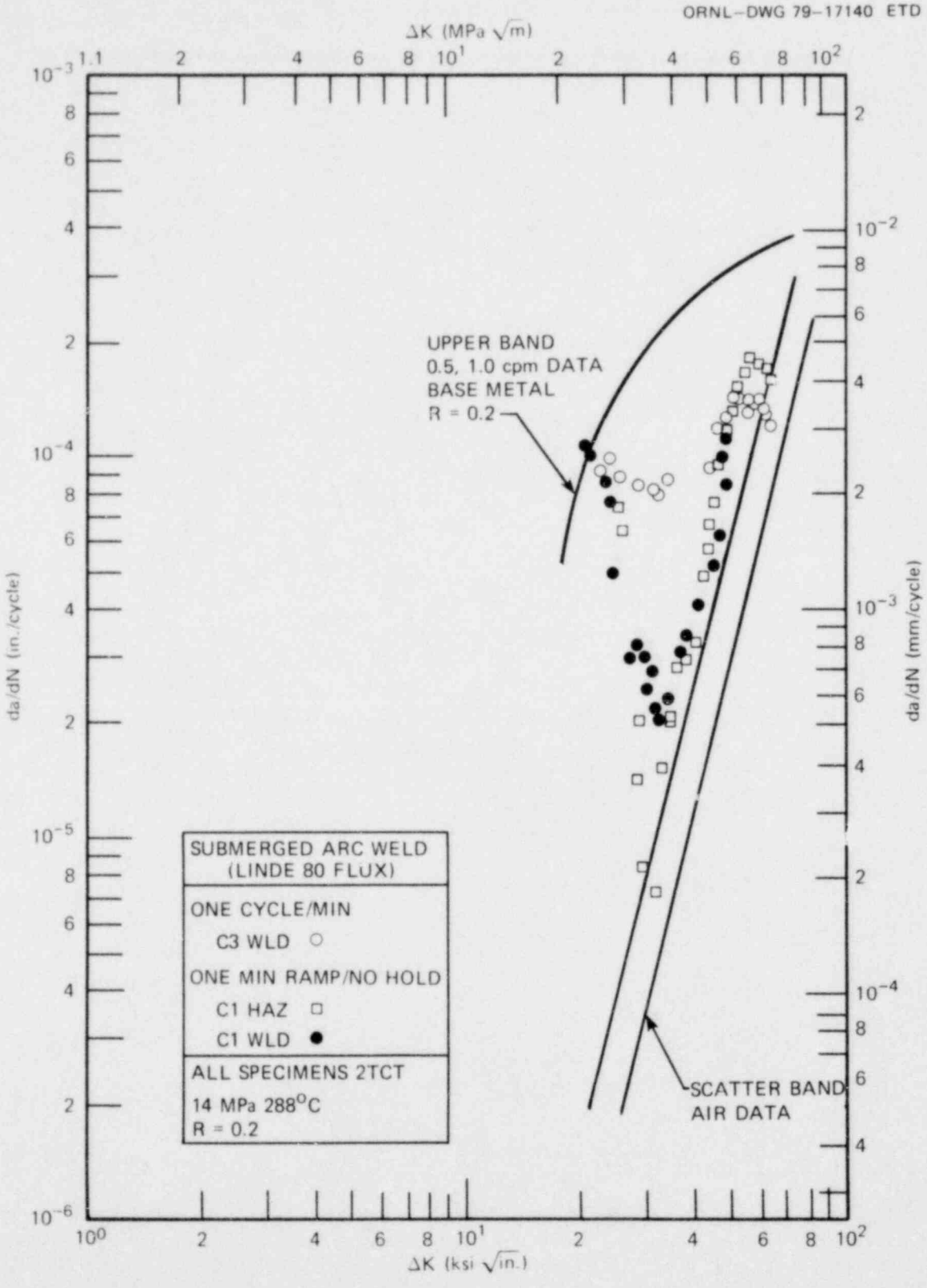

Fig. 3.3. Summary of fatigue crack growth rate behavior at low R ratio; Linde 80 welds.

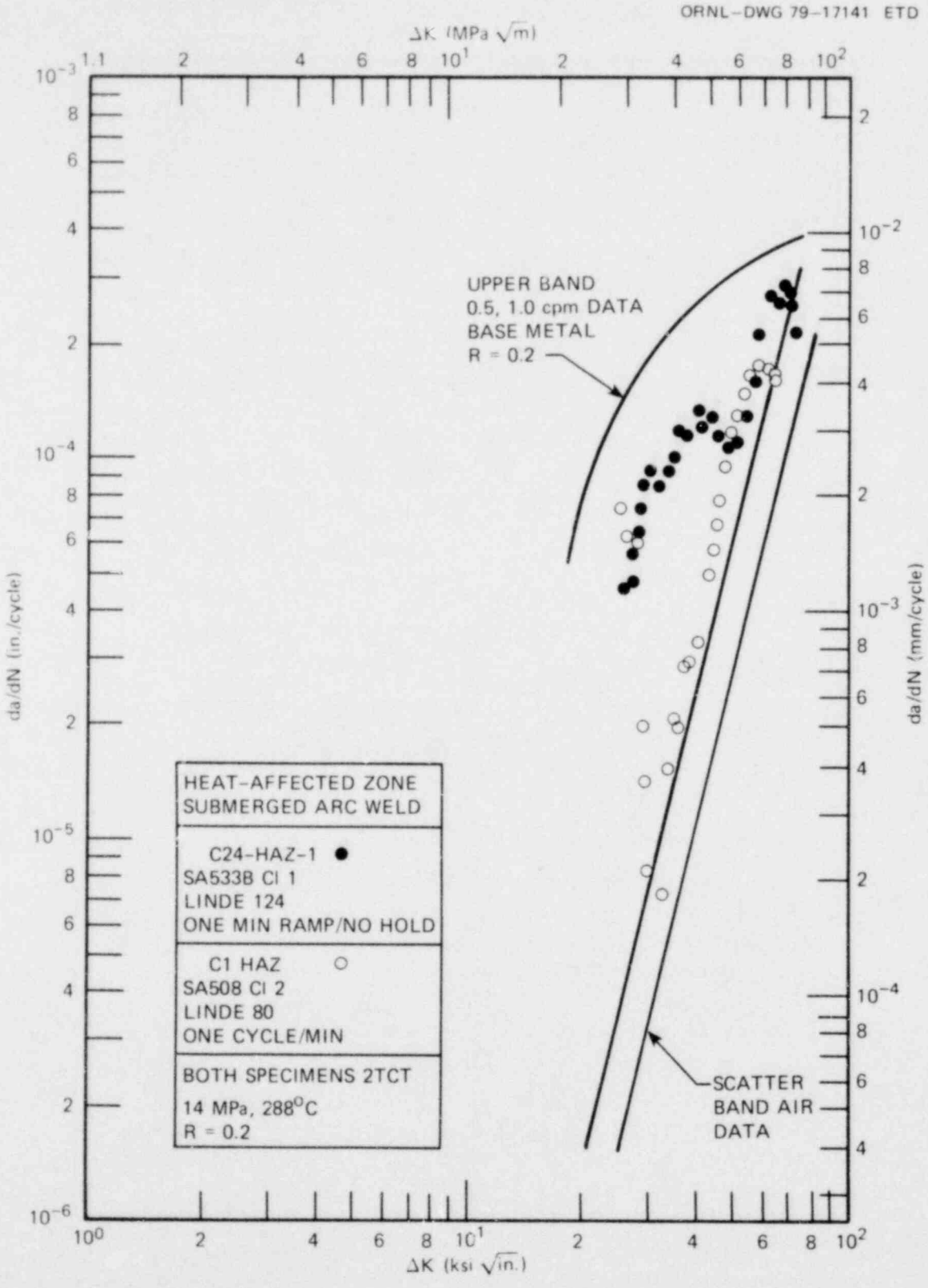

Fig. 3.4. Comparison of plate and forging HAZ behavior.

majority of its test life is spent in accelerated growth; this is compared with the forging HAZ specimen, C1 HAZ, the majority of whose life is spent in nonaccelerated growth.

Figure 3.5 presents the results of the first tests completed on a specimen of Linde 80 weld at high R ratio (0.7). Again, note that the crack growth rate accelerated very quickly to a significant rate without a significant incubation period, which was seen in the Linde 124 weld specimens and in all the base metal specimens tested. This same behavior was noted on the Linde 80 weld specimens tested at R = 0.2, as shown in Fig. 3.3. Another similarity noted at both values of R ratio is that an arrest event of some significance began almost immediately in the test. In the high R ratio specimen, the arrest was not as severe, but it was certainly significant. Further study is in progress on these weld and HAZ materials, and we hope that the blocks of Table 3.1 eventually will each be filled with at least two tests. A reasonable number of tests apparently must be completed on each weld to fully characterize the behavior.

A study has been made of the fracture surfaces of the two types of welds after corrosion-fatigue crack growth testing, and examples of the surfaces of two representative welds are shown in Fig. 3.6. Note that there is no major difference between the two fracture surfaces shown. Both are a mixture of striations and dimples, which result from void nucleation and growth. The fracture surfaces of HAZ specimens from the two types of welds are shown in Fig. 3.7. All specimens were tested with the R ratio = 0.2, and, again, no major difference is evident in this figure. The HAZ specimens show behavior that is more like the base metal than the weld because few dimples are apparent; earlier studies of the base metal fracture surfaces have shown virtually all of the fracture surfaces to be striated.[2]

3.2 Mechanisms of Growth—Starting Effects

Previous test results showed that the fatigue crack growth rate results can be affected significantly by the starting conditions of the test. If the specimen is initially loaded at a relatively high value of ΔK (or K_{max}), then the mechanically induced crack growth rate is faster than can be influenced by the environment, and no environmental enhancement is observed. In the reactor water environment, the observation is that this lack of environmental influence can be continued throughout the test, with no enhanced condition ever being attained.[2]

A series of tests was conducted during this report period to investigate these effects and try to quantify some of the reasons for their occurrence. Results of this test series are indicated in Fig. 3.8. A single heat of A533 grade B class 1 steel was used, and all the tests shown were done at an R ratio = 0.2 in a PWR environment. A number of interesting results were obtained. First, consider a specimen (04A103) tested earlier in the standard manner starting at $\Delta K = 22\ MPa\cdot\sqrt{m}$ and tested at 1 cycle/min and another specimen (04AE13) tested at the same rate and starting at $\Delta K = 35.2\ MPa\cdot\sqrt{m}$. Specimen 04A103 shows typical crack growth behavior accelerated by the environment, while specimen 04AE13 shows almost no environmental acceleration, with the latter data lying along a line parallel to the air behavior data represented by the straight lines in the figure.

Results of three other tests are shown in Fig. 3.8, and these were all done with a combination of 60-cycles/min and 1-cycle/min loadings. The purpose of these three tests was to investigate the possibility of "conditioning" the crack tip by propagating the crack at a high cyclic rate and then slowing the test to let the environment influence the crack. There were two purposes for this series of experiments: to further study the mechanisms of environmental enhancement and to find out if another method could be found to speed up the often lengthy tests. The tests were successful in both respects.

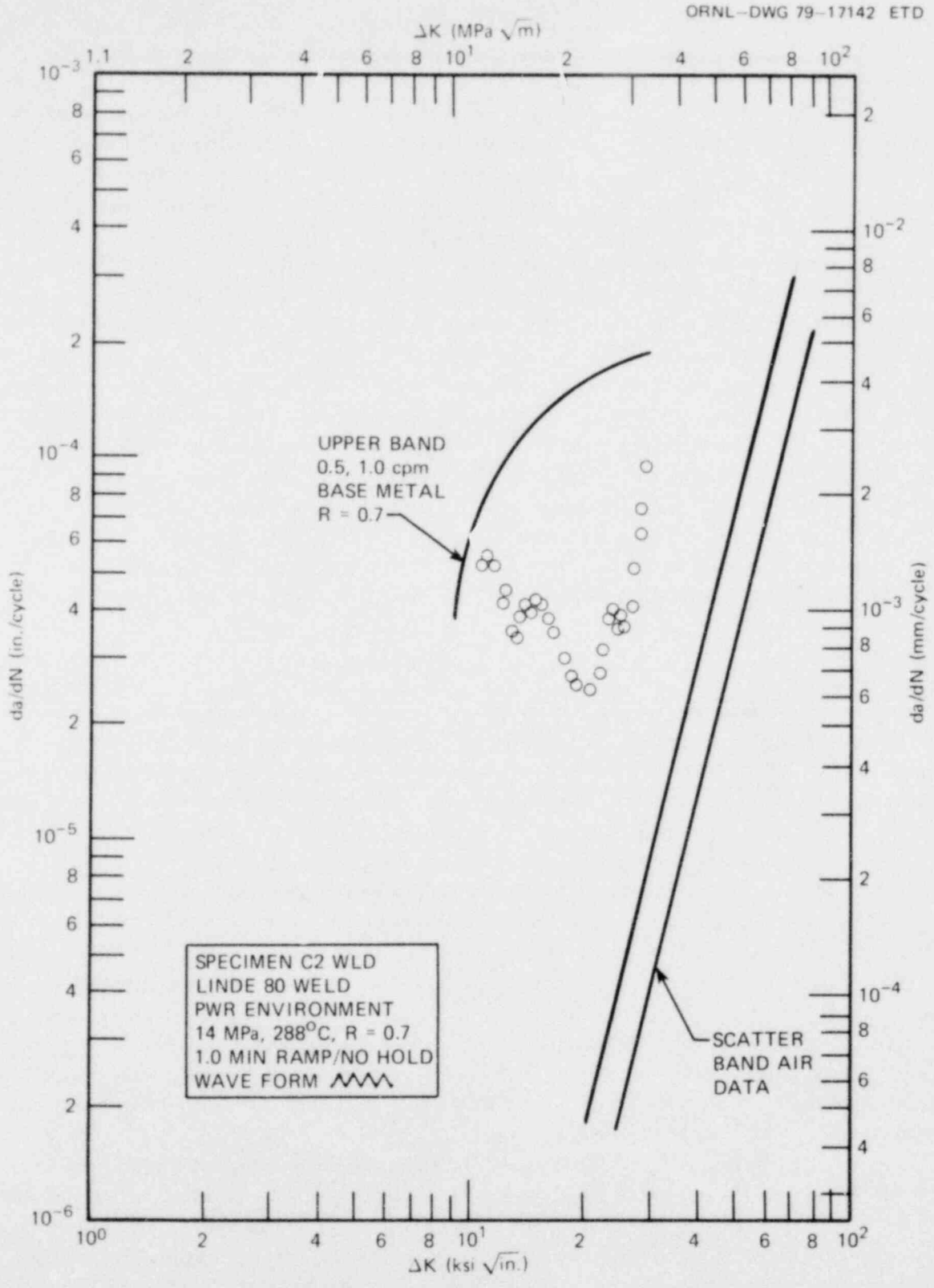

Fig. 3.5. Fatigue crack growth rate behavior at high R ratio; Linde 80 weld.

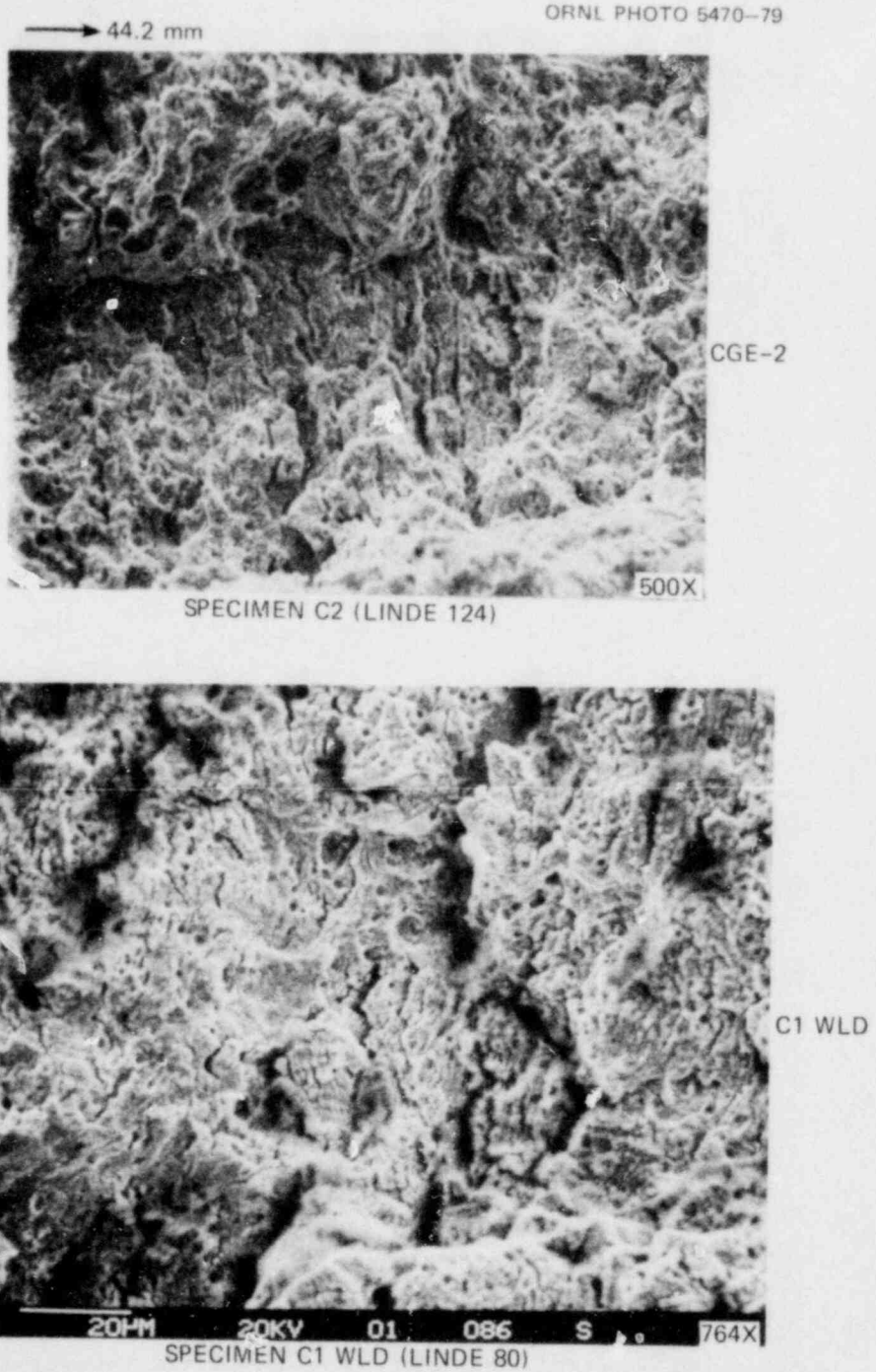

Fig. 3.6. Comparison of fracture surfaces; Linde 124 vs Linde 80 welds; R = 0.2.

ORNL PHOTO 5471-79

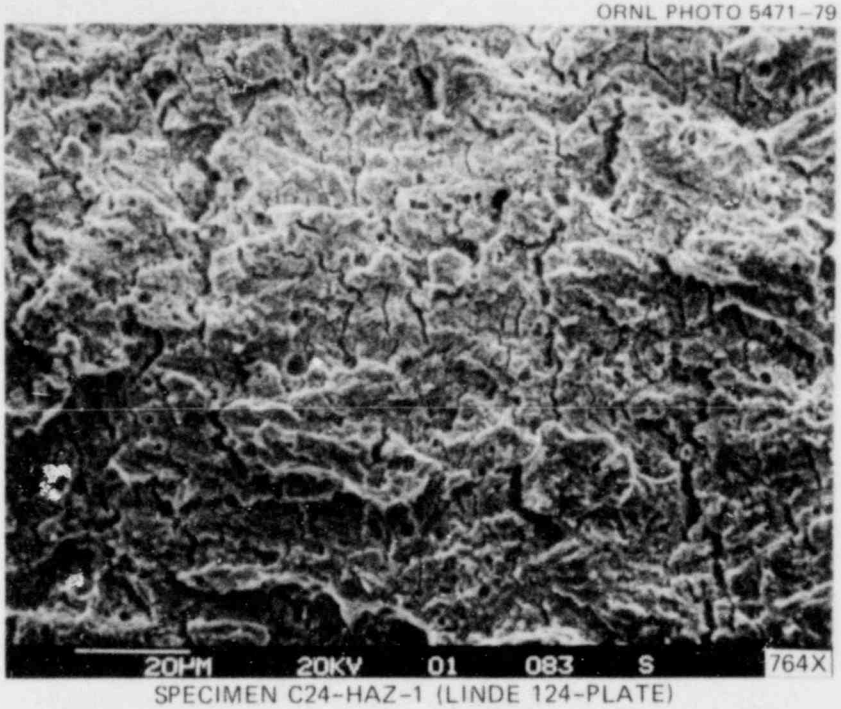

SPECIMEN C24-HAZ-1 (LINDE 124-PLATE)

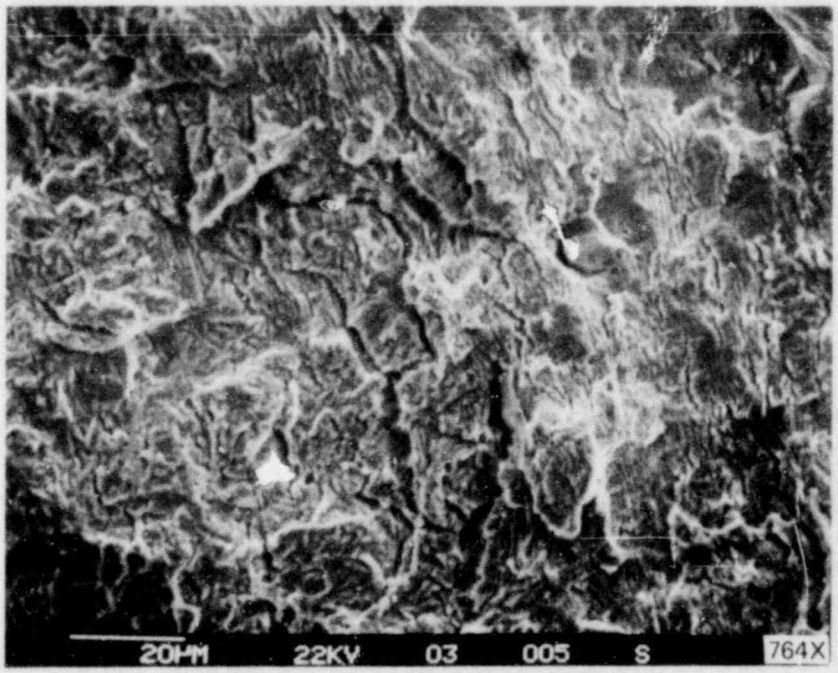

SPECIMEN C1 HAZ (LINDE 80-FORGING)

Fig. 3.7. Comparison of fracture surfaces; Linde 124 vs Linde 80 welds; R = 0.2.

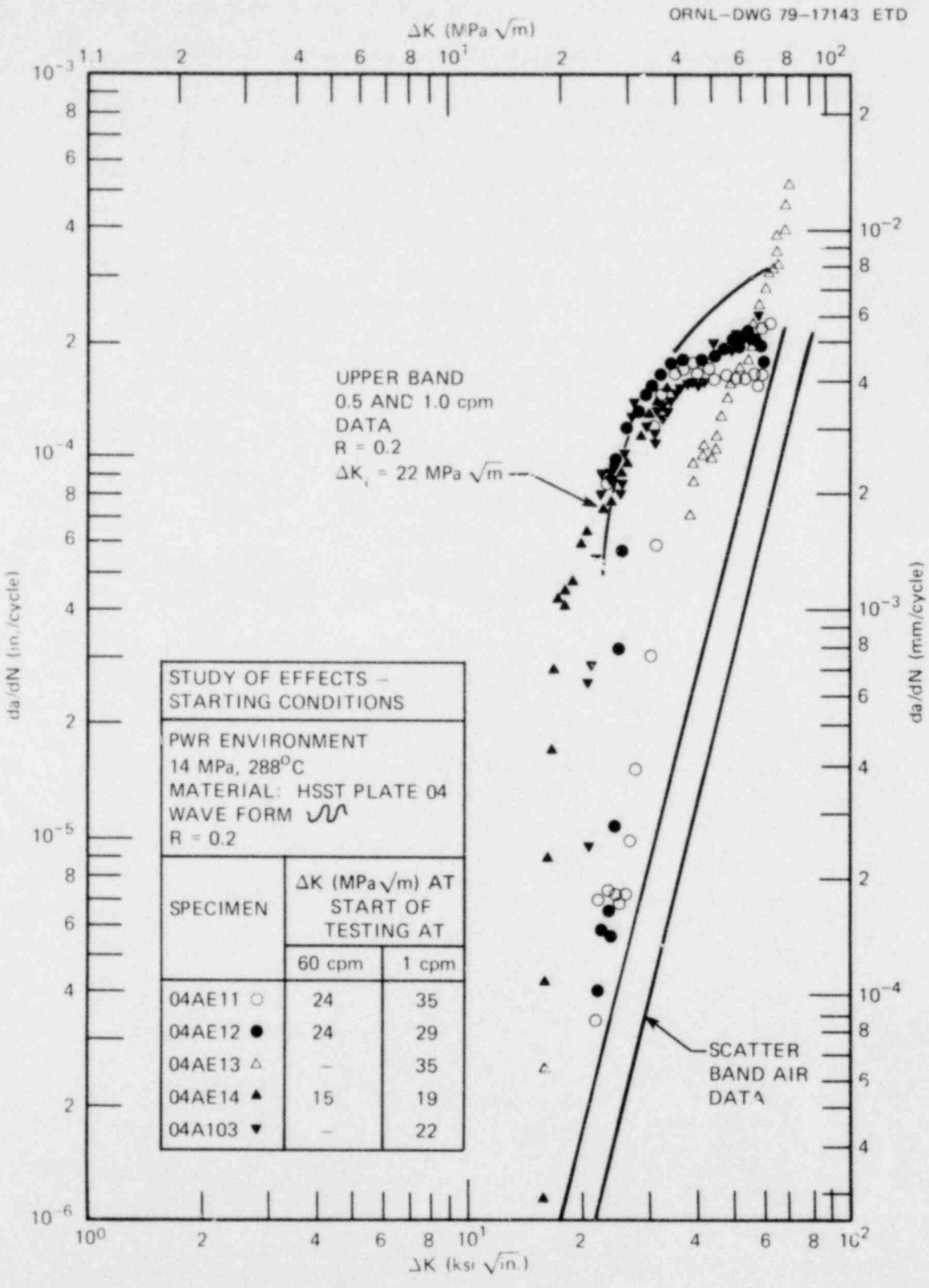

Fig. 3.8. Study of effects—starting conditions; R = 0.2.

The test times required for each of the three tests were factors of 4 to 6 less than those for the conventional tests. Such considerable time savings are possible if we recognize that the early part of the test when the cracks propagate slowly often makes up 80% of the time required for the test. Covering this portion of crack propagation as quickly as possible has always been a major goal, but starting at high values of ΔK to accomplish this has not been successful, as mentioned previously.

Each of the three specimens initially tested at high cyclic frequency accelerated almost immediately to the water-enhanced crack growth behavior obtained in the conventional test of 04A103 as soon as the frequency was changed to 1 cycle/min. This is shown even more clearly, for example, in the crack length test record in Fig. 3.9. Specimens 04AE11 and 04AE12 showed behavior parallel to the air curve until the frequency change, after which the growth rates of the two specimens accelerated almost vertically to the upper band of behavior obtained on previous specimens, as represented by the solid curve. Note that the "conditioning" of the crack in the test of specimen 04AE11 before cycling at 1 cycle/min results in

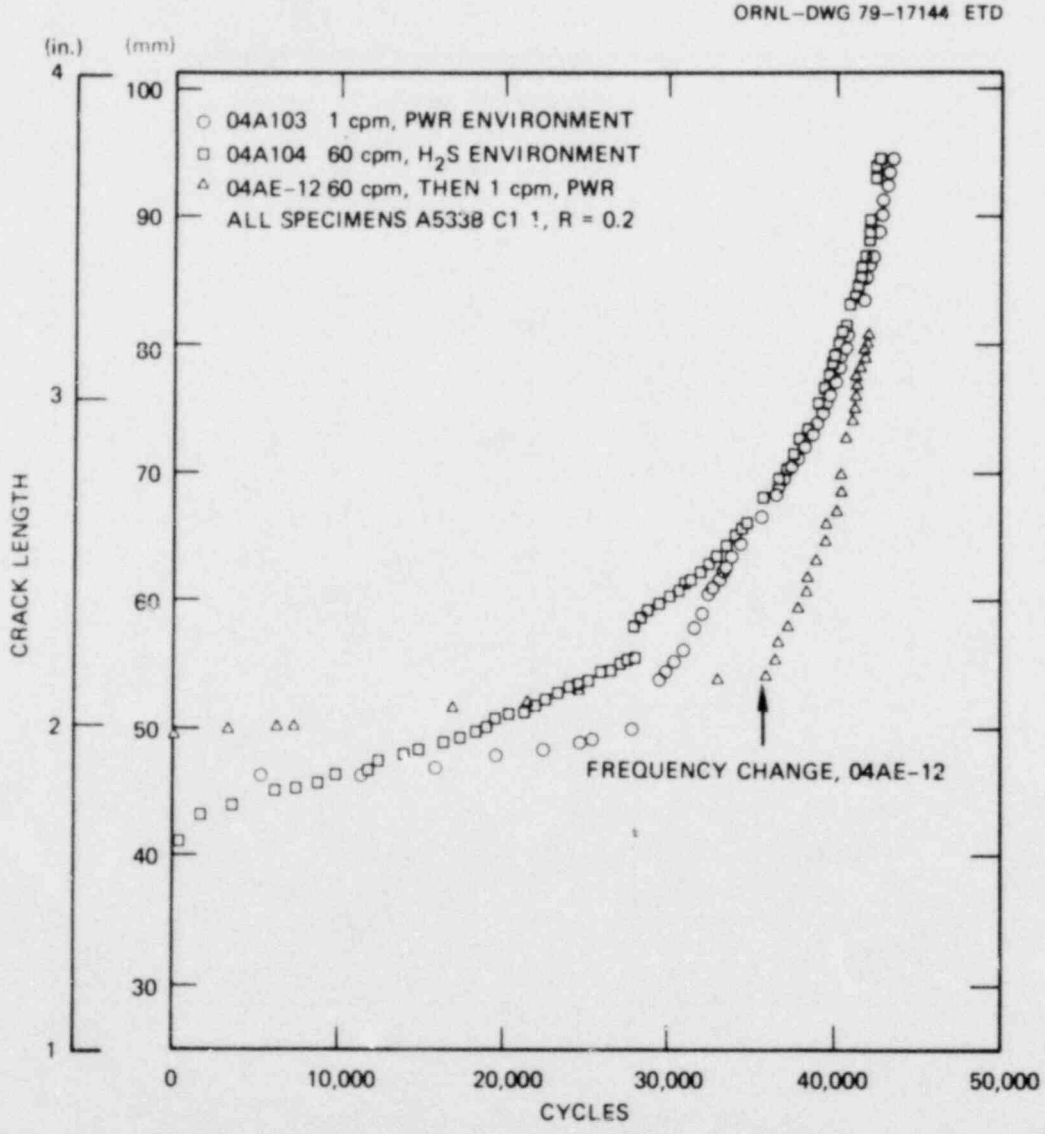

Fig. 3.9. Crack length vs cycles for several selected specimens.

considerably different behavior than does simply starting the 1-cycle/min test at the same ΔK, 35.2 MPa·$\sqrt{m}$, as was done on specimen 04AE13.

Another specimen, 04AE14, was cycled at 60 cycles/min, beginning at a value of ΔK = 15.4 MPa·$\sqrt{m}$. Previous conventional tests at this R ratio had always been started at a higher ΔK because the crack could not otherwise be made to grow. The crack did grow in this test, and, when the frequency was changed to 1 cycle/min at ΔK = 18.7 MPa·$\sqrt{m}$, the growth immediately accelerated to the environmentally influenced behavior and followed the behavior of the other specimens.

The crack growth rate in each of these three specimens reached a value that is virtually identical to the specimen of the same heat tested in the conventional manner, near the solid curve in Fig. 3.8. This strongly suggests that there is an incubation time before a steady-state enhanced growth rate behavior occurs. Note that, once the steady-state behavior occurs, the growth rates of the four specimens form a very narrow band. This indicates that at least some of the "data scatter" reported in corrosion fatigue crack growth rate tests in the past resulted from such non-steady-state behavior, and very little can be attributed to crack length measurement accuracy if these data are any indication. Also note that another source of "scatter" in the results of these environmental tests is the arrests that often occur and that are encouraged by long tests. Only one of these four tests was a long-time test, and, fortunately, no arrests occurred. This is another advantage of a test philosophy that incorporates a fast cycling period to condition the crack; fewer arrests are likely.

Consideration of the crack length test records sheds some further light on the evironmental effects, as shown in Fig. 3.9. As with most of the specimens tested in the conventional way at low cyclic frequency, specimen 04A103 shows a considerable incubation time before crack growth begins to accelerate. This is not seen on crack growth rate plots because relatively sizable increments of growth are always taken to produce these, and very little growth occurs during this incubation time. Note that this incubation period does not occur in a hydrogen sulfide environment, as shown by the results of specimen 04A104, even though the crack growth rates obtained are similar in water and in hydrogen sulfide through the middle of the ΔK range, as shown in Fig. 3.10 and discussed in earlier reports.

In Fig. 3.9, the specimen that was cycled in PWR water at 60 cycles/min and then switched to 1 cycle/min showed an abrupt change in growth rate behavior, indicating that the crack tip had been "conditioned" and was ready to take off when the frequency was slowed.

Comparison of specimen 04AE12 with the one tested conventionally in the PWR environment (04A103) shows that both specimens had an incubation period before the accelerated growth began. Although no attempt was made to reproduce any specific incubation time on specimen 04AE12, this result reveals that there is a finite time for cracks to stabilize with the environment. In tests done at 60 cycles/min, 10 h is clearly enough because that is the length of time before the frequency change on specimen 04AE12. Consideration of specimen 04A103 indicates that 200 or more hours were necessary for acceleration to begin. This apparent anomaly indicates that more than time is important in such a consideration of enhancement. This incubation apparently may be associated with the time required to grow through a characteristic zone of material. Let us assume that this zone is the plastic zone of the specimen and carry further with our investigation.

The plastic zone can be approximated by the expression given below, attributed to Irwin:

$$r_p = \frac{1}{6\pi}\left(\frac{\Delta K}{\sigma_y}\right)^2 ,$$

where σ_y is equal to the yield strength.

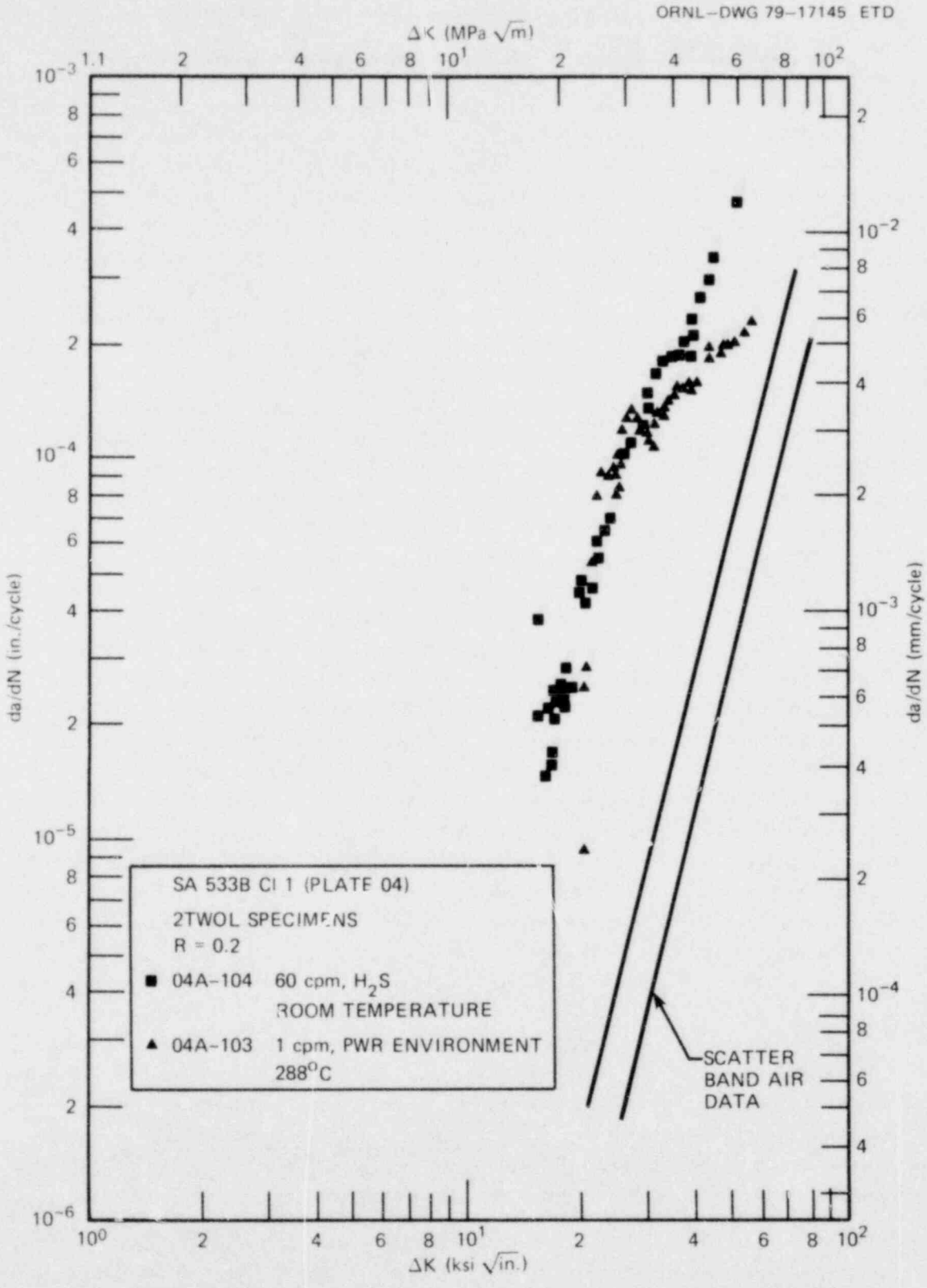

Fig. 3.10. Comparison of crack growth rate results; PWR environment vs hydrogen sulfide at 410 kPa.

Considering a starting ΔK equal to 35 MPa·$\sqrt{m}$, a plastic zone size of 0.25 mm is calculated. If the crack is growing at 1.8×10^{-3} mm/cycle, which is what occurred on specimen 04AE13, 2.3 h are necessary for the crack to grow through the plastic zone. Perhaps the crack is growing through the plastic zone before sufficient hydrogen has concentrated there to enhance the growth. At an initial ΔK = 22 MPa·$\sqrt{m}$, the plastic zone is smaller by a factor of about 2.5, but the growth rate is so much slower (2.5×10^{-5} mm/cycle) that it takes one or two orders of magnitude longer to grow the crack through this zone. This is presumably more than adequate time for hydrogen to accumulate to affect the crack growth.

This type of argument also can explain why there is little or no environmental acceleration in tests done at 60 cycles/min, regardless of the ΔK level. At this frequency, only 0.5 h would be required to propagate the crack through the plastic zone at ΔK = 35 MPa·$\sqrt{m}$ and about 0.7 h to accomplish this at ΔK = 22 MPa·$\sqrt{m}$. Neither of these times may be sufficient to concentrate the adequate amount of hydrogen.

Such an argument also explains why the growth rate obtained in a water environment tends to increase more slowly as ΔK increases (shown clearly in Fig. 3.8), producing the curved effect on a logarithmic plot. As the growth rate increases, it becomes more difficult for hydrogen to keep up with the crack; eventually, the growth rate reaches an equilibrium with the available hydrogen.

The fracture surfaces of two of the specimens in this series were examined microscopically, and results of this work are presented in Fig. 3.11. Both specimens show the same striated appearance, but specimen 04AE13 shows more microcracking, which is evidence of the higher loads being applied. In both cases, the striations do match the macroscopically observed growth.

Clearly, this is only a beginning in the investigation of starting effects and mechanisms. Future work will involve the study of higher values of R ratio and further treatment of results already obtained.

The data interpretation method used on all these specimens distorts this behavior because it uses seven points in an incremental fitting procedure and thus allows earlier slow-growth points to influence the overall fit for a few points. This shows up as a few "transition" points as the growth rate jumps from air to environmentally enhanced behavior. Future work will include a study of this point and comparison with the popular "secant" or point-to-point data interpretation method.

3.3 Fatigue Crack Growth at High ΔK

The results of the recently completed large specimen test to study crack growth rate at very large ΔK values are presented in Fig. 3.12. The test, done on a WOL-type specimen 102 mm thick, was conducted with a 30-s ramp time and quick reset to obtain cycles as expeditiously as possible. The test still required almost 18 months to complete, and the results were disappointing. An R ratio equal to 0.7 was used.

Near the beginning of the test, after the crack had grown ~2.5 mm, the equipment had to be shut down to complete some system repairs. After the shutdown of approximately one month, during which time the specimen sat in a water bath at room temperature, the test was begun again, and the crack growth rate began to slow.

After propagating for ~39.2 mm at progressively slower growth rates (which took nearly 650,000 cycles), the crack began to accelerate, and the growth rate rose quickly to about 2.5×10^{-3} mm/cycle. At this point, the test stand was shut down for slightly more than a day, but the chamber was never opened. After this event, the growth slowed down again, dropping back toward the air growth curve. This short shutdown was the only one experienced during the accelerating growth period, although others had

ORNL PHOTO 5472-79

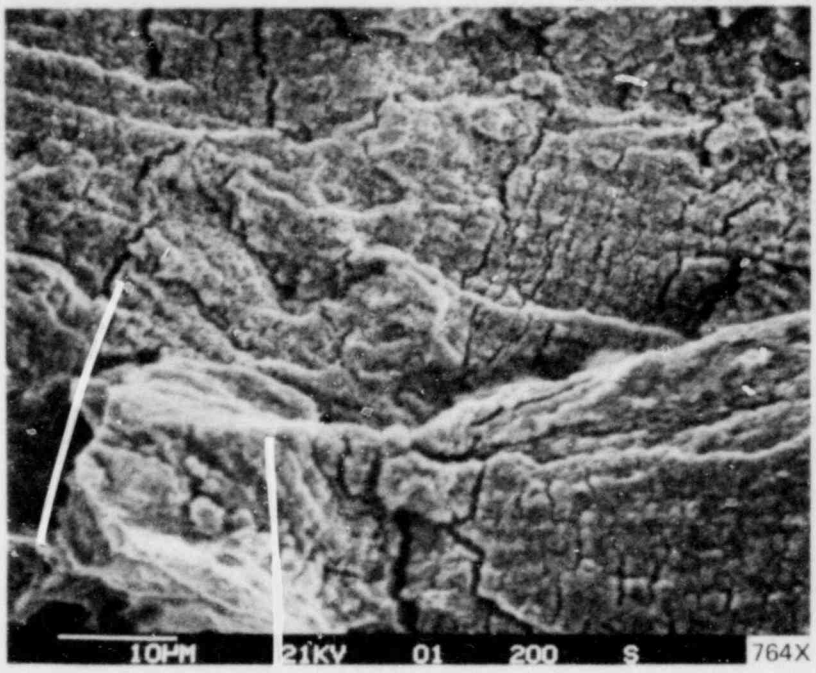

SPECIMEN 04AE13, INITIAL ΔK = 35.2 MPa $\sqrt{m}$

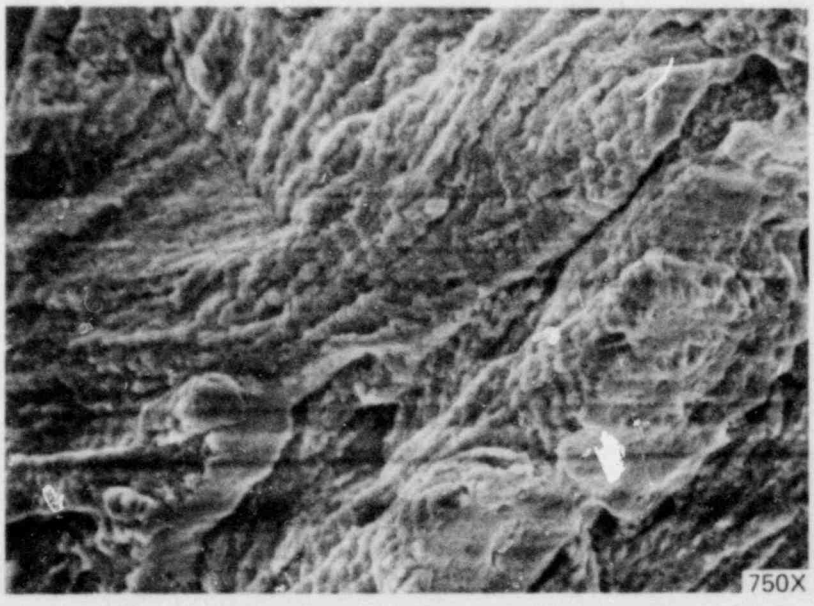

SPECIMEN 04AE14, INITIAL ΔK = 15.4 MPa $\sqrt{m}$

Fig. 3.11. Comparison of fracture surfaces; specimens tested at R = 0.2.

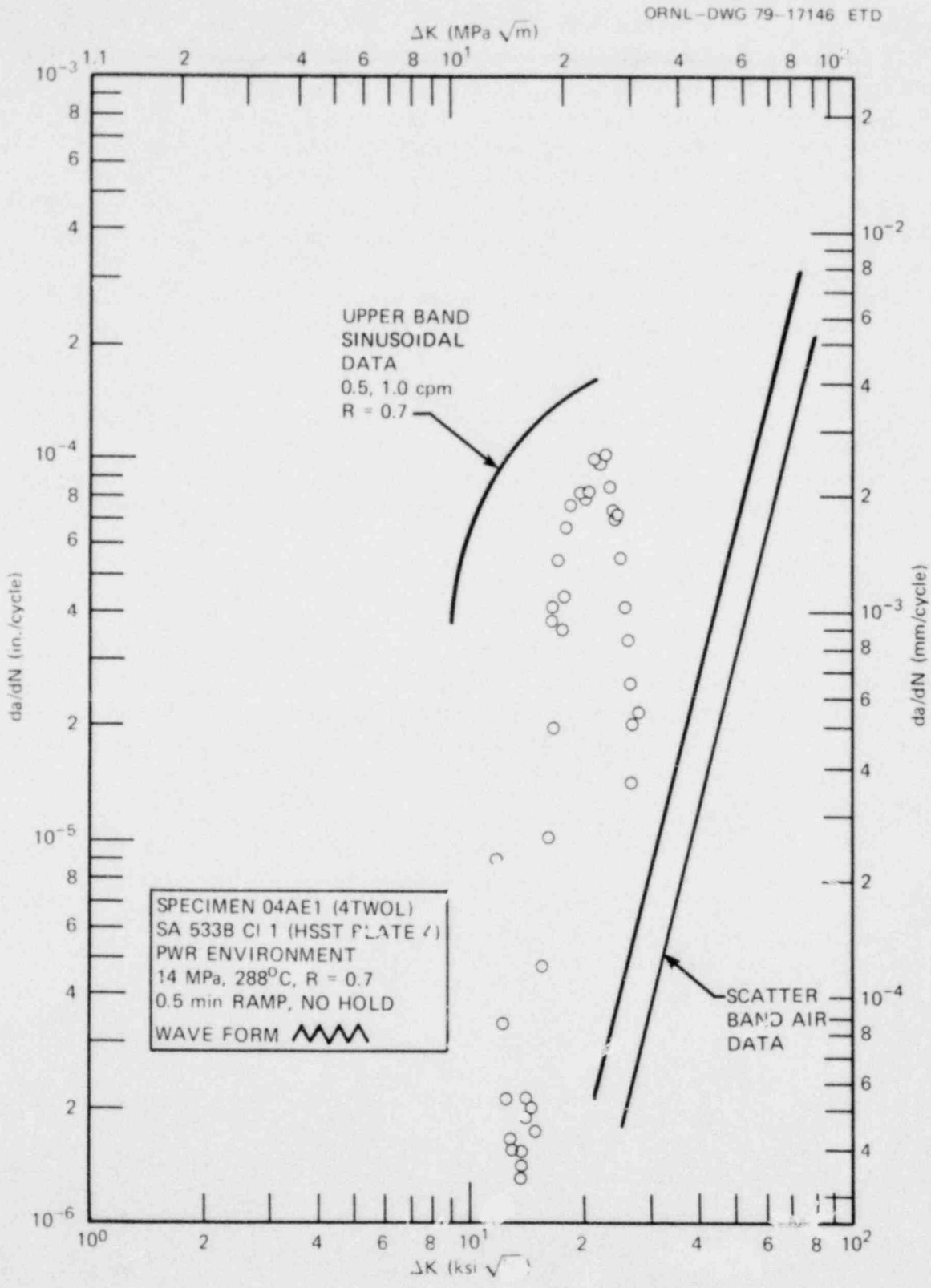

Fig. 3.12. Results of testing specimen 04AE1.

been experienced during the decelerating growth period. This indicates that the growth rate as interpreted by the incremental polynomial method is very sensitive to any changes that occur during the test. The deceleration in growth experienced at the beginning of the test lasted for much longer than the plastic zone size, so there is clearly an unknown variable influencing the time involved in such an event.

As an attempt to obtain crack growth rates at high values of applied K or ΔK, the test was somewhat of a failure because of the reversals experienced. Long tests such as this are extremely difficult, if not impossible, to complete without interruptions, which can negate the value of the test. The specimen did finally get to a value of applied K_{max} equal to about 104.5 MPa·$\sqrt{m}$, with an applied ΔK of 30.2 MPa·$\sqrt{m}$.

Results of this test showed that testing large specimens in the conventional manner is unlikely to provide useful data in the high ΔK regime unless test interruptions can be minimized. This is equivalent to saying that test time should be minimized, and some progress in this direction apparently has been made in the mechanistic studies of "conditioning," as discussed previously. More than 80% of the cycles in the test just completed were expended in the low-growth region, and a fast fequency applied to get through this region as quickly as possible appears the best course of action at present.

Investigations are continuing on the results of this recent test and include both fractography and comparisons of internal and external linear variable differential transformer (LVDT) crack measurement methods.

References

1. G. D. Whitman and R. H. Bryan, *Heavy-Section Steel Technology Program Quart. Prog. Rep. April–June, 1979*, ORNL/NUREG/TM-347 (October 1979).

2. W. H. Bamford and D. M. Moon, "Some Mechanistic Observations on the Crack Growth Characteristics of Pressure Vessel and Piping Steels in PWR Environment," presented at National Association of Corrosion Engineers meeting Corrosion 79 (to be published in *Corrosion*).

4. INVESTIGATIONS OF IRRADIATED MATERIALS*

4.1 Toughness Investigations of Irradiated Materials

R. G. Berggren J. W. Woods
T. N. Jones D. A. Canonico

4.1.1 Second 4T CS irradiation study

Previously we reported[1] Charpy V-notch impact (C_V) test results for three low-shelf submerged-arc weldments (weld numbers 61W, 62W, and 63W). One objective of this irradiation study was to irradiate these welds to upper-shelf energies of about 68 J (50 ft-lb); this objective was achieved. The initial tests, which were conducted to ensure that the 68-J objective was satisfied, utilized a minimum number of specimens. To better determine the irradiated upper-shelf (ductile) energies for these three weldments, 22 additional impact tests were conducted at temperatures above the onset of upper shelf. Results from these tests and pertinent prior C_V results for 61W, 62W, and 63W are presented in Figs. 4.1, 4.2, and 4.3, respectively. Loss of upper-shelf energy due to irradiation was markedly less (40 to 60%) than that predicted by Regulatory Guide 1.99 (Ref. 2). This may be an indication that the loss of upper-shelf energy is less for "low-shelf" materials than for materials with higher initial upper-shelf energies.

*Conversions from SI to English units for all SI quantities are listed on a foldout page at the end of this report.

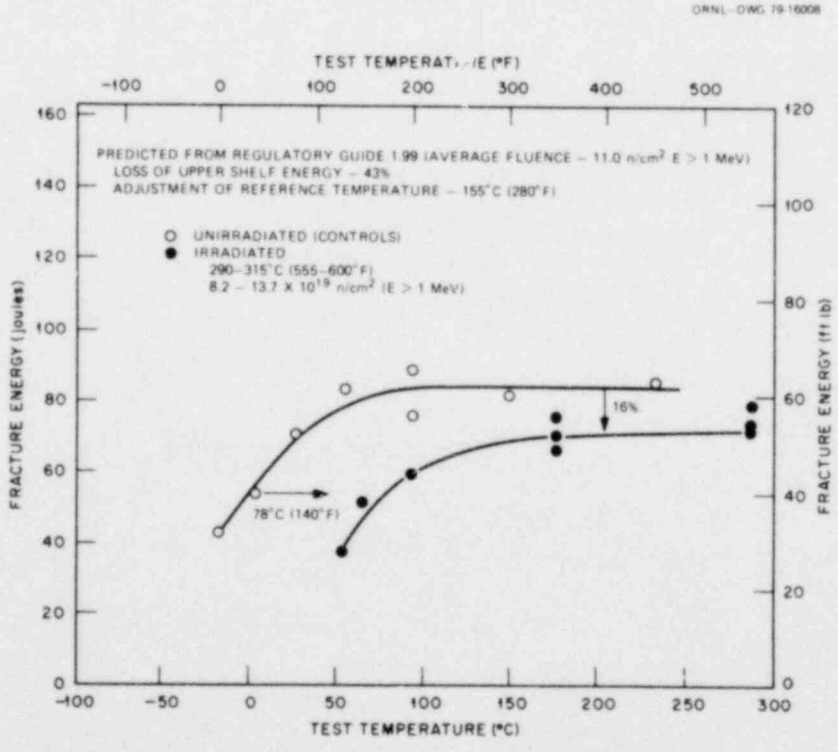

Fig. 4.1. Charpy V-notch impact data from weld 61W. Average copper content = 0.28%.

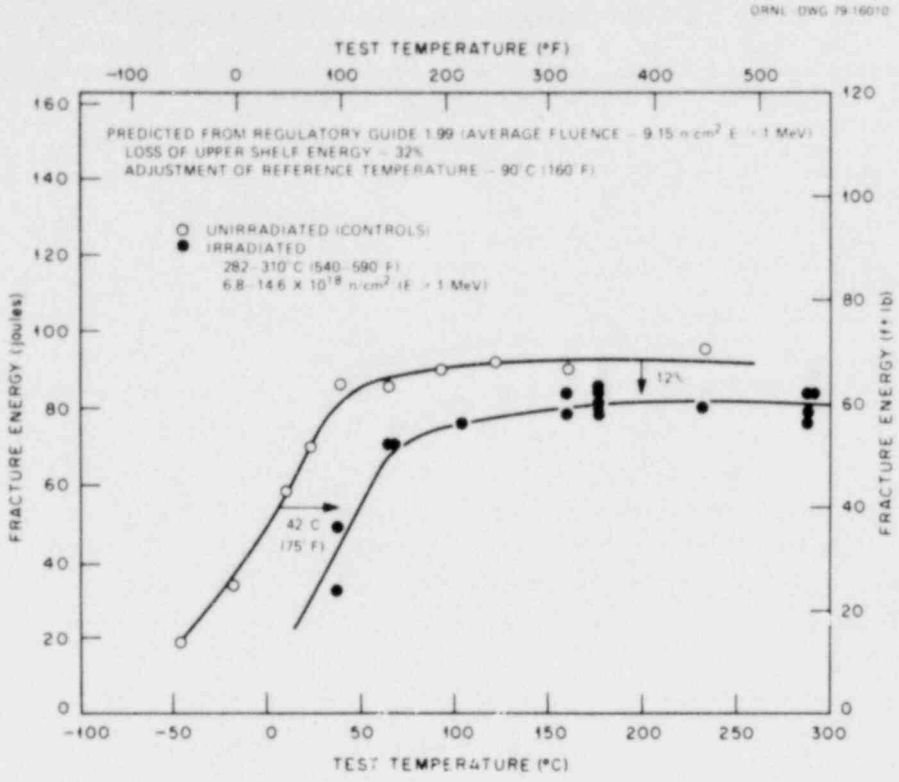

Fig. 4.2. Charpy V-notch impact data from weld 62W. Average copper content = 0.19%.

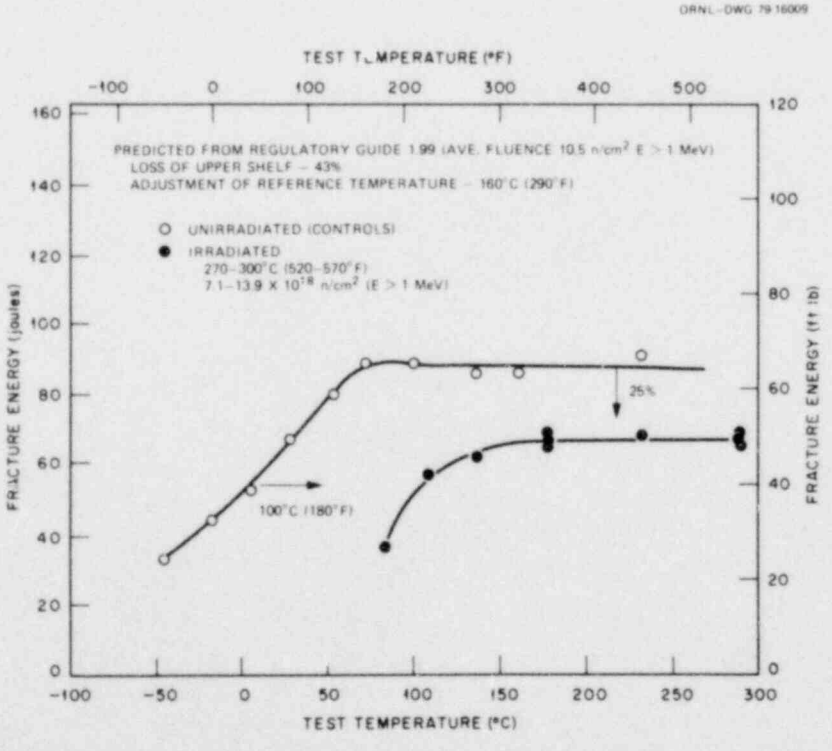

Fig. 4.3. Charpy V-notch impact data from weld 63W. Average copper content = 0.30%.

4.1.2 Third 4T CS irradiation study

Fast neutron dosimeter results and irradiation temperature records for this irradiation experiment were reviewed, and fast neutron fluences and irradiation temperatures for each specimen in the three capsules of this irradiation experiment were determined by three-dimensional interpolations. Tables 4.1 through 4.4 present irradiation parameters for each specimen.

The total irradiation time for the irradiation [which was done at 2 MW in the Bulk Shielded Reactor (BSR)] for capsules A and B (HSST weldments 64W and 65W) was 1012 h and for capsule C (HSST weldments 66W and 67W) was 1581 h. Each capsule was first irradiated in the "forward" position for 40% of the irradiation time, then rotated 180° and irradiated in the "reverse" position for an additional 50% of the irradiation time, then rotated back to the original "forward" position and irradiated for the final 10% of the total irradiation time.

We chose to report "median" irradiation temperatures as being the most meaningful data. We also determined "average" and maximum temperatures and percent of time in 3° C (5° F) intervals for each recording thermocouple, but these are not reported in the tables. Temperatures below 232° C (450° F), recorded during experiment start-up, have an inordinate effect on the "average" temperatures (only 10% of recorded temperatures were less than the average temperatures). Maximum temperatures, in almost all cases, were recorded during the initial start-up period and thus would have little effect on radiation-induced property changes. In almost all cases, more than 90% of the temperature recordings were within ±5.6° C (10° F) of the median temperatures.

4.1.3 Fourth HSST irradiation series

The first capsule of this irradiation series[3] has been assembled, and final preirradiation testing is in progress prior to start of irradiation. The capsule contains 60 1T compact specimens, 70 Charpy V-notch specimens, 20 precracked Charpy specimens, 10 tensile test specimens, and neutron dosimeters. All specimens are from HSST plate 02 (ASTM A533 grade B class 1 steel plate).

Because 1T compact specimens are used in this irradiation series rather than the 0.5T through 4T compact specimens used in the previous irradiation studies, the capsule was redesigned, and the capsules will not be rotated during irradiation. To achieve more uniform irradiation temperatures, 12 electrical heating sections are used (Fig. 4.4). The specimens are installed in an internal frame in the capsule and spring-loaded against the heater plate. Figure 4.5 shows the capsule during installation of specimens, thermocouples, and neutron dosimeters. In front of the capsule are typical specimens, spring assemblies, and a dosimeter capsule. The arrangement of specimens may be seen in the center portion of the capsule, with installed spring assemblies at the top of the capsule. Heat flow in the capsule is from the specimens through the heater plate, across a gas gap, through the capsule face, and into a cooling water jacket next to the reactor face.

Specimens of submerged-arc weldments are being machined for the second capsule of this series.

Table 4.1. Third 4T CT irradiation experiment (HSST-BSR-2). Fast neutron fluences and median irradiation temperatures for 4T compact specimens

Specimen No.	Capsule coordinates forward position (mm)			Forward position			Reverse position			Total fluence (10^{22} neutrons/m^2)[a]	Median temperature	
				Fluence	Temperature		Fluence	Temperature				
	X	Y	Z	(10^{22} neutrons/m^2)[a]	(°C)	(°F)	(10^{22} neutrons/m^2)[a]	(°C)	(°F)		(°C)	(°F)
Weldment 64W—Capsule A												
64W-22	0	−122	0	7.29	289	553	1.21	262	503	8.50	276	528
	0	−122	6	6.76	289[b]	553[b]	1.37	264[b]	508[b]	8.13	277	530
	0	−122	13	6.23	289	553	1.56	268	514	7.79	279	534
	0	−122	25	5.15	289[b]	553[b]	2.02	272[b]	522[b]	7.17	281	538
	0	−122	38	4.16	288	551	2.59	278	532	6.75	283	542
	0	−122	51	3.30	286	547	3.30	283	542	6.60	285	545
	0	−122	64	2.59	280	536	4.16	287	549	6.75	283	542
	0	−122	76	2.02	272[b]	521[b]	5.15	289[b]	553[b]	7.17	281	537
	0	−122	89	1.56	264	507	6.23	287	549	7.79	176	528
	0	−122	95	1.37	259[b]	498[b]	2.76	284[b]	544[b]	8.13	272	521
	0	−122	102	1.21	254	490	7.29	283	541	8.50	269	5[illegible]
64W-23	0	−122	0	7.09	284	543	1.18	280	536	8.27	282	540
	0	−122	6	6.70	286[b]	546[b]	1.34	281[b]	538[b]	8.04	283	542
	0	−122	13	6.06	289	552	1.52	283	542	7.58	286	547
	0	−122	25	5.00	292[b]	557[b]	1.98	286[b]	547[b]	6.98	289	552
	0	−122	38	4.04	292	557	2.52	288	551	6.56	290	554
	0	−122	51	3.21	292[b]	557[b]	3.21	290[b]	554[b]	6.42	291	556
	0	−122	64	2.52	291	555	4.04	291	555	6.56	291	555
	0	−122	76	1.98	289[b]	553[b]	5.00	291[b]	556[b]	6.98	290	554
	0	−122	89	1.52	288	551	6.06	289	552	7.58	289	552
	0	−122	95	1.34	288[b]	550[b]	6.70	287[b]	549[b]	8.04	288	550
	0	−122	102	1.18	287	549	7.09	286	547	8.27	287	548
Weldment 65W—Capsule B												
65W-24	0	−122	0	8.26	287	548	1.42	253	488	9.68	270	518
	0	−122	6	7.62	288[b]	551[b]	1.62	257[b]	494[b]	9.24	272	522
	0	−122	13	6.88	290	554	1.82	262	504	8.70	276	529
	0	−122	25	5.69	291[b]	556[b]	2.30	271[b]	519[b]	7.99	281	538
	0	−122	38	5.64	289	552	2.94	277	531	7.58	283	542
	0	−122	51	3.72	284[b]	543[b]	3.72	283[b]	541[b]	7.44	283	542
	0	−122	64	2.94	278	533	4.65	288	550	7.58	283	542
	0	−122	76	2.30	273[b]	523[b]	5.69	291[b]	556[b]	7.99	282	540
	0	−122	89	1.82	265	509	6.88	292	557	8.70	278	533
	0	−122	95	1.62	261[b]	502[b]	7.62	291[b]	556[b]	9.24	276	529
	0	−122	102	1.42	258	496	8.26	291	555	9.68	274	526

Table 4.1 (continued)

Specimen No.	Capsule coordinates forward position (mm)			Forward position			Reverse position			Total fluence (10^{22} neutrons/m^2)[a]	Median temperature	
	X	Y	Z	Fluence (10^{22} neutrons/m^2)[a]	Temperature (°C)	(°F)	Fluence (10^{22} neutrons/m^2)[a]	Temperature (°C)	(°F)		(°C)	(°F)
65W-25	0	−122	0	6.72	288	550	1.17	287	548	7.88	287	549
	0	−122	6	6.26	288[b]	551[b]	1.32	288[b]	550[b]	7.58	288	550
	0	−122	13	5.63	289	552	1.50	289	552	7.13	289	552
	0	−122	25	4.67	289[b]	553[b]	1.88	291[b]	555[b]	6.55	290	554
	0	−122	38	3.82	288	551	2.41	292	558	6.23	290	554
	0	−122	51	3.05	287[b]	548[b]	3.05	294[b]	561[b]	6.11	290	554
	0	−122	64	2.41	283	542	3.82	295	563	6.23	289	552
	0	−122	76	1.88	279[b]	535[b]	4.67	296[b]	565[b]	6.55	288	550
	0	−122	89	1.50	276	528	5.63	294	561	7.13	284	544
	0	−122	95	1.32	273[b]	524[b]	6.26	292[b]	558[b]	7.58	283	541
	0	−122	102	1.17	271	520	6.72	291	555	7.88	281	538
Weldment 67W—Capsule C												
67W-23	0	−122	0	9.45	288	551	1.63	288	509	11.08	277	530
	0	−122	6	8.70	289[b]	553[b]	1.86	267[b]	513[b]	10.56	278	533
	0	−122	13	7.99	291	555	2.11	271	520	10.10	281	538
	0	−122	25	6.57	291[b]	556[b]	2.67	277[b]	530[b]	9.24	284	543
	0	−122	38	5.33	288	550	3.40	281	538	8.73	284	544
	0	−122	51	4.30	283[b]	542[b]	4.30	285[b]	545[b]	8.60	284	544
	0	−122	64	3.40	278	533	5.33	288	551	8.73	283	542
	0	−122	76	2.67	272[b]	521[b]	6.57	289[b]	552[b]	9.24	280	536
	0	−122	89	2.11	263	506	7.99	287	548	10.10	275	527
	0	−122	95	1.86	257[b]	494[b]	8.70	283[b]	541[b]	10.56	270	518
	0	−122	102	1.63	253	487	9.45	281	538	11.08	270	518
67W-24	0	−122	0	10.58	282	540	1.83	276	529	12.41	279	534
	0	−122	6	9.71	284[b]	544[b]	2.14	278[b]	532[b]	11.85	281	538
	0	−122	13	8.94	288	550	2.36	280	536	11.30	284	543
	0	−122	25	7.36	292[b]	557[b]	3.01	283[b]	542[b]	10.37	287	548
	0	−122	38	5.96	292	558	3.80	285	545	9.76	289	552
	0	−122	51	4.81	292[b]	557[b]	4.81	287[b]	548[b]	9.62	289	552
	0	−122	64	3.80	291	555	5.96	288	551	9.76	289	553
	0	−122	76	3.01	289[b]	552[b]	7.36	289[b]	552[b]	10.37	289	552
	0	−122	89	2.36	286	547	8.94	288	550	11.30	287	548
	0	−122	95	2.14	284[b]	543[b]	9.71	286[b]	546[b]	11.85	284	544
	0	−122	102	1.83	282	540	10.58	284	543	12.41	283	542

[a] 10^{22} neutrons/m^2 = 10^{18} neutrons/cm^2. E > 1 MeV.

[b] Thermocouples were located at these coordinate sites; other temperature readings were interpolated.

Table 4.2. Third 4T CT irradiation experiment (HSST-BSR-2) Capsule A. Fast neutron fluences and median irradiation temperatures for specimens from weldment 64W

Specimen type[a]	Specimen No.	Forward position			Reverse position			Total fluence (10^{22} neutrons/m^2)[b]	Median temperature	
		Fluence (10^{22} neutrons/m^2)[b]	Temperature (°C)	(°F)	Fluence (10^{22} neutrons/m^2)[b]	Temperature (°C)	(°F)		(°C)	(°F)
1.6T CS	64W-30	3.33	279[c]	534[c]	2.90	292[c]	557[c]	6.23	286	546
	31	4.44	298[c]	569[c]	2.27	278[c]	533[c]	6.71	288	551
0.8T CS	64W-40	5.25	298[c]	568[c]	2.48	271[c]	519[c]	7.73	284	544
	43	5.25	298[c]	568[c]	2.48	271[c]	591[c]	7.73	284	544
	45	2.48	274[c]	526[c]	5.25	291[c]	556	7.73	283	541
	44	2.48	274[c]	526[c]	5.25	291[c]	556[c]	7.73	283	541
0.5T CS	64W-101	5.38	294[c]	562[c]	1.34	268[c]	514[c]	6.72	281	538
	107	3.12	298	569	2.58	279	535	5.70	286	547
	104	1.35	294	561	5.38	293	560	6.72	293	560
	108	4.65	277	531	1.17	266	510	5.82	271	520
	110	2.71	281[c]	538[c]	2.24	278[c]	533[c]	4.95	279	335
	111	1.17	277	530	4.65	296	565	5.82	287	548
	114	3.05	238[c]	461[c]	0.70	234[c]	453[c]	3.75	236	457
	112	1.77	242[c]	468[c]	1.36	246[c]	475[c]	3.13	244	472
	113	0.75	238[c]	460[c]	2.86	258[c]	497[c]	3.61	248	479
	115	2.86	238	461	0.75	234	453	3.61	244	472
	116	1.65	242	468	1.45	246	475	3.00	244	472
	117	0.70	238	460	3.05	258	497	3.75	248	479
	118	2.54	272[c]	521[c]	0.59	269[c]	517[c]	3.09	271	519
	119	1.46	278[c]	532[c]	1.13	273[c]	524[c]	2.56	276	528
	121	0.62	276[c]	528[c]	2.37	270[c]	518[c]	2.98	273	523
	122	2.37	272	521	0.62	269	517	2.98	271	519
	123	1.38	278	532	1.21	273	524	2.54	276	528
	124	0.59	276	528	2.54	270	518	3.09	273	523
	125	4.15	291	556	0.79	259	498	4.94	275	527
	127	4.48	292[c]	558[c]	0.85	259[c]	499[c]	5.33	276	528
	129	4.82	291	556	0.93	259	498	5.75	275	527
	130	2.02	275	527	1.68	270	518	3.70	272	522
	131	2.17	276[c]	529[c]	1.81	271[c]	519[c]	3.98	273	524
	132	2.35	275	527	1.95	270	518	4.30	272	522
	133	0.91	258	297	3.22	268	515	4.13	263	506
	134	0.99	259[c]	498[c]	3.48	269[c]	516[c]	4.47	264	507
	135	1.06	258	497	3.75	268	515	4.81	263	506
	138	3.75	279	535	1.06	288	550	4.81	283	542
	136	3.48	279	535	0.99	288	550	4.47	283	542
	139	3.22	279	535	0.91	288	550	4.13	283	542
	140	0.84	245[c]	473[c]	5.16	281[c]	538[c]	6.00	263	506
	141	4.52	292[c]	558[c]	0.88	277[c]	531[c]	5.40	284	544
	142	4.15	292	558	0.81	277	531	4.96	284	544
	143	3.66	292	558	0.72	277	531	4.38	284	544
	144	0.89	290[c]	554[c]	3.78	275[c]	527[c]	4.61	282	540
	145	3.51	272	521	1.00	282	540	4.51	277	530
	146	3.22	272[c]	521[c]	0.91	282[c]	540[c]	4.13	277	530
	147	2.85	272	521	0.81	282	540	3.66	277	530
	148	0.79	[illegible]	531[c]	4.84	285[c]	545[c]	5.63	281	538
C_v	64W-200	3.76	238	460	0.75	231	448	4.61	234	454
	201	3.35	239	463	0.92	236	456	4.27	238	460
	202	2.87	241	466	1.13	240	464	4.00	241	465
	203	2.43	242	468	1.38	243	470	3.81	243	469
	204	2.02	243	470	1.67	247	477	3.69	246	474
	205	1.67	242	468	2.02	251	484	3.69	247	476
	206	1.38	241	466	2.43	254	489	3.81	248	478
	207	1.13	240	464	2.87	257	494	4.00	248	479
	208	0.92	239	462	3.35	259	499	4.27	249	480
	209	0.75	237	458	3.76	262	504	4.61	249	481
	276	5.29	286	546	1.03	286	547	6.32	286	546
	277	3.95	289	552	1.56	288	550	5.51	288	551
	278	2.79	291[c]	556[c]	2.31	289[c]	553[c]	5.10	290	554
	279	2.31	291[c]	556[c]	2.79	289[c]	553[c]	5.10	290	554
	280	1.56	290	554	3.95	287	548	5.51	288	551
	281	1.03	289[c]	552[c]	5.29	284[c]	543[c]	6.32	287	548
	282	3.58	272	522	0.70	270	518	4.28	271	520
	283	2.67	275	527	1.06	272	522	3.73	273	524

Table 4.2 (continued)

Specimen type[a]	Specimen No.	Forward position			Reverse position			Total fluence (10^{22} neutrons/m^2)[b]	Median temperature	
		Fluence (10^{22} neutrons/m^2)[b]	Temperature (°C)	Temperature (°F)	Fluence (10^{22} neutrons/m^2)[b]	Temperature (°C)	Temperature (°F)		(°C)	(°F)
C_v	64W-284	1.90	279	534	1.56	274	526	3.49	277	530
	285	1.56	279	534	1.90	274	526	3.49	277	530
	286	1.06	276	532	2.67	273	523	3.73	276	528
	287	0.70	277	530	3.58	271	520	4.28	274	525
	288	1.66	262	503	2.57	284	544	4.23	273	524
	289	1.54	262	503	2.39	284	544	3.93	273	524
	293	1.75	262	503	2.80	284	544	4.55	273	524
	292	1.66	264	507	2.65	286	547	4.31	273	524
	291	1.55	264	507	2.48	286	547	4.03	273	524
	290	1.43	262	503	2.28	284	544	3.71	273	524
	294	1.68	262	503	2.77	284	544	4.45	273	524
	295	1.59	264[c]	507[c]	2.62	286[c]	547[c]	4.21	275	527
	296	1.49	264	507	2.45	286	547	3.94	275	527
	297	1.42	262[c]	503[c]	2.35	284[c]	544[c]	3.77	273	524
	298	1.54	262	563	2.65	284	544	4.19	273	524
	299	1.43	262	503	2.46	284	544	3.89	273	524
	300	1.33	262	503	2.30	284	544	3.63	273	524
	301	1.77	293	560	2.05	281	537	3.82	287	548
	302	1.59	293	560	1.84	281	537	3.43	287	548
	303	1.92	293	560	2.16	281	537	4.08	287	548
	304	1.81	294	562	2.04	282	539	3.85	288	550
	305	1.65	294	562	1.86	282	539	3.51	288	550
	306	1.51	293	560	1.68	281	537	3.19	287	548
	307	1.90	293	560	2.07	281	537	3.97	287	548
	308	1.79	294[c]	562[c]	1.95	282[c]	539[c]	3.74	288	550
	309	1.64	294	562	1.78	282	539	3.42	288	550
	310	1.48	293	560	1.61	281	537	3.09	287	548
	311	1.84	293	560	1.91	281	537	3.75	287	548
	312	1.71	293	560	1.78	281	537	3.49	287	548
	313	1.54	293	560	1.60	281	537	3.14	287	548
	314	1.54	275	527	2.36	287	548	3.90	281	538
	315	1.39	275	527	2.13	287	548	3.52	281	538
	316	1.63	275	527	2.58	287	548	4.21	281	538
	317	1.53	277	531	2.43	288	551	3.96	283	541
	318	1.40	277	531	2.22	288	551	3.62	283	541
	319	1.27	275	527	2.01	287	548	3.28	281	538
	320	1.56	275	527	2.56	287	548	4.12	281	538
	321	1.47	277[c]	531[c]	2.41	288[c]	551[c]	3.88	283	541
	322	1.34	277	531	2.20	288	551	3.54	283	541
	323	1.21	275[c]	527[c]	1.99	287[c]	548[c]	3.20	281	538
	324	1.43	275	527	2.47	287	548	3.90	281	538
	325	1.34	275	527	2.30	287	548	3.64	281	538
	326	1.20	275	527	2.07	287	548	3.27	281	538
PCC_v	64W-210C	4.61	287	549	1.27	287	549	5.88	287	549
	211C	3.34	290	554	1.90	289	552	5.24	289	553
	212C	1.90	291	555	3.34	288	551	5.24	289	553
	213C	1.27	289[c]	533[c]	4.61	284[c]	543[c]	5.88	287	548
	214C	3.12	273	523	0.86	271	519	3.98	272	521
	215C	2.26	277	531	1.28	273	524	3.54	276	528
	216C	1.28	278	533	2.26	274	525	3.54	276	529
	217C	0.86	277	531	3.12	272	522	3.98	274	526
Tensile	64W-4	4.80	293	560	1.89	269	516	6.69	281	538
	5	1.89	277	530	4.80	287	548	6.69	282	539
	6	1.76	292	558	0.69	287	548	2.45	289	553
	7	0.69	289	553	1.76	291	555	2.45	290	554
	8	4.60	275	527	1.82	272	522	6.42	273	524
	9	1.82	277	530	4.60	271	520	6.42	274	525
	1	1.77	262	503	2.75	284	544	4.52	273	524
	2	1.89	293	560	2.21	281	537	4.10	287	548
	3	1.65	275	527	2.54	287	548	4.19	281	538

[a]CS—compact specimen; C_v—standard Charpy V-notch impact specimen; PCC_v—precracked Charpy V-notch specimen; tensile—0.178-in. gage diameter.
[b]10^{22} neutrons/m^2 = 10^{18} neutrons/cm^2, E > 1 MeV.
[c]Thermocouples were located at these coordinate sites; other temperature readings were interpolated.

Table 4.3. Third 4T CT irradiation experiment (HSST-BSR-2) capsule B. Fast neutron fluences and median irradiation temperatures for specimens from weldment 65W

Specimen type[a]	Specimen No.	Forward position			Reverse position			Total fluence (10^{22} neutrons/m^2)[a]	Median temperature	
		Fluence (10^{22} neutrons/m^2)[a]	Temperature (°C)	(°F)	Fluence (10^{22} neutrons/m^2)[a]	Temperature (°C)	(°F)		(°C)	(°F)
1.6T CS	65W-37	4.63	304[c]	579[c]	2.07	274[c]	526[c]	6.70	289	552
	39	3.00	274[c]	525[c]	3.20	308[c]	586[c]	6.20	291	556
0.8T CS	65W-41	5.01	291[c]	556[c]	2.43	276[c]	528[c]	7.44	283	542
	42	5.09	291[c]	556[c]	2.47	276[c]	528[c]	7.56	283	542
	44	2.43	270[c]	518[c]	5.01	298[c]	568[c]	7.44	284	543
	45	2.47	270[c]	518[c]	5.09	298[c]	568[c]	7.56	284	543
0.5T CS	65W-100	6.07	297[c]	566[c]	1.60	269[c]	517[c]	7.67	283[c]	542
	101	3.55	289	552	2.97	283	541	6.52	286	546
	103	1.60	278	532	6.07	293	559	7.67	286	546
	104	4.98	294	561	1.31	279	534	6.29	287	548
	105	2.92	286[c]	547[c]	2.44	287[c]	548[c]	5.36	287	548
	106	1.31	275	527	4.98	297	566	6.29	283	542
	107	2.15	286[c]	546[c]	0.62	266[c]	510[c]	3.77	273	523
	108	1.24	278[c]	532[c]	1.16	279[c]	534[c]	2.40	278	533
	109	0.56	267[c]	512[c]	2.39	289[c]	552[c]	2.95	278	532
	111	2.39	286	546	0.5[c]	266	510	2.95	273	523
	112	1.38	278	532	1.04	279	534	2.42	278	533
	113	0.62	267	512	2.15	289	552	3.77	278	532
	115	1.90	262[c]	503[c]	0.56	273[c]	524[c]	2.46	270	518
	118	1.11	258[c]	497[c]	1.03	276[c]	528[c]	2.14	267	512
	120	0.50	264[c]	508[c]	2.10	273[c]	523[c]	2.60	269	516
	122	2.10	262	503	0.50	273	524	2.60	268	514
	123	1.24	258	497	0.93	276	528	2.17	267	512
	124	0.56	264	508	1.90	273	523	2.46	269	516
	126	2.80	282	541	1.01	273	524	3.81	268	514
	127	3.36	283[c]	542[c]	1.21	274[c]	526[c]	4.57	279	534
	129	3.74	283	541	1.35	273	524	5.09	268	514
	130	1.48	269	516	2.10	296	565	3.58	282	540
	131	1.77	269[c]	517[c]	2.51	298[c]	569[c]	4.28	284	543
	133	1.98	269[c]	516[c]	2.81	296[c]	565[c]	4.79	282	540
	136	0.72	252	486	4.00	302	576	4.72	277	531
	137	0.85	253[c]	487[c]	4.76	304[c]	580[c]	5.61	279	534
	138	0.96	252	486	5.33	302	576	6.29	277	531
	139	5.33	319	607	0.96	258	497	6.29	289	552
	140	4.76	320[c]	608[c]	0.85	259[c]	498[c]	5.61	289	553
	142	4.00	319	607	0.72	258	497	4.72	289	552
	143	1.24	267[c]	513[c]	4.10	272[c]	522[c]	5.34	269	516
	144	3.04	276	528	1.06	295	563	4.10	286	546
	145	2.71	276[c]	528[c]	0.95	295[c]	563[c]	3.66	286	546
	146	2.36	276	528	0.82	295	563	3.18	286	546
	157	0.70	265[c]	507[c]	4.44	292[c]	557[c]	5.14	278	532
	159	4.26	293	559	0.77	276	528	5.03	284	544
	160	3.81	293[c]	559[c]	0.69	276[c]	528[c]	4.50	284	544
	161	3.31	293	559	0.60	276	528	3.91	284	544
	162	0.96	276[c]	528[c]	3.22	269[c]	516[c]	4.18	272	522
C_v	65W-233	3.28	287	548	0.67	261	502	3.95	274	525
	234	2.84	286	546	0.82	266	510	3.66	276	528
	235	2.43	283	542	0.99	271	520	3.42	277	531
	236	2.06	281	538	1.20	275	527	3.26	278	532
	237	1.73	278	532	1.44	279	534	3.17	278	533
	238	1.44	277	530	1.73	282	540	3.17	279	535
	239	1.20	274	525	2.06	286	546	3.26	280	536
	241	0.99	271	520	2.43	288	550	3.42	279	535
	240	0.82	267	512	2.84	289	552	3.66	278	532
	242	0.67	264	508	3.28	289	552	3.95	279	530
	243	4.87	281	538	1.01	293	560	5.88	287	549
	244	3.65	282	540	1.49	295	563	5.14	289	552
	245	2.60	281[c]	537[c]	2.17	296[c]	565[c]	4.77	288	551
	246	2.17	279	535	2.60	296	565	4.77	288	550
	247	1.49	274	525	3.65	292	558	5.14	283	542
	248	1.01	268	514	4.87	289	552	5.88	278	533
	249	3.07	267	513	0.64	278	532	3.71	272	522
	250	2.32	267	512	0.94	280	536	3.26	273	524

Table 4.3 (continued)

Specimen type[a]	Specimen No.	Forward position			Reverse position			Total fluence (10^{22} neutrons/m^2)[b]	Median temperature	
		Fluence (10^{22} neutrons/m^2)[b]	Temperature (°C)	Temperature (°F)	Fluence (10^{22} neutrons/m^2)[b]	Temperature (°C)	Temperature (°F)		(°C)	(°F)
C_v	65W-251	1.65	266	510	1.38	282	540	3.03	274	525
	252	1.38	266	510	1.65	282	540	3.03	274	525
	253	0.94	266	510	2.32	280	536	3.26	273	523
	254	0.64	266	511	3.07	277	530	3.71	371	520
	255	2.10	294	561	2.19	273	524	4.29	283	542
	256	1.83	294	561	1.91	273	524	3.74	283	542
	257	2.42	294	561	2.37	273	524	4.79	283	542
	258	2.22	294	562	2.17	273	524	4.39	284	543
	259	2.00	294	562	1.96	273	524	3.96	284	543
	260	1.71	294	561	1.68	273	524	3.39	283	542
	262	2.44	294	561	2.24	273	524	4.68	283	542
	261	2.24	294[c]	562[c]	2.06	273[c]	524[c]	4.30	284	543
	263	2.02	294	562	1.85	273	524	3.87	284	543
	264	1.73	294[c]	561[c]	1.58	273[c]	524[c]	3.31	283	542
	265	2.35	294	561	2.03	273	524	4.38	283	542
	266	2.14	294	561	1.85	273	524	3.99	283	542
	267	1.87	294	561	1.61	273	524	3.48	283	542
	268	1.33	269	516	2.21	298	568	3.54	283	542
	269	1.20	269	516	1.99	298	568	3.19	283	542
	270	1.43	269	516	2.54	298	568	3.97	283	542
	271	1.32	270	518	2.34	299	571	3.66	284	544
	272	1.19	270	518	2.12	299	571	3.31	284	544
	273	1.06	269	516	1.90	298	568	2.96	283	542
	274	1.35	269	516	2.57	298	568	3.92	283	542
	275	1.25	270[c]	518[c]	2.37	299[c]	571[c]	3.62	284	544
	276	1.13	270	518	2.14	299	571	3.27	284	544
	277	1.01	369[c]	516[c]	1.92	298[c]	568[c]	2.93	283	542
	278	1.24	269	516	2.50	290	568	3.74	283	542
	279	1.12	269	516	2.27	290	568	3.39	283	542
	280	1.01	269	516	2.05	290	568	3.06	283	542
	281	1.68	284	543	1.75	274	526	3.43	279	534
	284	1.51	284	543	1.58	274	526	3.09	279	534
	287	1.94	284	543	1.89	274	526	3.83	279	534
	290	1.79	285	545	1.74	276	528	3.53	288	536
	293	1.62	285	545	1.58	276	528	3.20	288	536
	296	1.45	284	543	1.41	274	526	2.86	279	534
	299	1.95	284	543	1.79	274	526	3.74	279	534
	302	1.79	285	545	1.65	276	528	3.44	288	536
	305	1.62	285	545	1.49	276	528	3.11	288	536
	308	1.45	284[c]	543[c]	1.33	274[c]	526[c]	2.78	279	534
	311	1.89	284	543	1.63	274	526	3.52	279	534
	314	1.72	284	543	1.48	274	526	3.20	279	534
	317	1.54	284	543	1.33	274	526	2.87	279	534
PCC_v	65W-200C	4.27	282	540	1.23	294	562	5.50	288	551
	201C	3.10	282	540	1.80	296	564	4.90	286	552
	202C	1.80	277	530	3.10	294	562	4.90	286	546
	203C	1.23	269[c]	517[c]	4.27	289[c]	553[c]	5.50	282	540
	204C	2.71	267	513	0.78	279	534	3.49	273	524
	205C	1.97	266	511	1.14	281	538	3.11	273	524
	206C	1.14	266	510	1.97	281	538	3.11	273	524
	207C	0.78	266	511	2.71	278	533	3.49	272	522
Tensile	65W-4	5.44	293	560	2.20	266	510	7.64	279	535
	5	2.20	277	530	5.44	292	558	7.64	284	544
	6	1.39	285	545	0.57	291	555	1.96	288	550
	7	0.57	277	530	1.39	296	565	1.96	287	548
	8	4.27	262	504	1.74	274	526	6.01	268	515
	9	1.74	266	510	4.27	274	525	6.01	270	518
	1	2.30	294	561	2.43	273	524	4.73	283	542
	2	1.46	269	516	2.93	290	568	4.39	283	542
	3	1.85	284	343	1.94	274	526	3.79	281	538

[a]CS—compact specimen; C_v—standard Charpy V-notch impact specimen; PCC_v—precracked Charpy V-notch specimen; tensile—0.178-in. gage diameter.
[b]10^{22} neutrons/m^2 = 10^{18} neutrons/cm^2, $E > 1$ MeV.
[c]Thermocouples were located at these coordinate sites; other temperature readings were interpolated.

Table 4.4. Third 4T CT irradiation experiment (HSST-BSR-2) capsule C. Fast neutron fluences and median irradiation temperatures for specimens from weldments 66W and 67W

Specimen type[a]	Specimen No.	Forward position			Reverse position			Total fluence (10^{22} neutrons/m^2)[b]	Median temperature	
		Fluence (10^{22} neutrons/m^2)[b]	Temperature (°C)	(°F)	Fluence (10^{22} neutrons/m^2)[b]	Temperature (°C)	(°F)		(°C)	(°F)
1.6T CS	66W-31	3.88	292[c]	558[c]	4.66	269[c]	517[c]	8.54	281	538
	32	6.73	314[c]	597[c]	2.71	267[c]	512[c]	9.44	290	554
0.8T CS	66W-41	6.97	316	600	3.33	268	514	10.30	292	557
	40	6.81	316	600	3.41	268	514	10.22	292	557
	67W-42	3.41	279[c]	535[c]	6.81	289[c]	553[c]	10.22	284	544
	43	3.33	279[c]	535[c]	6.97	289[c]	553[c]	10.30	284	544
0.5T CS	66W-116	7.09	297[c]	566[c]	1.87	272[c]	521[c]	8.96	284	544
	117	4.16	294	561	3.47	283	541	7.63	288	551
	119	1.87	277	530	7.09	286	546	8.96	281	538
	120	6.30	287	549	1.66	271	519	7.96	279	534
	125	3.69	284[c]	544[c]	3.08	282[c]	539[c]	6.77	283	542
	126	1.66	268	515	6.30	284	544	7.96	277	530
	127	4.30	273[c]	523[c]	0.97	260[c]	500[c]	5.27	267	512
	132	2.51	270[c]	518[c]	1.80	271[c]	520[c]	4.31	271	519
	133	1.11	253[c]	487[c]	3.68	274[c]	525[c]	4.79	263	506
	134	3.68	273	523	1.11	260	500	4.79	267	512
	139	2.15	270	518	2.09	271	520	4.24	271	519
	140	0.97	253	487	4.30	274	525	5.27	263	506
	67W-121	2.09	263[c]	505[c]	0.47	257[c]	495[c]	2.56	260	500
	122	1.21	258[c]	496[c]	0.87	256[c]	493[c]	2.08	257	494
	123	0.54	252	485	1.78	249	480	2.32	250	482
	126	1.78	263	505	0.54	257	495	2.32	260	500
	124	1.04	258	496	1.01	256	493	2.05	257	494
	127	0.47	252	485	2.09	249	480	2.56	250	482
	128	5.98	288	551	0.96	247	477	6.94	268	514
	129	6.74	289[c]	552[c]	1.09	248[c]	479[c]	7.83	268	515
	130	7.18	288	551	1.16	247	477	8.34	268	514
	131	3.11	284	544	2.01	260	500	5.12	272	522
	132	3.50	286[c]	546[c]	2.26	261[c]	501[c]	5.76	273	523
	133	3.73	284[c]	544[c]	2.41	260[c]	500[c]	6.17	272	522
	134	1.44	264	507	3.73	261	501	5.17	262	504
	135	1.63	264[c]	508[c]	4.20	261[c]	501[c]	5.83	263	505
	136	1.73	264	507	4.48	261	501	6.21	262	504
	66W-141	4.48	276	528	1.78	286	546	6.26	281	537
	146	4.20	276[c]	528[c]	1.67	286[c]	546[c]	5.87	281	537
	147	3.73	276	528	1.48	286	546	5.21	281	537
	148	1.05	249[c]	481[c]	7.83	312[c]	593[c]	8.88	281	537
	153	6.21	296	564	0.97	264	507	7.18	280	536
	154	5.43	296[c]	564[c]	0.85	264[c]	507[c]	6.28	280	536
	155	4.53	296	564	0.71	264	507	5.24	280	536
	157	1.32	284[c]	544[c]	4.05	260[c]	500[c]	5.37	272	522
	67W-138	3.77	269	517	1.50	286	546	5.27	278	532
	139	3.30	269[c]	517[c]	1.31	286[c]	546[c]	4.61	278	532
	140	2.75	269	517	1.09	286	546	3.84	278	532
	141	0.88	266[c]	511[c]	6.70	289[c]	553[c]	7.58	278	532
Cv	66W-215	5.18	274	526	1.05	258	496	6.23	266	511
	216	4.46	274	525	1.28	261	502	5.74	268	514
	217	3.81	273	524	1.56	266	510	5.37	269	517
	218	3.24	272	522	1.89	269	517	5.13	271	520
	219	2.71	271	520	2.27	272	522	4.98	272	521
	220	2.27	268	515	2.71	273	523	4.98	271	519
	221	1.89	264	508	3.24	274	526	5.13	269	517
	222	1.56	261	502	3.81	275	527	5.37	268	514
	223	1.28	254	490	4.46	276	528	5.74	265	509
	224	1.05	250	482	5.18	276	528	6.23	263	505
	67W-203A	7.34	286	546	1.49	280	536	8.83	283	541
	206A	5.40	286	547	2.20	282	540	7.60	284	544
	207A	3.85	286[c]	546[c]	3.21	284[c]	543[c]	7.06	284	544
	226	3.21	285	545	3.85	284	543	7.06	284	544
	227	2.20	283	541	5.40	284	544	7.60	283	542
	232	1.49	281	538	7.34	283	542	8.83	282	540
	233	3.70	271	520	0.75	267	512	4.45	269	516
	234	2.72	271	520	1.11	268	515	3.83	270	518

Table 4.4 (continued)

Specimen type[a]	Specimen No.	Forward position			Reverse position			Total fluence (10^{22} neutrons/m^2)[b]	Median temperature	
		Fluence (10^{22} neutrons/m^2)[b]	Temperature (°C)	(°F)	Fluence (10^{22} neutrons/m^2)[b]	Temperature (°C)	(°F)		(°C)	(°F)
C_v	67W-235	1.94	271	520	1.62	269	517	3.56	270	518
	240	1.62	271	519	1.94	269	517	3.56	270	518
	241	1.11	269	516	2.72	270	518	3.83	269	517
	242	0.75	267	512	3.70	269	517	4.45	268	514
	66W-211	2.16	261	501	3.92	308	587	6.08	284	544
	212	1.88	261	501	4.18	308	587	6.06	284	544
	213	1.78	261	501	3.96	308	587	5.74	284	544
	214	1.65	261	501	3.66	308	587	5.21	284	544
	225	2.36	292	557	2.23	266	511	4.89	279	534
	226	2.85	292	557	2.50	266	511	5.35	279	534
	227	2.54	293	559	2.23	267	513	4.77	280	536
	228	2.22	293	559	1.94	267	513	4.16	280	536
	229	1.89	292	557	1.66	266	511	3.55	279	534
	230	2.87	292	557	2.36	266	511	5.23	279	534
	231	2.56	293[c]	559[c]	2.10	267[c]	513[c]	4.66	280	536
	232	2.23	293	559	1.83	267	513	4.06	280	536
	233	1.91	292[c]	557[c]	1.56	266[c]	511[c]	3.47	279	534
	234	2.69	292	557	2.08	266	511	4.77	279	534
	290A	2.38	292	557	1.84	266	511	4.22	279	534
	67W-243	2.06	292	557	1.59	266	511	3.65	279	534
	248	1.70	270	518	3.10	294	561	4.80	282	540
	249	1.91	270	518	3.73	294	561	5.64	282	540
	250	1.70	270	518	3.33	294	561	5.03	282	540
	251	1.48	270	518	2.90	294	561	4.38	282	540
	256	1.27	270	518	2.48	294	561	3.75	282	540
	257	1.80	270	518	3.77	294	561	5.57	282	540
	258	1.60	270[c]	518[c]	3.36	294[c]	561[c]	4.96	282	540
	259	1.40	270	518	2.93	294	561	4.33	282	540
	264	1.19	270[c]	518[c]	2.50	294[c]	561[c]	3.69	282	540
	265	1.59	270	518	3.53	294	561	5.12	282	540
	266	1.41	270	518	3.12	294	561	4.53	282	540
	267	1.22	270	518	2.70	294	561	3.92	282	540
PCC_v	67W-200C	6.31	286	546	1.82	281	538	8.13	283	541
	201C	4.55	286	547	2.66	283	542	7.21	284	544
	203C	2.66	284	543	4.55	284	544	7.21	284	544
	208C	1.82	282[c]	539[c]	6.31	284[c]	543[c]	8.13	283	541
	210C	3.18	271	520	0.92	268	514	4.10	269	517
	211C	2.29	271	520	1.34	269	516	3.63	270	518
	217C	1.34	270	518	2.29	270	518	3.63	270	518
	218C	0.92	268	514	3.18	270	518	4.10	269	516
	66W-201C	2.19	261	501	4.29	308	587	6.48	284	544
	202C	2.08	261	502	4.07	310	590	6.15	286	546
	203C	1.95	261	502	3.81	310	590	5.76	286	546
	204C	1.78	261	501	3.48	308	587	5.26	284	544
	205C	2.07	261	501	4.33	308	587	6.40	284	544
	207C	1.96	261[c]	502[c]	4.10	310[c]	590[c]	6.06	286	546
	209C	1.84	261	502	3.84	310	590	5.68	286	546
	206C	1.68	261[c]	501[c]	3.51	308[c]	587[c]	5.19	284	544
Tensile	66W-11	6.22	297	566	2.52	274	525	8.74	286	546
	12	2.52	274	525	6.22	288	550	8.74	281	538
	67W-17	1.27	288	550	0.51	281	538	1.78	284	544
	18	0.51	285	545	1.27	287	548	1.78	286	546
	15	6.74	264	507	2.73	258	497	9.47	261	502
	16	2.73	253	488	6.74	250	482	9.47	252	485
	66W-3	2.28	261	501	4.14	308	587	6.42	284	544
	5	2.67	292	557	2.52	266	511	5.19	279	534
	67W-4	1.92	270	518	3.50	294	561	5.42	282	540
	66W-4	1.99	261	501	3.63	308	587	5.62	284	544
	9	2.04	292	557	1.93	266	511	3.97	279	534
	67W-9	1.47	270	518	2.68	294	561	4.15	282	540

[a]CS—compact specimen; C_v—standard Charpy V-notch impact specimen; PCC_v—precracked Charpy V-notch specimen; tensile—0.178-in. gage diameter

[b]10^{22} neutrons/m^2 = 10^{18} neutrons/cm^2, E > 1 MeV.

[c]Thermocouples were located at these coordinate sites; other temperature readings were interpolated.

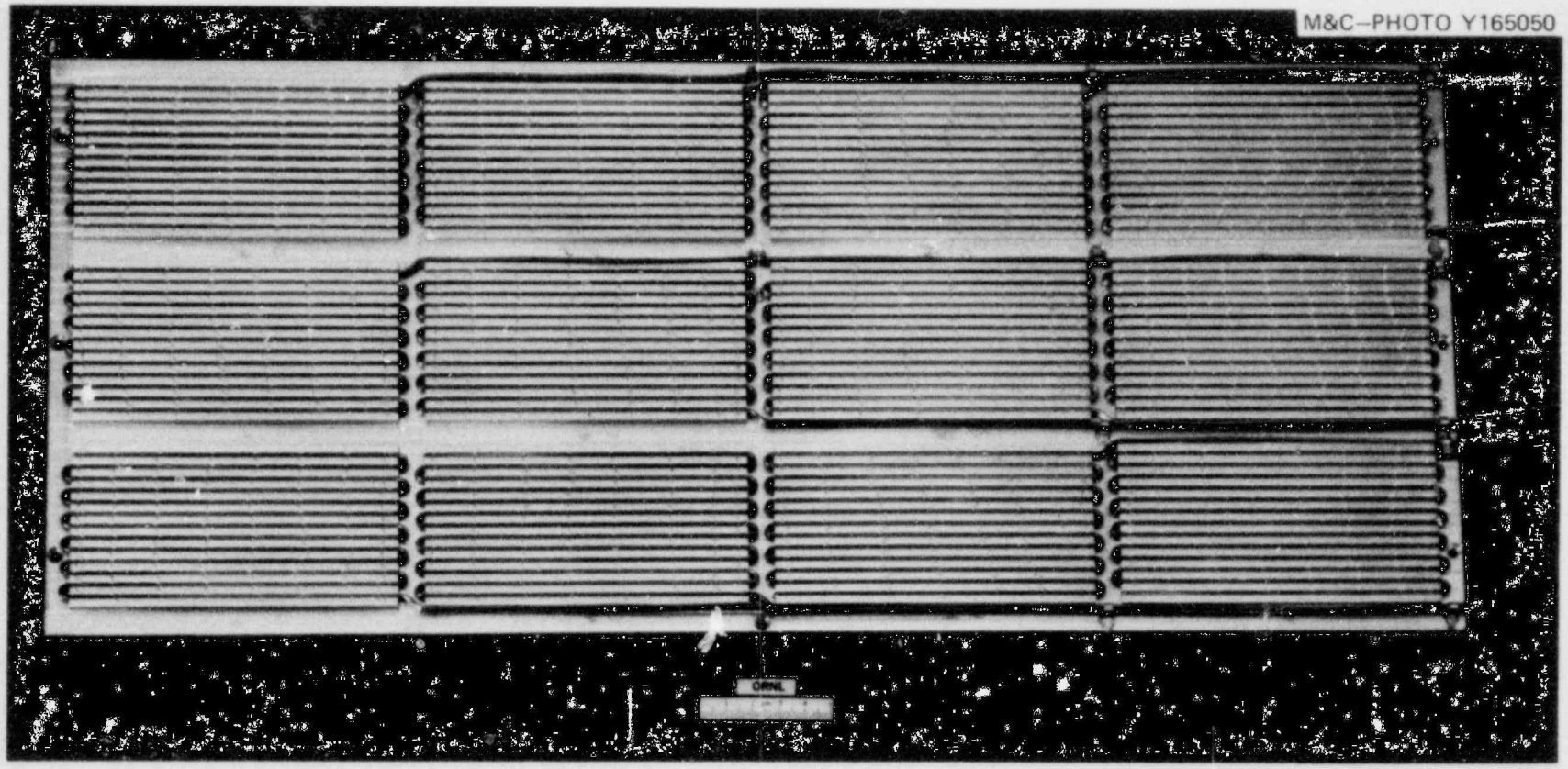

Fig. 4.4. Heater plate for fourth HSST irradiation series capsules with heaters installed.

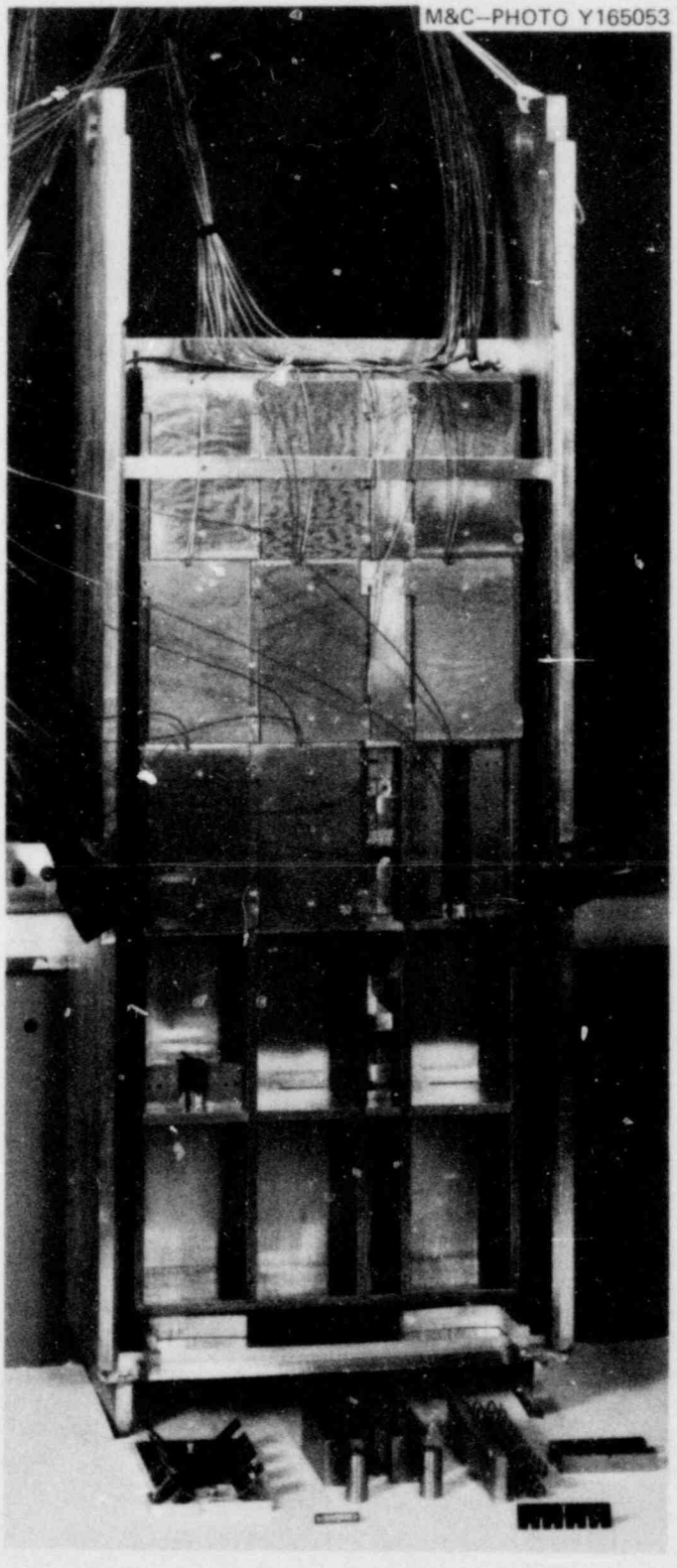

Fig. 4.5. Assembly of capsule for fourth HSST irradiation series.

4.2 Fracture Toughness of Irradiated Welds 61W, 62W, and 63W*

J. A. Williams† K. W. Carlson†

The materials of interest were from the second 4T irradiations conducted by ORNL. A weld of ASTM A533 grade B class 1 steel plate (weld 61W) and the two welds of A508 class 1 forging (welds 62W and 63W) were evaluated.

The toughness vs temperature curves were developed using 12.7-mm-thick compact specimens. Because all specimens in the temperature range of testing were invalid by ASTM E 399,[4] the specimens were analyzed by J-integral test and analysis methods.[5,6] Test temperatures were nominally in the range of 25 to 93°C to develop transition data and at 177 and 260°C to provide upper-shelf toughness information.

4.2.1 Testing and analysis

A minicomputer system used for data acquisition and computations was programmed to accurately measure load and displacements, compute the compliance, and assess the accuracy of compliance measurements. Real-time computations of the compliance, crack length, and estimated J values were made and printed at the time of each unloading; all data were stored on a magnetic disk. Concurrently, the computer-controlled x-y plotter produced a load-deflection record. On completion of the tests, temporary processing was completed by the computer. After subsequent crack length measurements were made from the broken specimen, the data were recalled from the magnetic disk and were reprocessed, and the r curve was plotted. Reprocessed results were then refiled on the magnetic disk.

Test method. The fracture toughness tests of this study were conducted using the procedure given below. Calibrations of all test machines, measuring devices, and data-indicating and -recording devices are directly traceable to the National Bureau of Standards (NBS).

The tests were conducted as follows.

1. Specimens were visually examined for their general appearance and integrity.
2. Specimens were loaded into the test machine. During this step, load-line extensometers and thermocouples were attached to the specimen, and the specimens were aligned in the specimen grips. Shims were used to ensure centering of specimen in grips; shims were subsequently removed after setting a small preload (8.76 N/mm of thickness) on the specimen. Preload was necessary for maintaining alignment of the test specimen and was accounted for within the computer program.
3. A "Test-Ready" analysis was conducted at room temperature. The following steps were included.
   a. System stability analysis was conducted by sampling the load signal and load-line extensometer systems. For each signal, 100 readings were taken, and a 95% confidence limit on the signal stability was obtained. Generally, the 95% confidence level of stability was 20 N or better for load, 0.38 μm or better for the dual LVDT load-line extensometer, 2.0 μm or better for the clip gage load-line extensometer.
   b. Ten unloadings were conducted at low elastic load. Approximately 250 load-deflection pairs were taken and analyzed by the computer to determine the compliance of each unloading.

*Research performed under Purchase Order 11Y-50917V for the Oak Ridge National Laboratory, operated by Union Carbide Corporation Nuclear Division.

†Hanford Engineering Development Laboratory.

c. Computer analysis determined the mean and standard deviations of compliances and crack lengths for the ten unloadings, as indicated by each load-line extensometer used on the system.
d. When standard deviations of calculated crack length of less than 25 μm were obtained for the dual LVDT load-line extensometer system, a "Test-Ready" condition was considered to exist. The clip-gage-system standard deviation was generally in the range of 130 μm or less. Irradiated test specimens of this series had machined knife edges, which are unsuitable for obtaining highly reproducible (low standard deviation on calculated crack length) clip-gage results and therefore were considered unreliable indicators of "Test-Ready" conditions. Standard deviations of less than 25 μm have been achieved on 25-mm-thick compact specimens using clip-gage systems seated on razor blade knife edges attached to the specimen.

4. The specimen was heated to test temperature. Soak time of specimen was 0.04 h/mm of specimen thickness in the furnace at test temperature.

5. After attaining test temperature, the "Test-Ready" analysis is repeated [see item (3) above].

6. With a positive "Test-Ready" indication, the test was started. An initial unloading at the same load level of the "Test-Ready" analysis was conducted, and, if the measured crack length was within the 95% confidence limit of the "Test-Ready" analysis, the testing was continued.

   a. For tests being conducted in the transition region, no further unloadings were necessary. The test loading was continued to first pop-in or unstable fracture. If unstable fracture occurred without arrest, the test was terminated. If pop-in or unstable fracture with arrest was observed, the specimen was unloaded, the unloading compliance data were obtained, and the test unloading was completed, at which time the test was terminated.
   b. For tests conducted on the upper shelf, unloading compliance procedures were continued incrementally throughout the course of the test. The number of unloadings conducted ranged from 20 to 25. Real-time computer analysis of the unloadings gave J and Δa printouts for monitoring the progress of the tests.

7. Posttest measurements of initial crack length and the final crack extension were made from the fracture surfaces of specimens after heat tinting at 340°C and fracturing at low temperature. Crack length measurements of irradiated specimens were made from enlarged photographs of the fracture surfaces.

Calculations of fracture toughness parameters for both unstable and stable crack growth are described in the following paragraphs. All calculations were made using the minicomputer fracture toughness processing programs developed at Hanford Engineering Development Laboratory (HEDL).

J-integral calculations. To compute J for the compact specimens, the formula developed by Rice et al.[7] modified for the tensile component of load after Merkle and Corten,[6] and shortened by the ASTM Task Group E24.01.09[5] was used. This equation is

$$J = \frac{2A}{Bb}\,\frac{(1+\alpha)}{(1+\alpha^2)}, \tag{1}$$

where

$$\alpha = \left[\left(\frac{2a_o}{b}\right)^2 + \frac{4a_o}{b} + 2\right]^{1/2} - \left(\frac{2a_o}{b} + 1\right), \tag{2}$$

A = area (energy) under the load-deflection record,

b = thickness (net section thickness for face-grooved specimens),

b = remaining uncracked ligament,

a_0 = initial crack length.

Compliance-based crack-length calculations. The compliance equation developed by Saxena and Hudak[8] was used to calculate the crack length from the measured compliance data of clip-gage load-line extensometers. An experimentally determined crack-length compliance equation was used for analysis of dual LVDT load-line extensometer compliance measurements.

The initial crack length was computed from the mean of ten compliance measurements at very low load levels. Crack extension (Δa) was computed by subtracting this value from subsequent computed crack lengths.

J-R curve analysis. The intersection of the lines representing crack blunting and crack extension was taken as the J_{Ic} value. The blunting line was taken as following the relationship

$$\Delta a = (J/2)\,\sigma_0 \text{ for } \sigma_0 = \text{flow stress} = \frac{\sigma_y + \sigma_u}{2} , \tag{3}$$

where σ_y is the yield strength and σ_u is the ultimate strength. Data points utilized for the construction of the crack extension line were those contained in an interval defined by offset lines parallel to the blunting line [Eq. (3)], offset 0.5 and 1.8 mm "ahead" of the blunting line. The crack extension portion of the r-curve was a least-squares linear regression through these points. Nominally, Ref. 6 recommends a range between 0.15- and 1.5-mm offset. The larger offsets were used because of the consistent behavior of unloading compliance blunting data to exhibit greater apparent crack blunting than predicted by the theoretical blunting line. Inclusion of these points (between 0.15 and 0.5 mm) would have yielded inordinately low toughness values.

Tearing modulus. After Paris et al.,[9] the tearing modulus T was calculated

$$T = \frac{dJ}{da}\left(\frac{E}{\sigma_o^2}\right) , \tag{4}$$

where

dJ/da = slope of the crack extension line,

E = modulus of elasticity,

σ_o = flow stress.

Stress-intensity calculations. Stress-intensity calculations were made for tests that exhibited unstable crack extension by the equation of Rice[10] for small-scale yielding,

$$K_I^2 = \frac{JE}{1-\nu^2} , \tag{5}$$

where ν is Poisson's ratio and J is determined by Eq. (1) for the area under the curve to unstable fracture. Equation (5) was also used for the calculation of critical stress intensity from J_{Ic} determined by J-R curve methods. The value of critical stress intensity determined by Eq. (5) is reported in the tabulations as K_J to avoid confusion with the K_{Ic} calculation by ASTM E 399 methods.

Physical crack measurements. After completion of the test, specimens were heat tinted in a furnace at 340° C and then fractured after cooling in liquid nitrogen. The blue oxide coating clearly delineates the fatigue crack and crack extension. Crack measurements were made at nine equally spaced points along the fatigue crack front and the final crack front. The crack measurement was taken as the mean of eight points: the seven interior measurements plus the average of the two surface measurements. The initial crack length as measured on the specimen fracture surface was used to recompute the J values.

4.2.2 Results

The results of the fracture toughness studies of welds 61W, 62W, and 63W are given in Tables 4.5, 4.6, and 4.7, respectively.

After irradiation, the fracture properties of all three welds appear to be very similar, as shown in Figs. 4.6 through 4.8. Upper transition occurs between 25 and 75° C for all materials, and upper-shelf

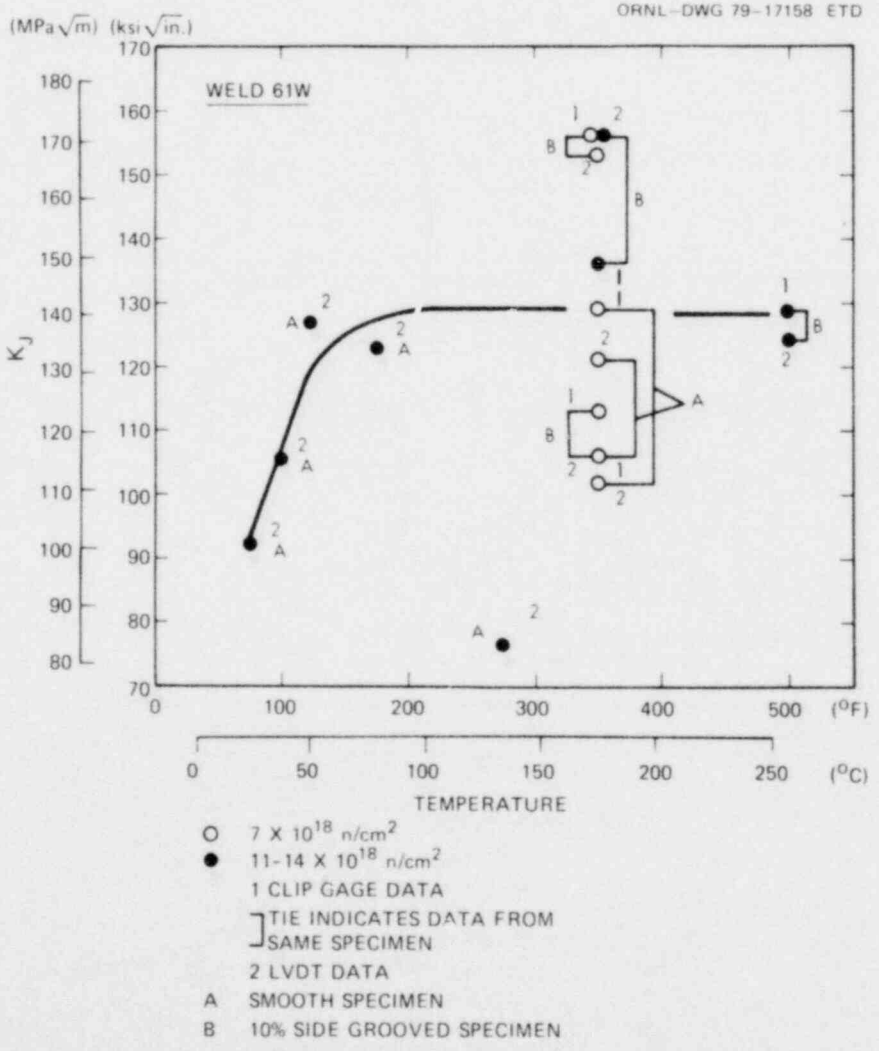

Fig. 4.6. Toughness vs temperature curve for weld 61W.

Table 4.5. Fracture toughness of irradiated A533 weld 61W

Specimen No.	Irradiation fluence (10^{18} neutrons/cm^2) (E > 1 MeV)	Irradiation temperature (°C)		Test temperature (°C)	K_J (MPa·$\sqrt{m}$)[a]	J_{Ic} (kJ/m^2)[a]	T[a]	$25(J_{Ic}/\sigma_{flow})$ (mm)[a]	Test conditions[b]
		Forward position	Reverse position						
Smooth Specimens									
61W-104	11 (8/3)	291-293	299-304	26	101	44		1.5	1,4,8,11
61W-103	14 (3/11)	302-310	316-324	37	115	58		2.3	1,4,8,11
61W-112	12 (9/3)	302-307	288-307	52	140	85		3.3	1,5,8,11
61W-106	12 (10/2)	291-293	299-304	79	135	80		3.0	1,5,8,11
61W-113	11 (8/3)	302-307	288-307	135	84	31	73	1.3	1,6,8,12
10% Side-Grooved Specimens									
61W-123	16 (13/3)	288-299	288-299	177	150/171	101/133	48/51	4.1/5.3	3,6,10,12
61W-124	14 (3/11)	277-288	277-288	260	142/136	94/86	45/48	3.8/3.6	3,6,10,12
Low-Fluence Smooth Specimens									
61W-125	7 (4/3)	293-304	293-302	177	142/112	91/56	53/61	3.8/2.3	2,6,10,12
61W-126	7 (4/3)	293-304	293-302	177	117/133	61/79	79/75	2.5/3.3	2,6,10,12
Low-Fluence 10% Side-Grooved Specimens									
61W-127	7 (4/3)	293-304	293-304	177	171/168	133/127	56/67	5.2/5.1	3,6,10,12
61W-128	7 (4/3)	293-304	288-299	177	124/117	69/61	60/63	2.8/2.5	3,6,10,12

[a]Where two values are given, the first value is from clip gage data and the second is from LVDT data.

[b]Test conditions are as follows (for Tables 4.5 through 4.7):

1. Standard CT specimen.
2. J-modified specimen.
3. J-modified specimen, 10% side grooves.
4. Unstable fracture.
5. Unstable fracture-arrest.
6. Stable crack extension.
7. Calculated at maximum specimen load where noted in the table.
8. LVDT data only.
9. Clip gage data only.
10. Clip gage data/LVDT data.
11. J_{Ic} and K_J determined from crack instability.
12. J_{Ic} and K_J determined from R-curve.

Table 4.6. Fracture toughness of irradiated weld 62W

Specimen No.	Irradiation fluence (10^{18} neutrons/cm^2) (E > 1 MeV)	Irradiation temperature (°C)		Test temperature (°C)	K_J (MPa·$\sqrt{m}$)[a]	J_{Ic} (kJ/m^2)[a]	T[a]	$25(J_{Ic}/\sigma_{flow})$ (mm)[a]	Test conditions[b]
		Forward position	Reverse position						
Smooth Specimens									
62W-117	12 (7/5)	288-296	296-310	25	119	60		2.3	1,4,8,11
62W-152	12 (10/2)	277-288	293-299	37	103	49		1.8	1,4,8,11
62W-120[c]	10 (8/2)	291-299	285-293	52	148,g				1,7,8
62W-119[c]	10 (8/2)	291-299	285-293	66	155,g				1,7,8
10% Side-Grooved Specimens									
62W-106	12 (10/2)	291-302	302-310	177	147/166	97/124	90/86	4.1/5.1	3,6,10,12
62W-159	11 (1/10)	277-288	299-310	260	134/113	84/59	58/62	3.5/2.5	3,6,10,12

[a]Where two values are given, the first value is from clip gage data and the second is from LVDT data.

[b]Test conditions are defined in Table 4.5, footnote b.

[c]The value of K_J was determined from the analysis of the area under the load-deflection curve to maximum load. These values do not represent crack initiation for specimens 62W-120 and 62W-119. Examination of fracture surfaces of both specimens indicates small amounts of stable crack extension and, therefore, represents upper bounds of the fracture toughness at the temperatures indicated. The test of 62W-120 was stopped at maximum load and 62W-119 just after maximum load because no unstable crack extension had occurred.

Table 4.7. Fracture toughness of irradiated weld 63W

Specimen No.	Irradiation fluence (10^{18} neutrons/cm^2) (E > 1 MeV)	Irradiation temperature (°C)		Test temperature (°C)	K_J (MPa·$\sqrt{m}$)[a]	J_{Ic} (kJ/m^2)[a]	T[a]	$25(J_{Ic}/\sigma_{flow})^2$ (mm)[a]	Test conditions[b]
		Forward position	Reverse position						
Smooth Specimens									
63W-100	14 (3/11)	285-302	291-307	24	59	15		0.5	1,5,8,11
63W-101	14 (11/3)	285-302	266-282	52	81	28		1.0	1,5,8,11
10% Side-Grooved Specimens									
63W-135	9 (6/3)	288-304	293-304	93	152	101	53	4.1	3,6,9,12
63W-109	12 (10/2)	296-313	288-304	149	151/157	100/110	72/68	4.1/4.3	3,6,10,12
63W-123	10 (3/7)	293-313	277-282	260	105/103	50/49	49/45	2.3/2.0	3,6,10,12

[a]Where two values are given, the first value is from clip gage data and the second is from LVDT data.

[b]Test conditions are defined in Table 4.5, footnote b.

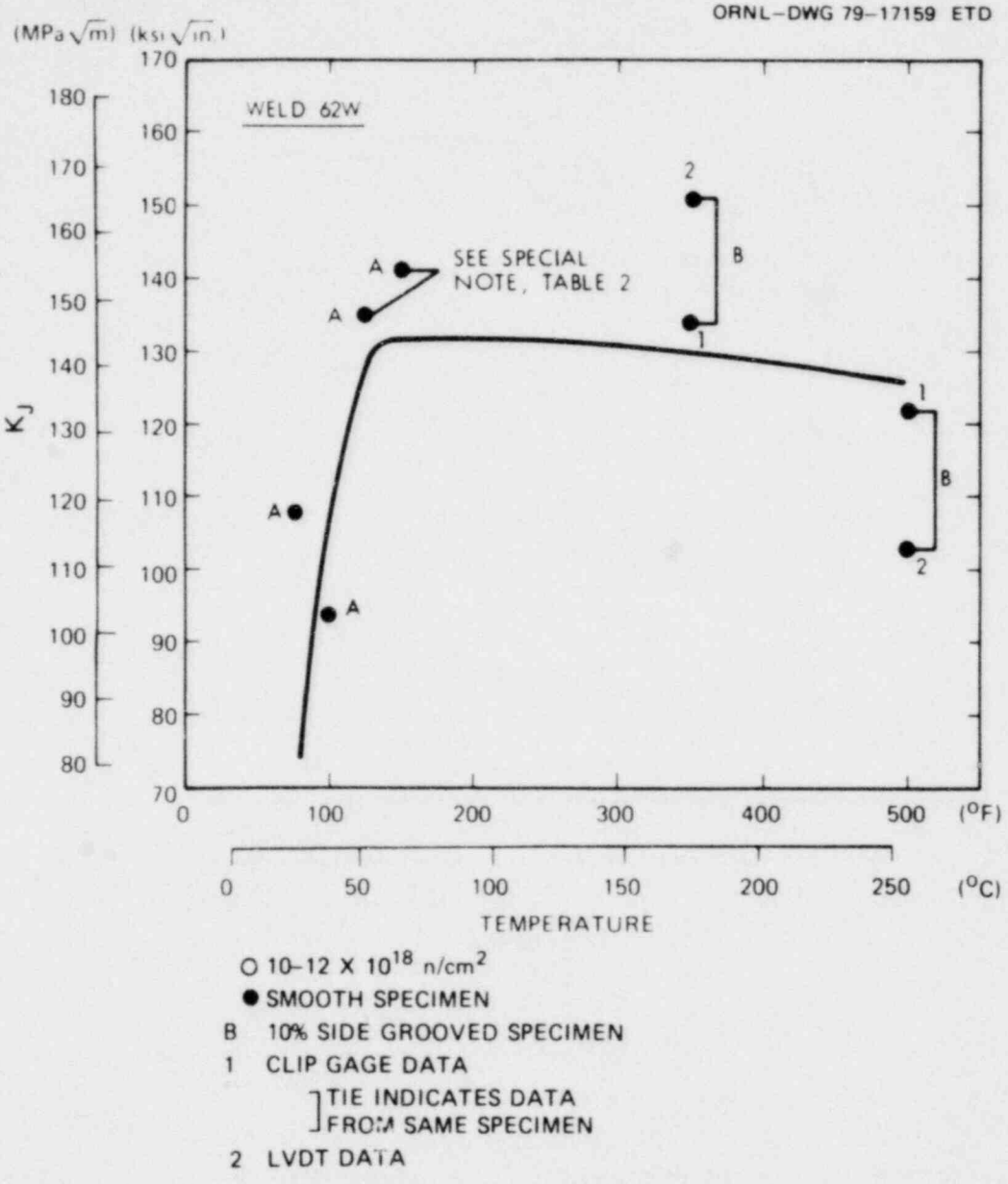

Fig. 4.7. Toughness vs temperature curve for weld 62W.

toughness is in the range of 140 to 150 MPa·$\sqrt{m}$. The degree of transition shift or the reduction in upper shelf due to irradiation cannot be ascertained because no unirradiated data are available for comparison.

We also observed that the degree of scatter, probably caused by material variability, masked any effects that might be attributed to differences in irradiation level or specimen side grooving; specifically, the data of weld 61W, which attempted to show these effects, can be cited. Although not shown here, examination of fracture surfaces of broken specimens failed to show any evidence of beneficial effects of 10% side grooves in producing straight crack fronts.

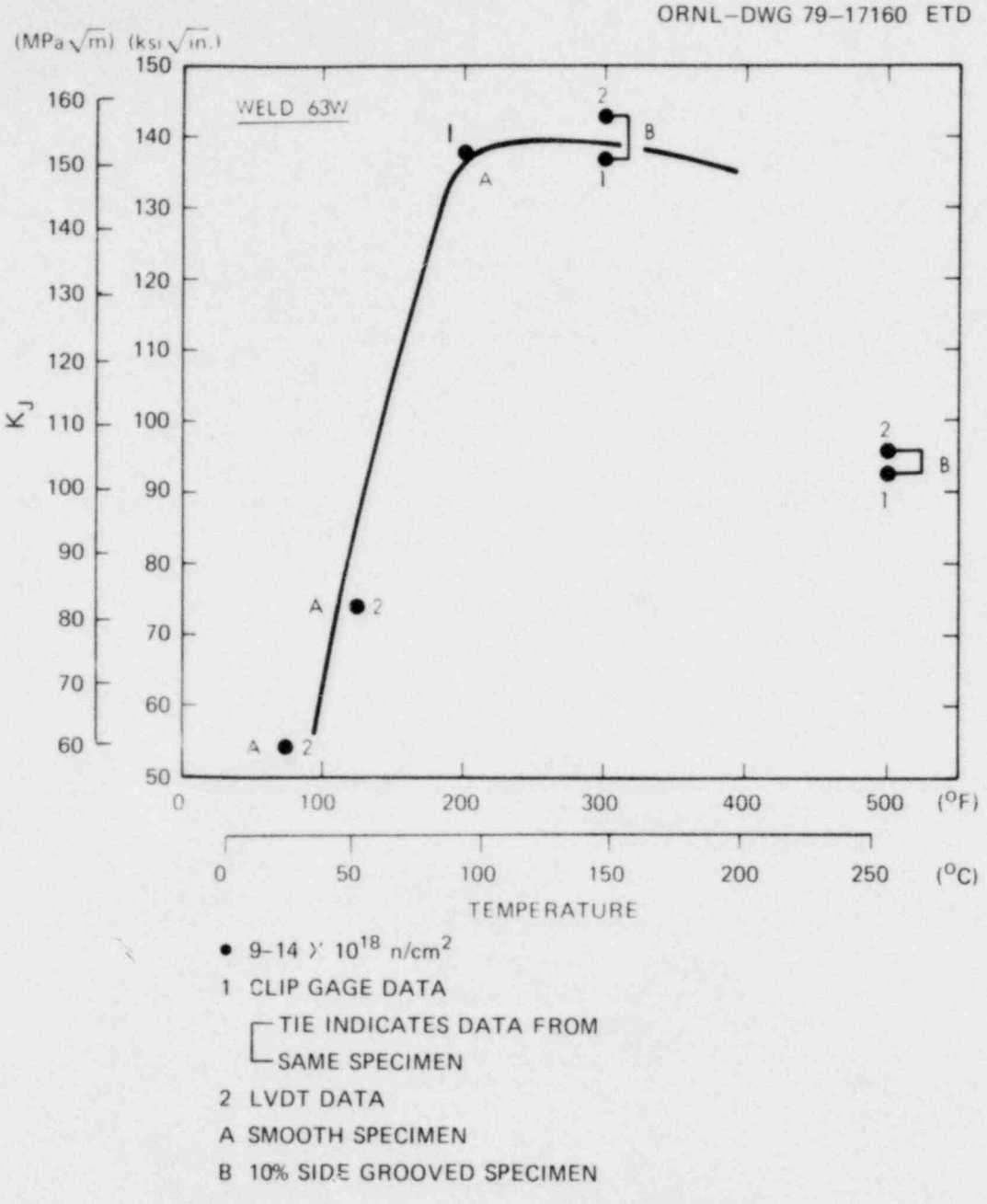

Fig. 4.8. Toughness vs temperature curve for weld 63W.

References

1. R. G. Berggren et al., "Toughness Investigations of Irradiated Materials," *Heavy-Section Steel Technology Program Quart. Prog. Rep. October–December 1977*, ORNL/NUREG/TM-194, p. 36.

2. U.S. Nuclear Regulatory Commission, "Effects of Residual Elements on Predicted Radiation Damage to Reactor Vessel Material," *Regulatory Guide 1.99*, Rev. 1 (April 1977).

3. R. G. Berggren et al., "Toughness Investigations of Irradiated Materials," *Heavy-Section Steel Technology Program Quart. Prog. Rep. January–March 1979*, ORNL/NUREG/TM-324, p. 56.

4. "Plane Strain Fracture Toughness of Metallic Materials," ASTM E 399-78, *Annual Book of ASTM Standards, Part 31,* American Society for Testing and Materials, Philadelphia, Pa. 1978.

5. G. A. Clarke et al., "A Procedure for the Determination of Ductile Fracture Toughness Values Using J-Integral Techniques," *J. Test. Eval.* **7** (1), 49–56 (January 1979).

6. J. G. Merkle and H. T. Corten, "A J-Integral Analysis for the Compact Specimen, Considering Axial Force as Well as Bending Effects," *J. Pressure Vessel Technol.*, American Society of Mechanical Engineers, 1974.

7. J. R. Rice, P. C. Paris, and J. G. Merkle, "Some Further Results of J-Integral Analysis and Estimates," *Progress in Flaw Growth and Fracture Toughness Testing,* ASTM STP 536, 1973, pp. 231–45.

8. A. Saxena and S. J. Hudak, Jr., "Review and Extension of Compliance Information for Common Crack Growth Specimens," Westinghouse Scientific Paper No. 77-9E7-AFCGR-P1, May 1977.

9. P. C. Paris "Instability of the Tearing Mode of Elastic-Plastic Crack Growth," *Elastic-Plastic Fracture*, ASTM STP 668, 1979, pp. 5–26.

10. J. R. Rice, *J. Appl. Mech. Trans.* **35,** 379–86 (June 1968).

5. PRESSURE VESSEL INVESTIGATIONS

R. H. Bryan P. P. Holz
G. C. Robinson G. D. Whitman

Preparations were initiated for an intermediate vessel test to investigate the application of elastic-plastic fracture mechanics (EPFM) to a thick structure, and a preliminary feasibility study of pressurized thermal shock and thermal fatigue tests in intermediate vessels was undertaken.

5.1 Behavior of Flaws in Low-Upper-Shelf Material

The tests of six 152-mm-thick vessels[1-3] with part-circular surface flaws demonstrated the useful application of linear-elastic fracture mechanics (LEFM) to the analysis of flawed vessels for cases in which fracture toughness is low enough that fast fracture precedes the onset of gross yielding in the structure. However, in tests conducted at high transition and upper-shelf temperatures, for which toughness is high, tearing and local plastic instability are important mechanisms associated with failure.

Attempts to apply EPFM methods to the latter types of tests were complicated by extensive yielding and vessel deformations that preceded failure. Further, in the early tests, the means of detecting and measuring stable tearing in a flawed vessel had not been developed. Even so, these tests, which were conducted at 54°C or above, clearly showed that a deeply flawed vessel could sustain through-the-thickness yielding without failing.

All of the intermediate vessel tests involved materials with high-upper-shelf toughness typical of steels in reactor pressure vessels of current design, while some vessels in operating plants contain high-copper welds of lower toughness and greater sensitivity to neutron embrittlement. After some period of operation, the toughness of these welds is expected to be degraded to the extent that practical operating temperature limits may not be definable in accordance with present regulatory guidelines, which essentially would not allow operation of a vessel with a Charpy impact energy upper shelf of less than 68 J. However, no one has actually demonstrated that a vessel with such a low toughness does not have adequate resistance to tearing.

Intermediate test vessel V-8 will be prepared for a test in which flaw behavior in low-upper-shelf material will be investigated at upper-shelf temperature. The test program is expected to reveal the modes of flaw growth and to test the capabilities of EPFM in predicting flaw behavior. In addition, the test will be a direct demonstration of the behavior of a flaw in a thick vessel under conditions that may be typical of some future reactor vessel accident conditions.

The plan for the low-upper-shelf test (test V-8A) is to repair vessel V-8 (Ref. 3), place a longitudinal seam weld of low-upper-shelf toughness in the test section, place a flaw in the weld, and pressurize the vessel at an upper-shelf temperature.

Specifications for the repair and seam weld preparation were developed. The weld will be required to have properties similar to those of irradiated specimens in the second irradiation study.* The upper-shelf impact energy should preferably be in the range 54 to 68 J and the yield strength 448 to 621 MPa. Since these values are not typical of welds being made today in pressure vessel steels, some special welding process may be required. The finished vessel will be stress relieved; the base metal must not be degraded by the process to the extent that the yield strength requirement of the ASME Boiler and Pressure Vessel Code for SA533 class 1 steel would not be satisfied.

---

*See Sect. 4.1.1 and Figs. 4.1 through 4.3 of this report.

The seam weld will be characterized by testing specimens from seam welds made in a cylindrical prolongation of intermediate test vessel V-10. The prolongation welds will be made concurrently with the seam weld in vessel V-8. Tensile, Charpy impact, fracture toughness, J_{Ic}, and r-curve properties will be determined; these will be used to make detailed test plans and to predict the behavior of the flaw.

5.2 Pressurized Thermal Shock and Thermal Fatigue Tests

Steam line break and small-size loss-of-coolant accidents lead to combined thermal and pressure loads that would affect crack propagation differently than would thermal shock alone. Merkle demonstrated that an axial internal crack propagating through the wall under the influence of a severe thermal shock at zero pressure would be stopped by a compressive ligament before penetrating to the outside surface.[4] Some combination of pressure and thermal shock with low toughness hypothetically could lead to a complete penetration of the wall. Thus, an interest exists in experimental study of crack propagation for the combined loading.

The combined loading is also of interest from an entirely different point of view. Cracking in nozzle corner regions of vessels has been observed in several instances in which crack initiation and subcritical crack growth are associated with thermal cycling. The incidence of this type of cracking is of concern because, at some point, repairs must be instituted unless it can be shown that the cracks are harmless. One can reasonably argue, on the basis of analysis, that some thermally induced cracking is limited in depth. However, no experimental demonstration has indicated that this is the case in the structure of interest.

The feasibility of combined pressure and thermal load tests relating to both types of problems has been investigated. The particular concept considered would use vessels of approximately the geometry of the intermediate test vessels that have nozzles. The nozzle corner region would be equipped with flow baffles and channels through which a cooling fluid flows at a controlled rate. With the high stress concentration at the nozzle corner, producing stress-intensity factors high enough to study both thermal shock and thermal fatigue problems of interest appears feasible.

Test facility modifications that would be needed for these types of tests were studied to make a preliminary evaluation of feasibility. The test facility, in addition to present features, would consist of high-pressure pump loops for both hot and cold fluids, a mixing and injection system for the controlled coolant, and system auxiliaries. With this facility, the vessel could be maintained at essentially constant temperatures (except for the test region) between ~ -30 and 300°C. Pressure could be maintained or cycled up to about 70 MPa. Capabilities of the thermal cycling feature have not been defined precisely, but severe single shocks and cyclic frequencies as high as 1/60 Hz are feasible.

References

1. R. W. Derby et al., *Test of 6-in.-thick Pressure Vessels. Series 1: Intermediate Test Vessels V-1 and V-2*, ORNL-4895 (February 1974).

2. R. H. Bryan et al., *Test of 6-in.-thick Pressure Vessels. Series 2: Intermediate Test Vessels V-3, V-4, and V-6*, ORNL-5059 (November 1975).

3. R. H. Bryan et al., *Test of 6-in.-thick Pressure Vessels. Series 3: Intermediate Test Vessel V-8*, ORNL/NUREG-58 (December 1979).

4. J. G. Merkle, "Analysis of Crack Behavior Under Thermal Shock Loading," *Heavy-Section Steel Technology Program Quart. Prog. Rep. July–September 1978*, ORNL/NUREG/TM-275, pp. 3–12.

6. THERMAL SHOCK INVESTIGATIONS

R. D. Cheverton S. E. Bolt
P. P. Holz

6.1 Introduction

During this report period for the Thermal Shock Program, the TSE-5 test cylinder (TSC-1) was tempered, flawed, and instrumented, its inner surface was coated, and TSE-5 was conducted. A posttest analysis was begun, and material characterization for TSC-1 was continued.

6.2 Flaw Preparation in TSC-1

The full-length axial flaw associated with TSE-5 was prepared in TSC-1 by means of the electron-beam (EB)-weld technique, which requires postweld hydrogen charging of the weld to induce cracking. Final development stages of the technique involved preparing the desired TSE-5 EB-weld flaw in the TSC-1 prolongation.[1] With one exception, the EB-weld parameters used for making the weld in TSC-1 were the same as those used for the prolongation. For TSC-1, the focus was sharp +9 rather than +14 to reduce the flaw depth slightly and thus reduce spiking.

Hydrogen charging of the TSC-1 weld was accomplished using a 10% H_2SO_4 solution and a dc current density of $\sim 8 \times 10^{-4}$ A/mm^2. Ultrasonic instrumentation (5-MHz transducers) was used to detect crack formation and depth during the charging process. A period of 79.5 h was required to achieve complete cracking (only 36.75 h were required for the prolongation). Visual observation confirmed the presence of the axially oriented crack and also revealed numerous short cross cracks, the lengths of which were confined to the fusion zone. Cross cracking of this type would be expected because of the nature of the EB-weld–induced residual stress field; these cross cracks were observed during the development stage.

Figure 6.1 shows the EB-weld apparatus and TSC-1 inside the EB-weld box just prior to making the weld. Note that the weld box is the largest of its kind readily available and is barely large enough. This was a consideration in the selection of test cylinder length.

6.3 Instrumentation of TSC-1

6.3.1 Thermocouples

One hundred eighty thermocouples (type K) were used to measure the radial temperature distribution as a function of time in the wall of TSC-1 during TSE-5. The radial distributions were determined at 15 different locations (as shown in Fig. 6.2), and, at each location, 12 thermocouples were used to establish the gradient. These 12 thermocouples are located in a thimble[2] that plugs into a 25.4-mm-diam hole in the wall of TSC-1. Use of 15 of these thimbles distributed uniformly around and along the test cylinder permits a determination of the degree of symmetry in quenching during the thermal shock experiment. All thermocouples were scanned every 2 s at a rate of 10^4 points/s and recorded on tape.

6.3.2 Crack-opening displacement (COD) gages

Nine COD gages in the form of weldable strain gages (Ailtech SG-125) were used to detect sudden crack-opening events, to provide an estimate of actual crack opening, and to measure crack-opening

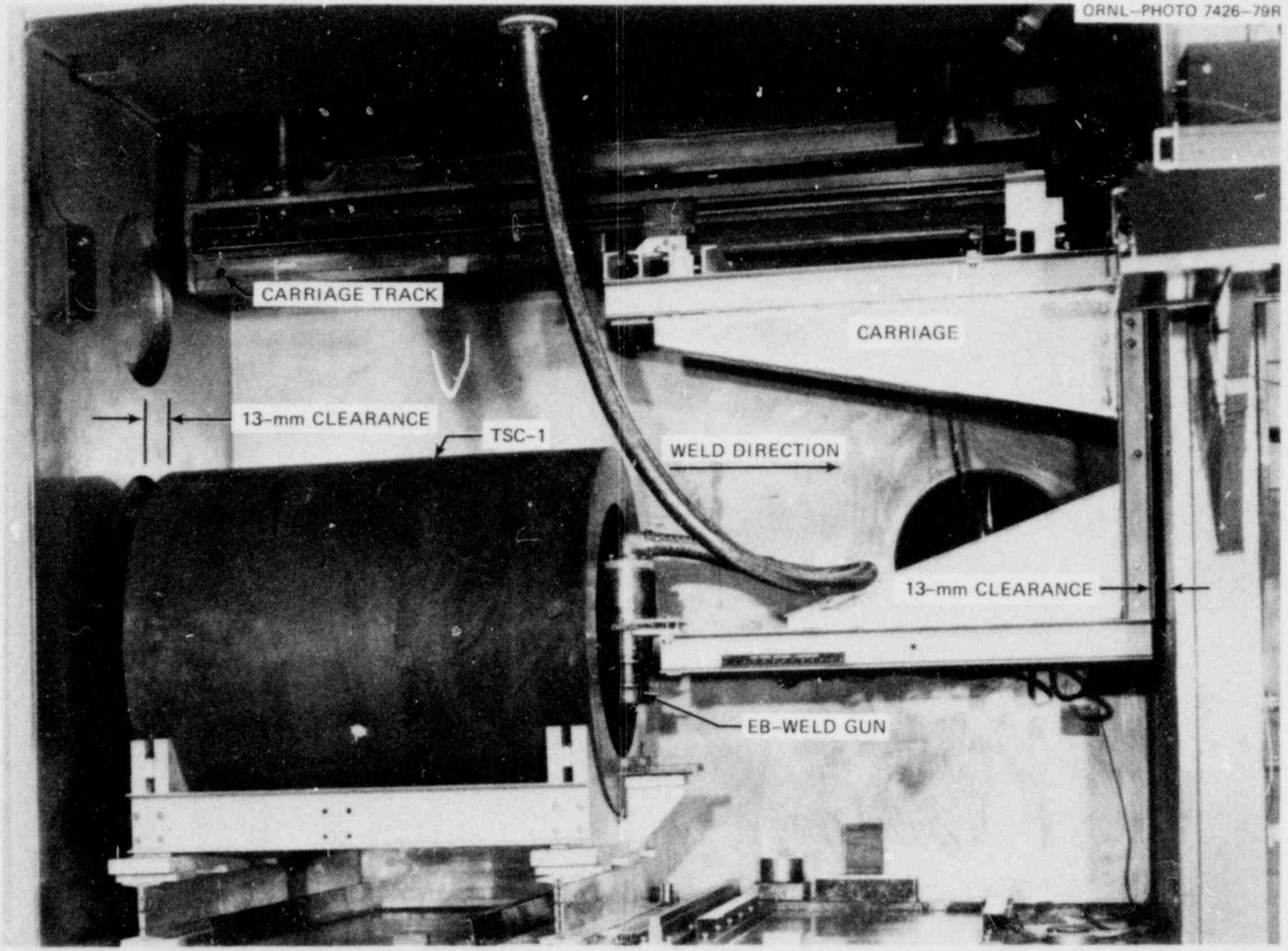

Fig. 6.1. View of interior of EB-weld box in TSC-1.

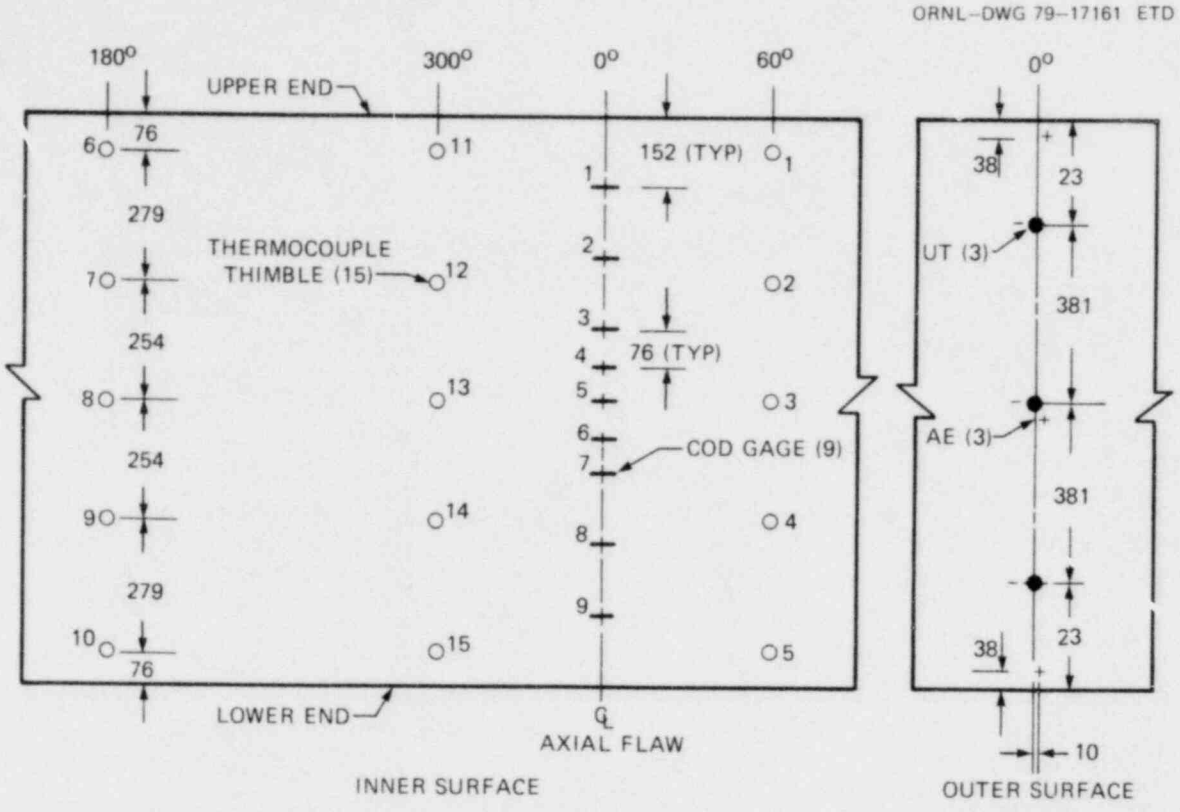

Fig. 6.2. Partially developed views of TSC-1 showing locations of instrumentation.

rate. The gages were placed across the initial long axial flaw, as shown in Fig. 6.2. Details pertaining to mounting and performance of the gages are discussed in Ref. 3. Figures 6.3 and 6.4 are photographs of the gages on the inner surface of TSC-1 following TSE-5. The buckled condition of the gages shown in these figures is the result of extensive plastic strain of the gages during the thermal shock, followed by closing of the crack as the thermal stress subsided. A good indication of maximum crack opening during the thermal shock can be obtained by measuring the permanent stretch of the gages.

All gages but Nos. 4 and 6 (Fig. 6.2) were recorded on the data system (digital) and on charts (analog). Output from the other two gages was fed into a fast-phenomena digital recorder, permitting a determination of crack-opening rate.

6.3.3 Acoustic emission

Three acoustic emission transducers were located on the outer surface of TSC-1 opposite the long axial flaw in the specific locations shown in Fig. 6.2. These locations were selected so that only events in the immediate flaw zone were recorded.

6.3.4 Ultrasonics

Three ultrasonic test (UT) crystals were located on the outer surface of TSC-1 directly opposite the long axial flaw (see Fig. 6.2). This instrumentation was used to determine crack depth before, during, and after the thermal shock. All output was recorded on tape.

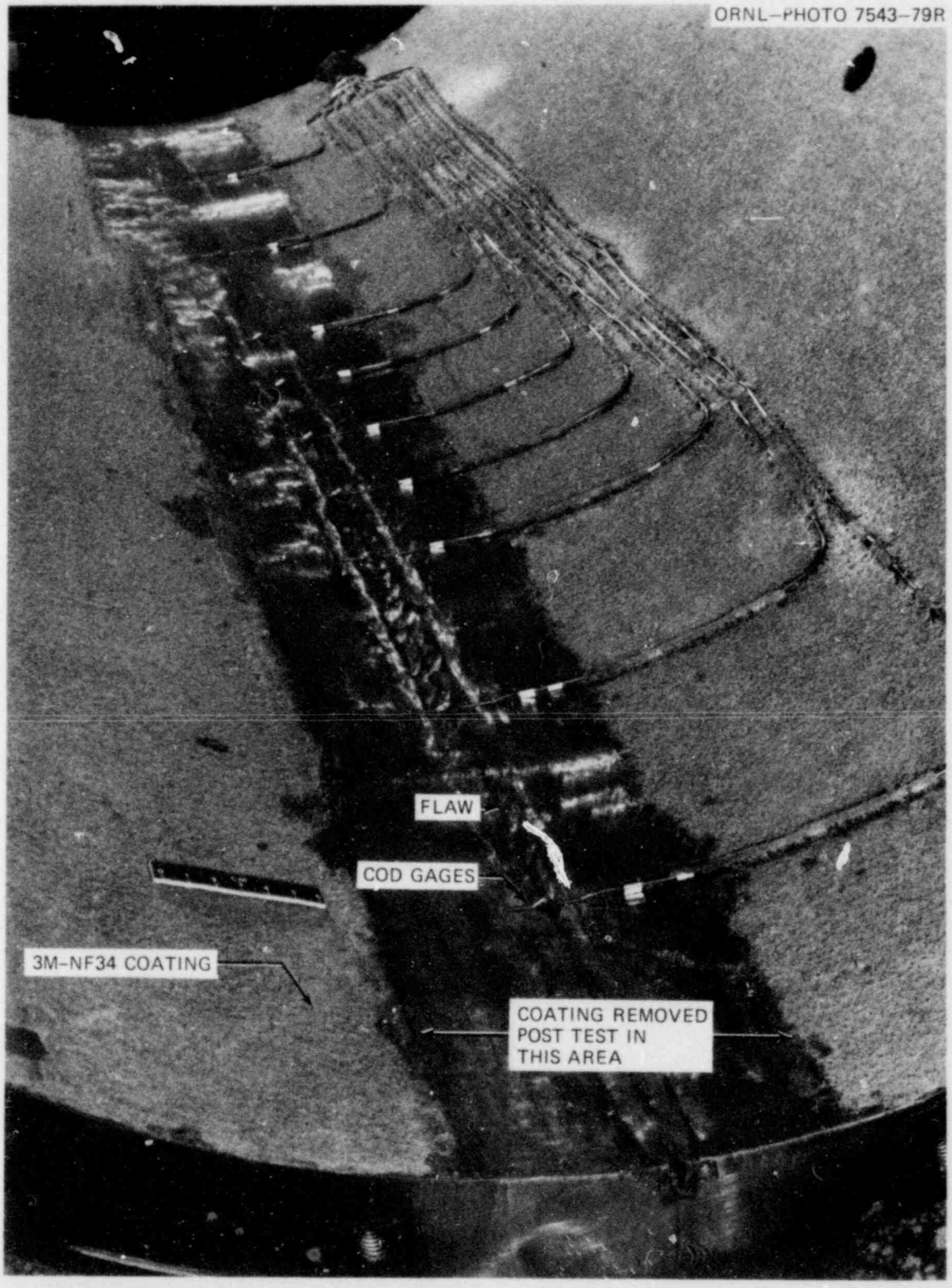

Fig. 6.3. View of interior of TSC-1 following TSE-5 showing the long axial flaw and COD gages.

Fig. 6.4. Close-up view of flaw and COD gages in TSC-1 following TSE-5.

6.4 Coating of TSC-1 Inner Surface

The inner surface of TSC-1 was coated with rubber cement (3M-NF34) to enhance the heat transfer to liquid nitrogen (see Figs 6.3 and 6.4). Prior to TSE-5, two thermal shock heat transfer experiments[4] were conducted with TSC-1. From these experiments and the TSE-5 design analysis, the determination was made that the thickness of the rubber cement coating for TSE-5 should be ~0.86 mm. The coating for TSE-5 was applied in 11 separate coats for a total thickness of 0.87 mm.

The coating thickness measurements are made with an eddy current device (Kaman) and include a bias associated with compression of the coating under the applied force of the eddy current transducer. As a check on consistency from one coating to another, the surface density of the coating was also obtained. This was done by weighing 51- by 51-mm squares of vellum that were attached to the inner surface of the test specimen and coated along with the rest of the surface (these were also used for the thickness measurements). The desired surface density for TSE-5 was 0.39 mg/mm^2, and the value obtained was 0.37 mg/mm^2, which was considered satisfactory.

Following the two heat transfer experiments, we noticed that the rubber cement coating was blistered and, after warming to room temperature, would flake off easily in many places. However, careful observation following the second heat transfer experiment indicated that the blistering was occurring some time after the test specimen was removed from the LN_2 dunk tank and thus would have no effect on quenching of the test specimen. This was confirmed by the wall temperature measurements, which showed no irregularities in quenching that could be attributed to blistering. Even so, any tendency for blistering could not be tolerated because of the possible consequences during a thermal shock experiment; thus, an investigation was undertaken.

One important observation regarding blistering was that the coating on the ends of the thermocouple thimbles never blistered; in fact, the adhesion to the thimbles was very good. Elsewhere, the coating could be scraped off rather easily posttest. In all previous experiments associated with development of the coating technique and with smaller-scale thermal-hydraulic experiments, including those with the 533-mm-ODA50' class 5 flow-test specimen (TSV-F), adhesion of the coating was very good, even after repeated thermal shocking. Thus, two possible causes of blistering were apparent: (1) there was something peculiar about the surface of TSC-1, or (2) there was something different about the 3M-NF34 material. A test of coating material and cleaning procedure was conducted on a piece of 250-mm pipe that had been used in the LN_2-quench development experiments. The same container of 3M-NF34 used for the two heat transfer experiments with TSC-1 was used for coating the section of pipe, and the surface preparation and coating techniques were the same. The coated pipe was then heated to 93° C and quenched in LN_2. No blistering or other indications of poor adhesion occurred.

The 3M-NF34 adhesive is manufactured at several different 3M facilities, and, according to 3M, processes and component materials at each plant might be slightly different. The adhesive used for the TSC-1 heat transfer experiments came from a different plant than the adhesive used for the earlier experiments, in which no blistering occurred. The 3M company recommended that we purchase the 3M-NF34 adhesive to be used for TSE-5 from the plant that provided our original material. This we did, although, as indicated above, there were indications that the problem was not associated with the material.

During our discussions with 3M, the suggestion was made that condensation caused by air temperature changes and/or surface temperature changes resulting from evaporation of the 3M-NF34 solvent might create a problem. Therefore, while coating TSC-1 in preparation for the second heat

transfer experiment, TSC-1 was maintained at a temperature about 6 K above room temperature; however, blistering still occurred.

Following the TSC-1 heat transfer experiments and prior to TSE-5, TSC-1 was tempered at 633° C for 4 h and cooled in air. This resulted in an oxide scale that was subsequently removed by sanding. The surface was then cleaned with solvent in the usual manner in preparation for application of the coating. With the exception of the heat treatment, this cleaning process, including the sanding, was essentially identical to that used in preparing TSC-1 for the second heat transfer experiment.

As in the previous experiments with TSC-1, there were no indications, based on temperature data, that blistering or other nonbonds had occurred during TSE-5. However, though less extensive than before, blistering did occur, although it was visually obvious only quite some time after TSC-1 had been removed from the LN_2 dunk tank. Thus, blistering was not a factor during TSE-5.

A final suggestion from 3M was that we should use 3M-34 instead of 3M-NF34 the next time.

6.5 TSE-5

Thermal shock experiment TSE-5 was conducted on August 1, 1979, and consisted of quenching the inner surface of a thick-walled steel cylinder (initially at 96° C and containing a long axial flaw) with liquid nitrogen. Conditions for the experiment are summarized in Table 6.1.

Anticipated results of TSE-5, based on expected heat transfer conditions and specified and assumed material properties, are discussed in Ref. 5 and are summarized in terms of the critical-crack-depth set of curves in Fig. 6.5, which indicates that the 16-mm-deep initial flaw would initiate at a time of 204 s and that a total of three initiation-arrest events would take place prior to warm prestressing (WPS). Depending on the actual values of K_{Ia}/K_{Ia} (the K_{Ia} vs temperature curve was assumed) and assuming WPS to be effective, the final crack depth would be ~50 to 70% of the wall thickness, and

Table 6.1. Test conditions for TSE-5

Test specimen	TSC-1
Test specimen dimensions, m	
OD	0.991
ID	0.686
Length	1.22
Test specimen material	A508 class 2
Test specimen heat treatment	Tempered at 613° C for 4 h
K_{Ic} vs temperature curve specified	HSST plate 02 (Ref. 6)
K_{Ic} and K_{Ia} curves used in TSE-5 design analyses	ASME Section XI, Appendix A,[7,8] $RT_{NDT} = -34°C$
Flaw	Long axial sharp crack, a = 16 mm
Temperatures, °C	
Wall (initial)	96
Sink	−196
Coolant	LN_2
Flow rate	Natural convection loop
Coating on quenched surface	Rubber cement (3M-NF34)
Coating thickness, mm	0.8

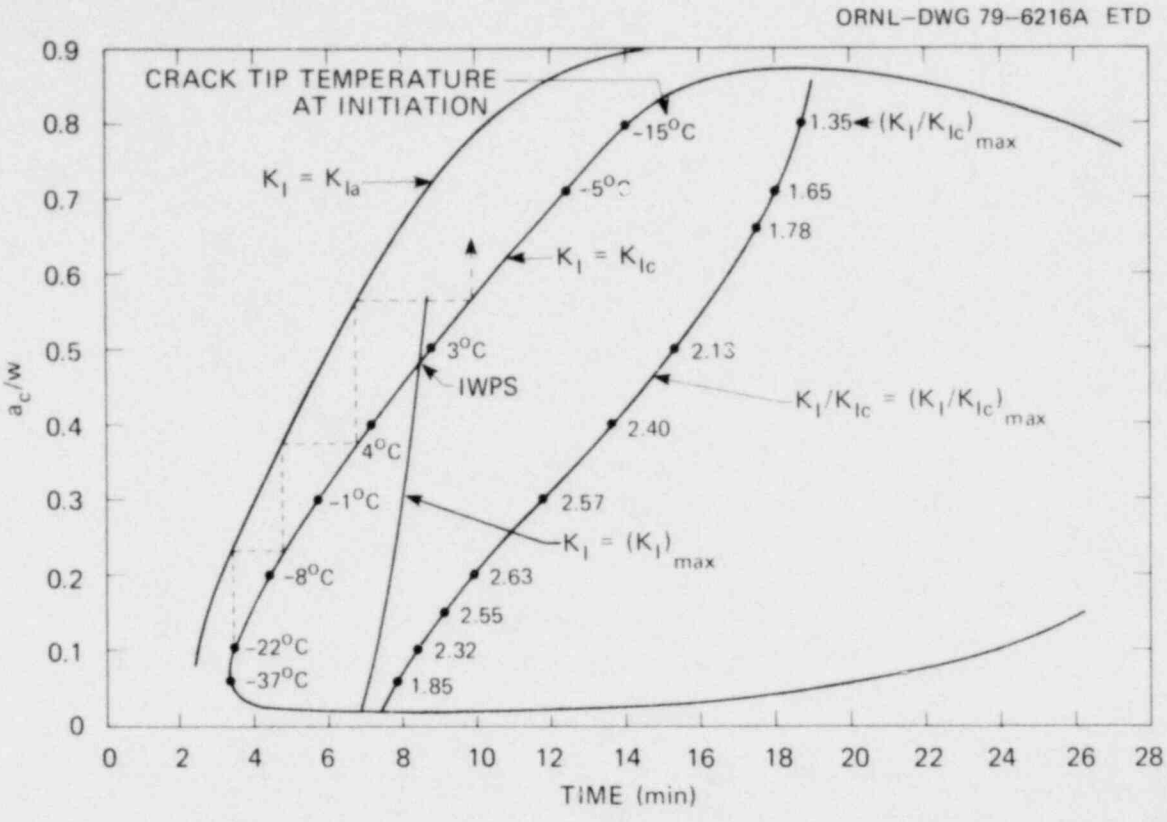

Fig. 6.5. Critical-crack-depth curve from pretest analysis of TSE-5.

incipient warm prestressing (IWPS) would take place ~50% of the way through the wall. The largest single crack jump was expected to be ~20% of the wall thickness. Calculated maximum K ratios $[(K_I/K_{Ic})_{max}]$ were large enough to ensure initiation of the initial flaw and to provide assurance that WPS was effective, if initiation failed to occur after the time corresponding to IWPS.

Actual results of the experiment indicate that (1) the thermal shock was somewhat more severe than planned, (2) the toughness of the material above a temperature of 0° C was substantially less than expected (see Sect. 6.7), and (3) even though WPS may have been effective in preventing crack initiation deep in the wall, conclusive evidence could not be obtained.

As illustrated graphically in Fig. 6.6 by the trace of the COD gage output, initiation-arrest events took place at 105, 177, and 205 s, with all gages indicating these events. Four of the gages survived the event at 205 s and indicated no further events during the remainder of the 30-min test. Prior to the event at 105 s, a few relatively small events took place but were not indicated by all gages.

Flaw depths corresponding to the three major events were measured with UT instrumentation before, during, and after the experiment, and this information is presented in Fig. 6.7. As indicated by these results, less propagation of the flaw occurred near the ends of TSC-1 than elsewhere. Maximum uniform fractional crack depths for the three events, as determined by UT, are 0.20, 0.63, and 0.80.

Posttest fracture mechanics calculations have been made using the actual TSE-5 radial temperature distributions as input to the LEFM finite-element (FE) code. For the first such analysis, the K_{Ic} vs temperature data (referred to in Table 6.1) were used,[6] and the corresponding critical-crack-depth set of curves is shown in Fig. 6.8, with the actual path of events indicated by the dashed lines. The

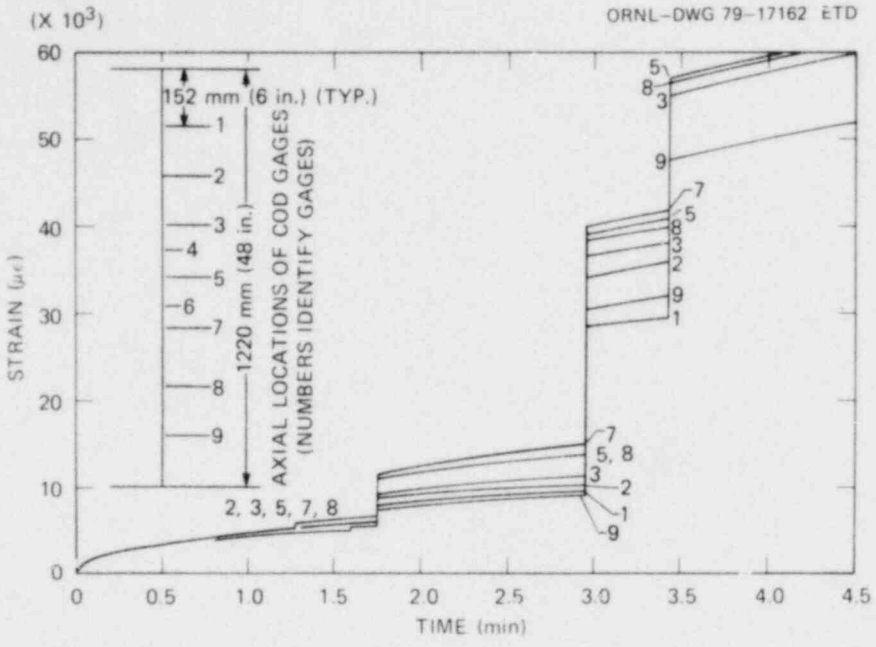

Fig. 6.6. COD output during TSE-5.

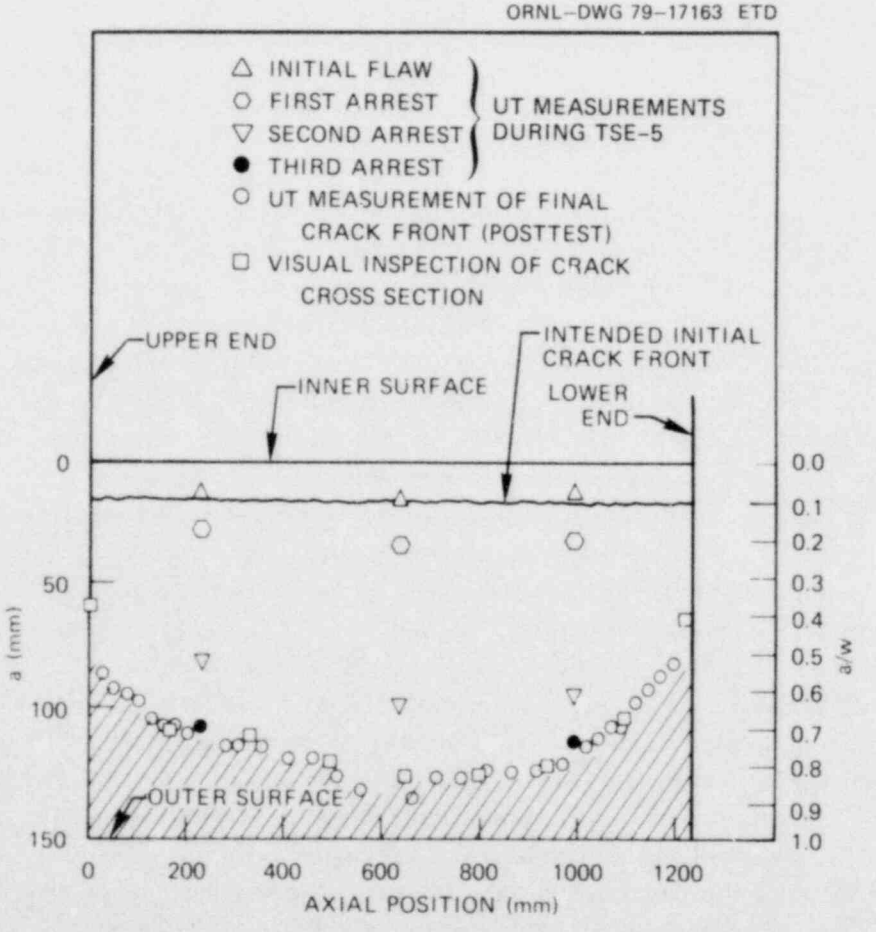

Fig. 6.7. Measurements of crack depth during and after TSE-5.

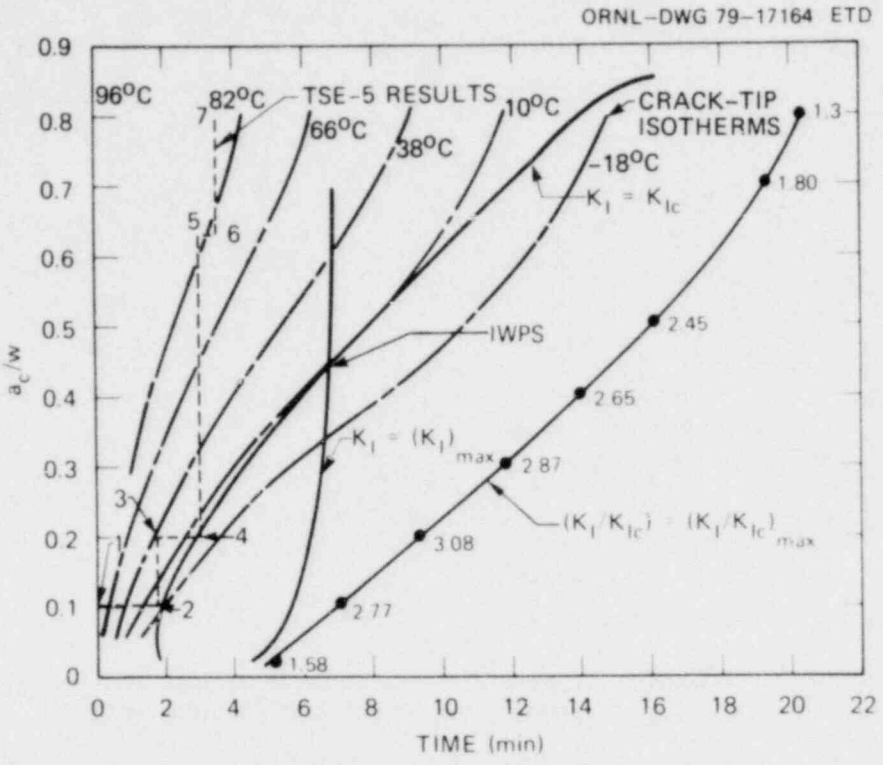

Fig. 6.8. Critical-crack-depth curve from posttest analysis of TSE-5 (original K_{Ic} data).

first two initiation events (points 2 and 4 on the dashed curve) agree well with the $K_I = K_{Ic}$ curve, but the final initiation event (point 6) does not, indicating that the actual toughness at temperatures corresponding to the third initiation event was much less than assumed.

As mentioned in Sect. 6.7, a posttest review of the K_{Ic} data obtained for the TSC-1 prolongation to TSE-5 indicates that the toughness of TSC-1 for temperatures above 0° C is considerably less than it was believed to be prior to TSE-5. This trend is also indicated by a comparison of the calculated K_I values corresponding to the TSE-5 initiation and arrest events with the available pretest K_{Ic} data and the specified K_{Ic} vs temperature curve; such a comparison is shown in Fig. 6.9. With the exception of the K_I value for the second initiation event, all the critical K_I values (K_{Ic} and K_{Ia}) derived from TSE-5 indicate a higher transition temperature. Consistent with these data, a new toughness curve was obtained by plotting a straight line through the K_{Ic} values for the first and third initiation events, and this new K_{Ic} vs temperature curve was used in a second posttest fracture mechanics analysis. The results are shown in Fig. 6.10.

Figure 6.10 indicates that the second initiation event (point 4) was delayed relative to what would be expected on the basis of this particular analysis, and this delay, which results in a further increase in K_I, would account for the large second crack jump. What caused the delay is not clear, although it might be crack-tip blunting, inhomogeneities, or simply statistical variations in K_{Ic}. There are arguments against each of these, but a long crack jump did take place. Regarding the possibility of a statistical variation, note that the K_{Ic} value corresponding to the second initiation event is ~38% higher than the toughness curve (Fig. 6.9) used in the analysis.

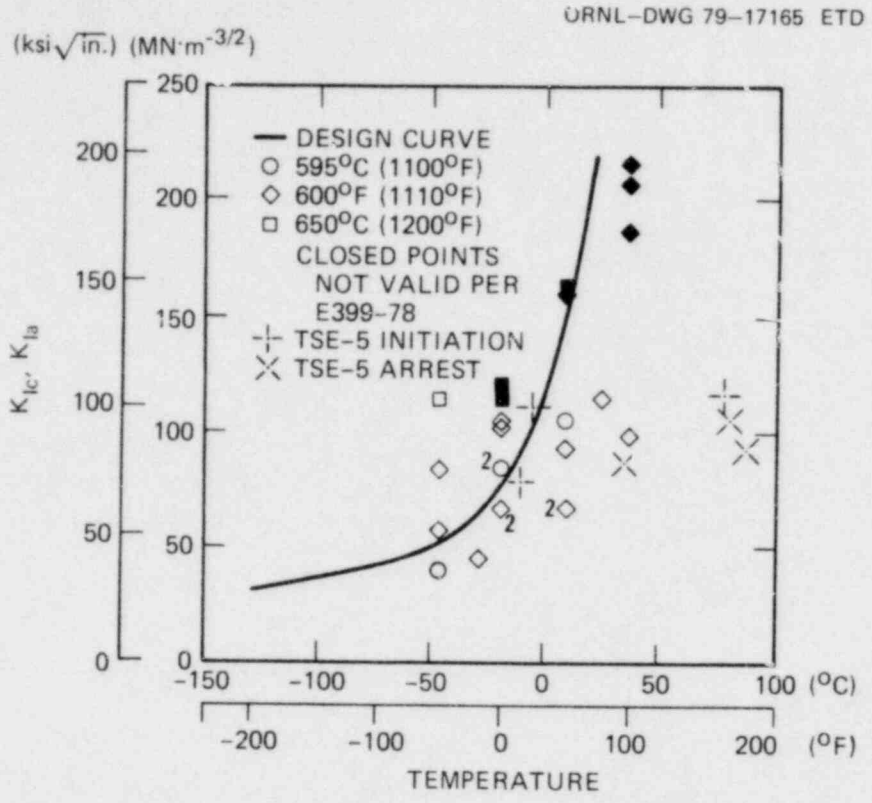

Fig. 6.9. K_{Ic} vs temperature data obtained from the TSC-1 prolongation (pretest) and from TSE-5.

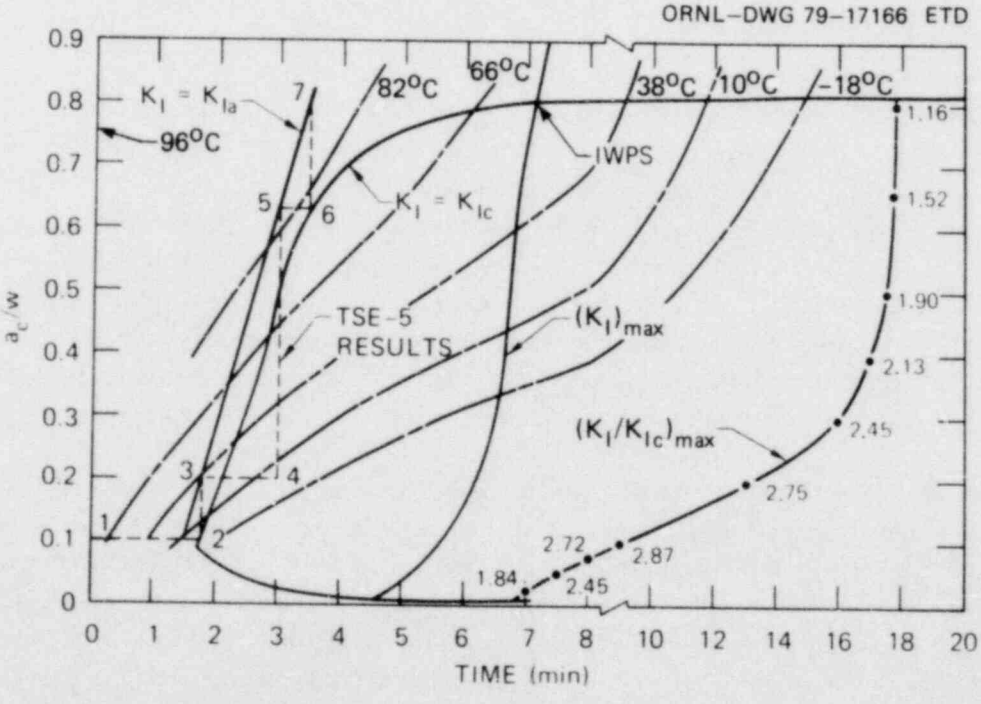

Fig. 6.10. Critical-crack-depth curve from posttest analysis of TSE-5 using TSE-5 K_{Ic} data.

Figures 6.8 and 6.10 also give an indication of the crack depth corresponding to IWPS. As indicated, this crack depth is a function of the toughness curve used in the analysis. If the actual toughness curve were identical to that specified, the fractional crack depth corresponding to IWPS would have been ~0.45 (Fig. 6.8). However, the use of the apparent lower toughness in the second posttest analysis resulted in an IWPS fractional crack depth of ~0.8 (Fig. 6.10). The calculated maximum K ratio $[(K_I/K_{Ic})_{max}]$ for this crack depth is only 1.16, and no initiation events took place for cracks deeper than ~0.63. Thus, WPS apparently prevented a fourth initiation event. However, the maximum K ratio (~1.16) for the final crack depth (~0.80) is too small to compensate for uncertainties in K_I and K_{Ic}, and, therefore, a firm conclusion regarding a demonstration of WPS during TSE-5 cannot be drawn.

Another objective of TSE-5 was to demonstrate crack arrest in a rising K_I field. The pretest analysis indicated that this could be achieved for the first two crack jumps. However, results of the posttest analysis, as shown in Fig. 6.11 in terms of K_I vs fractional crack depth (a/w), indicate that the first arrest event occurred as K_I reached a maximum $[dK_I/d(a/w) = 0]$ and that the other two occurred as K_I was decreasing with increasing crack depth. During the second crack jump, K_I initially increased

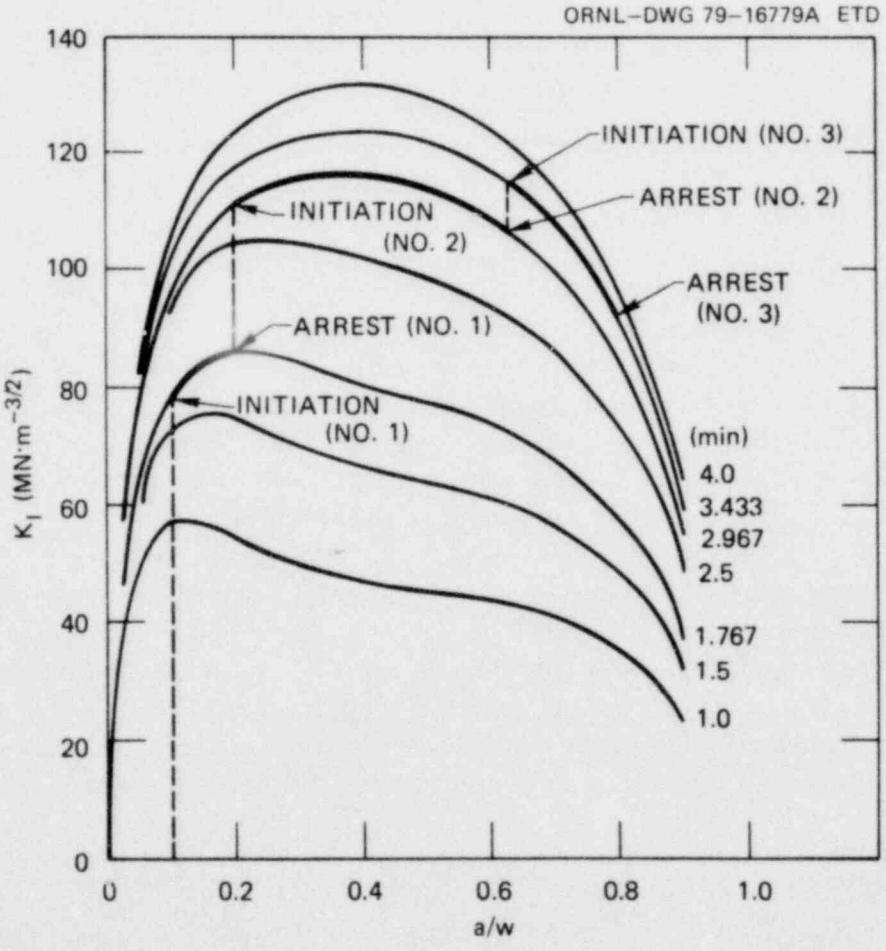

Fig. 6.11. K_I vs a/w for several times in the TSE-5 transient (posttest analysis).

and then decreased before arresting, while, for the third crack jump, K_I was decreasing for the entire crack jump.

Results of the experiment (as related above) are summarized in Table 6.2. Note that the K_{Ic} and K_{Ia} values listed for the three initiation-arrest events are based on posttest K_I calculations and are completely independent of assumptions regarding toughness curves used in the analysis. The toughness values listed in Table 6.2 are material properties derived from the experiment (TSE-5). Additional K_I values calculated posttest for TSE-5 are shown in Fig. 6.12, where K_I is plotted as a function of time, with crack depth as a parameter.

Table 6.2. Results of TSE-5

	Initiation-arrest events		
	1	2	3
Time, s	105	177	205
Crack depth,[a] a/w			
Initiation	0.10	0.20	0.63
Arrest	0.20	0.63	0.80
Temperature, °C (°F)			
Initiation	−9 (15)	−3 (27)	79 (175)
Arrest	36 (96)	82 (180)	89 (193)
K_{Ic}, MN·m$^{-3/2}$ (ksi$\sqrt{\text{in.}}$)	79 (72)	111 (101)	115 (105)
K_{Ia}, MN·m$^{-3/2}$ (ksi$\sqrt{\text{in.}}$)	86 (78)	104 (95)	92 (84)
Duration of experiment, min	30		

[a]Maximum depth (midlength of TSC-1).

The above K_I values were calculated with a two-dimensional finite-element technique. Previous studies[9] indicate that, for a straight crack front and for the deepest crack investigated (a/w = 0.5), two-dimensional K_I values for the central portion of the cylinder are reasonably accurate. As indicated in Fig. 6.7, the first and second crack fronts are reasonably straight. However, the third and fourth crack fronts are significantly shallower near the ends of the test cylinder, and, thus, actual K_I values in the central portion will tend to be less than those calculated. A three-dimensional analysis considering the actual TSE-5 crack fronts has not been conducted.

The fracture surfaces of the long axial flaw are being examined at this time. To gain access to these surfaces, TSC-1 was cut into two nearly equal-length cylinders, and then a narrow pie section containing the flaw was cut from each of the two cylinders. These pie sections were then cut into eight nearly equal-length blocks. (The cutting plan is shown in Fig. 6.13.) Each block will be broken open at cryogenic temperatures to reveal the fracture surfaces; to facilitate the operation, an axial slot 5 mm wide by 8 mm deep (3/16 by 5/16 in.) was machined in the top end of the EB weld to allow insertion of a wedge.

The ends of each of the eight blocks have been polished for examination of the crack cross sections. A cross section for one of the blocks (TSC1-1) is shown in Fig. 6.14. Each of these blocks has been superficially examined for an estimate of initial and final crack depth. These findings are recorded in Fig. 6.7, and these results are seen to agree well with the UT measurements. One of the blocks (TSC1-1)

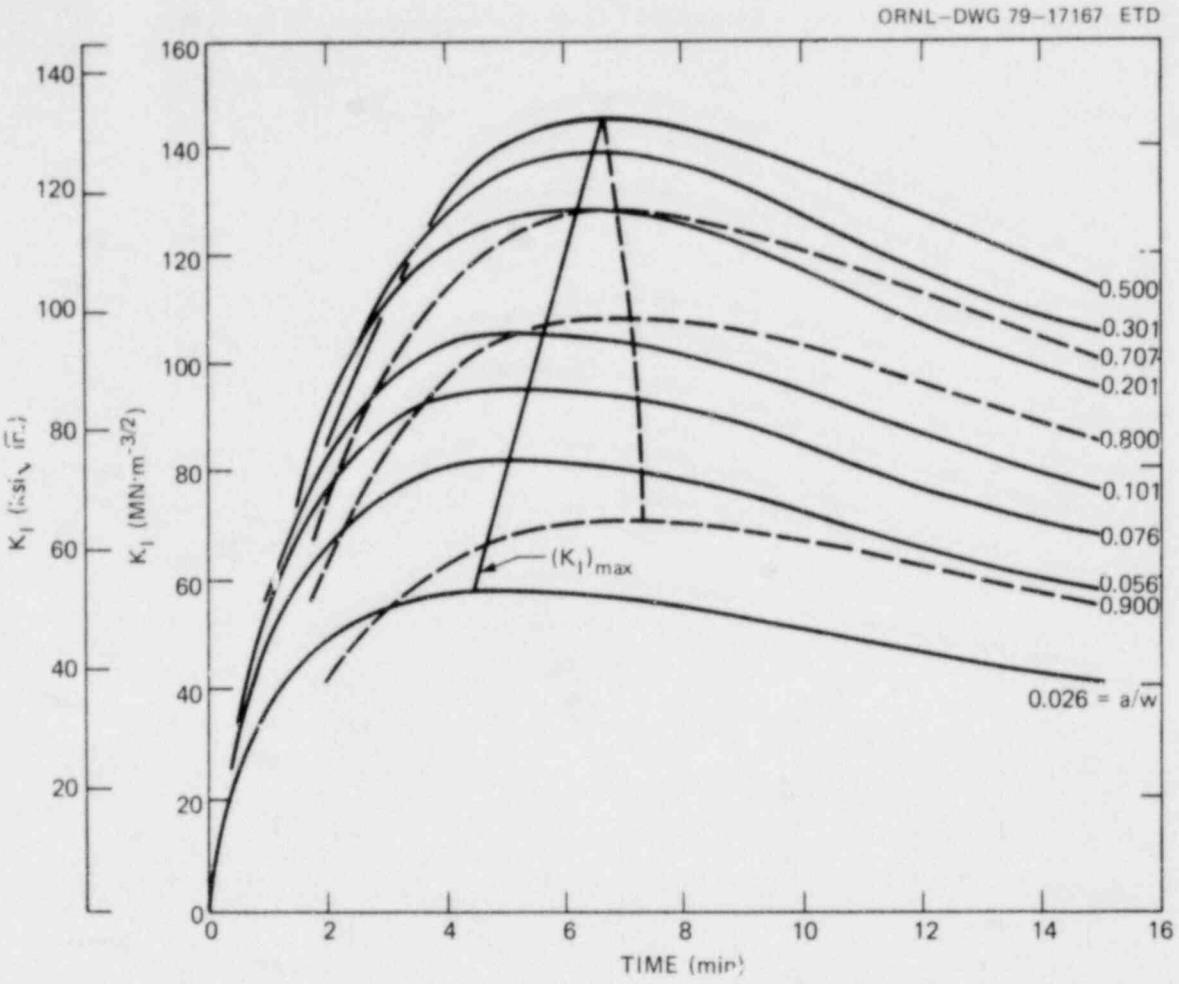

Fig. 6.12. K_I vs time for several crack depths (TSE-5 posttest analysis).

has been broken open, and the fracture surface is shown in Fig. 6.15. The initial and second flaw depths are quite obvious, but the others are not. As indicated in Fig. 6.15, the EB-weld and next fracture surfaces are quite flat and well defined, and the depths agree well with the UT measurements. The fracture induced by the wedge at −196° C (−320° F) appears flat, but its initiation point is not well defined. All the area in between is quite rough and irregular, without a clear indication of the second arrest event. A thorough examination of this and similar surfaces is being conducted.

An attempt was made during TSE-5 to measure crack velocity by recording the output of COD gages on a scope. This output (COD vs time) could then be converted to crack velocity by relating crack depth to COD with the LEFM-FE analysis. Comparing measured and calculated COD for the same crack depth at specific times in the transient indicates that the calculation overestimates COD for TSE-5 by about 50%. Thus, the crack velocities deduced from the COD vs time data would tend to be low by this amount.

The second crack jump was recorded successfully on a scope, and a reprint of the curves for COD gages 4 and 6 (Fig. 6.2) near midlength of TSC-1 is shown in Fig. 6.16. We observed from the decreasing slopes of the curves with time that the velocity decreases throughout the crack jump. The uncorrected

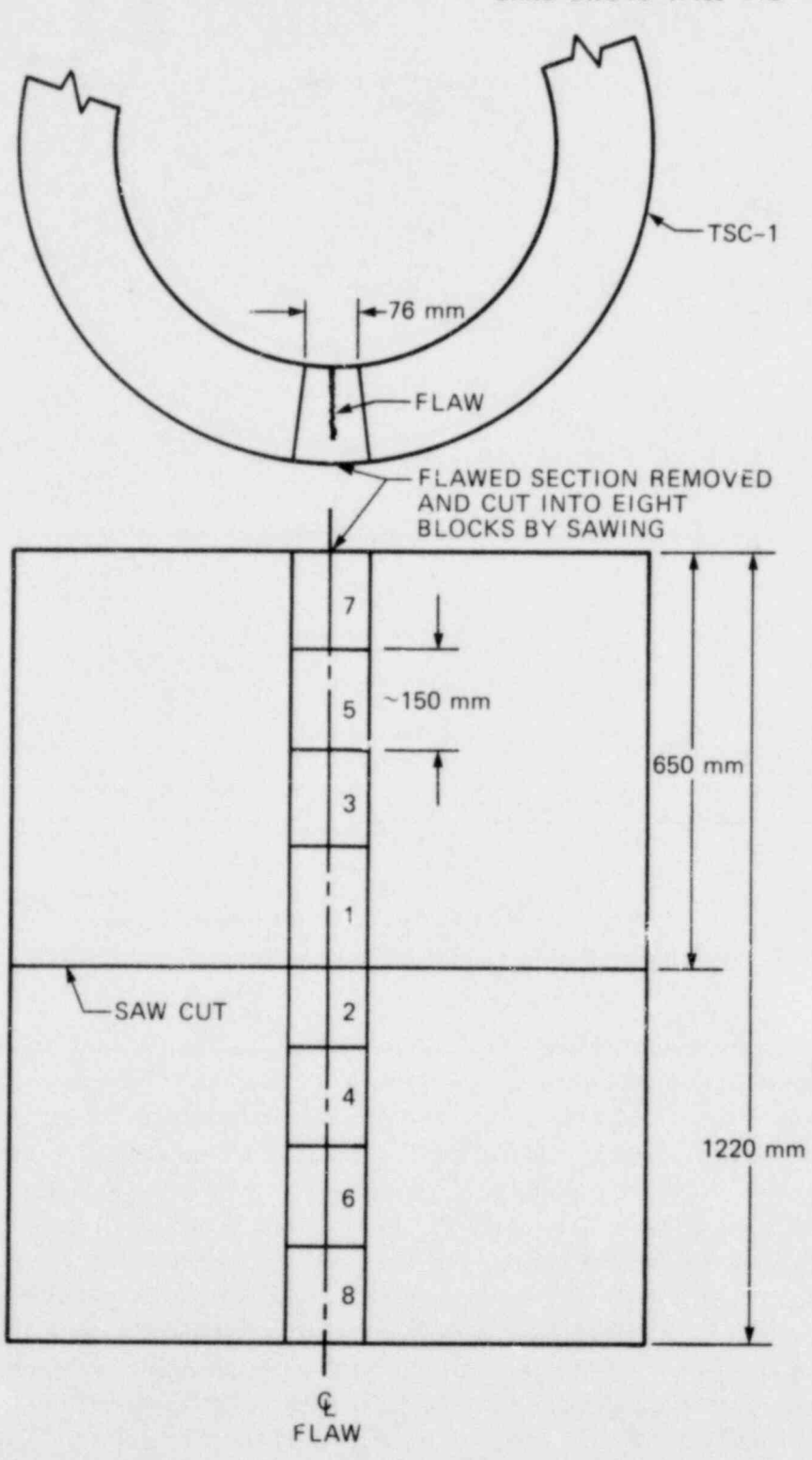

Fig. 6.13. Section of TSC-1 removed for study of crack profile and fracture surfaces.

M&C PHOTO Y164626

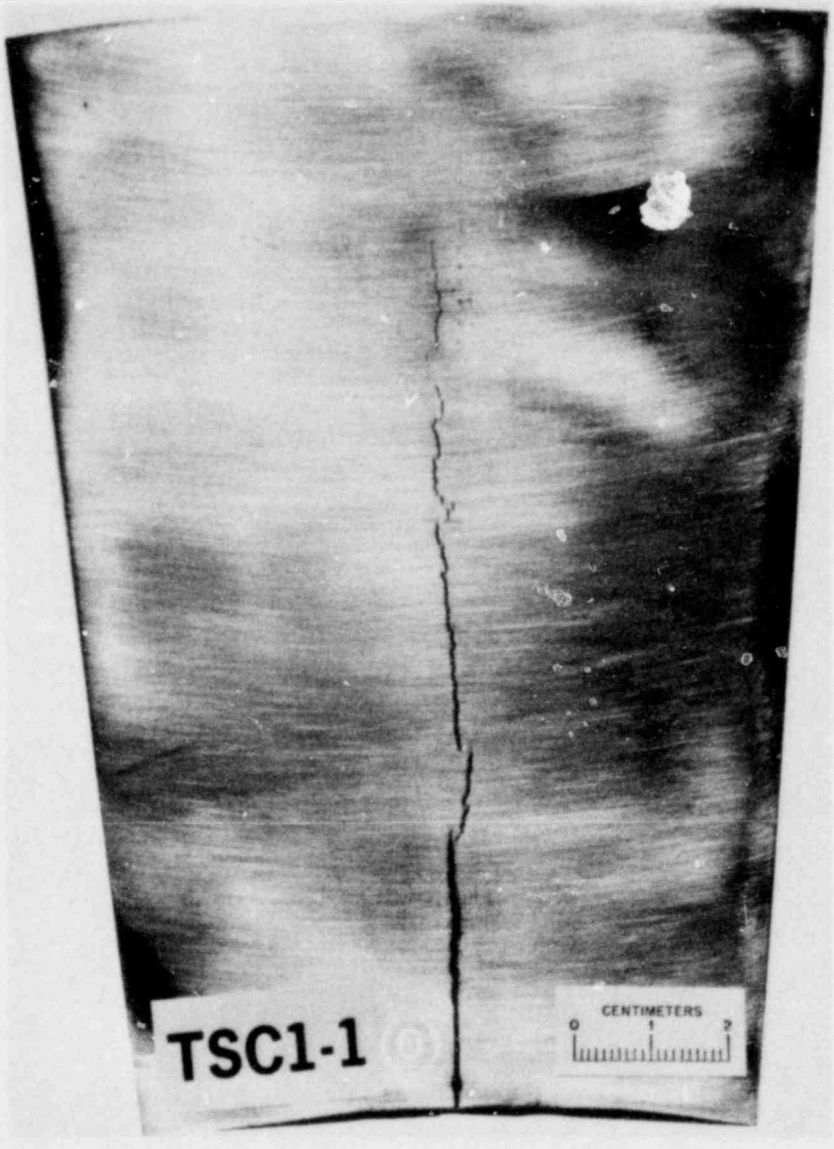

Fig. 6.14. Cross section of TSE-5 long axial flaw (posttest).

calculated crack velocity for the first part of the jump is ~180 m/s, which is rather low compared with velocities measured on laboratory-size crack-arrest specimens.

This relatively low velocity and the disagreement between measured and calculated COD raise questions regarding the accuracy of the COD measurements. A check on maximum COD was obtained posttest by determining the permanent stretch of the COD gages. Most of the strain in the COD gages during TSE-5 was beyond the elastic limit. As the thermal stress diminished, the crack closed, causing the unbonded portion of the COD gages to buckle without inducing significant reduction in actual length of the gage (see Fig. 6.4). Thus, the stretched length could be determined, and the results agree well with the output of the COD gages.

ORNL–PHOTO 0057–80

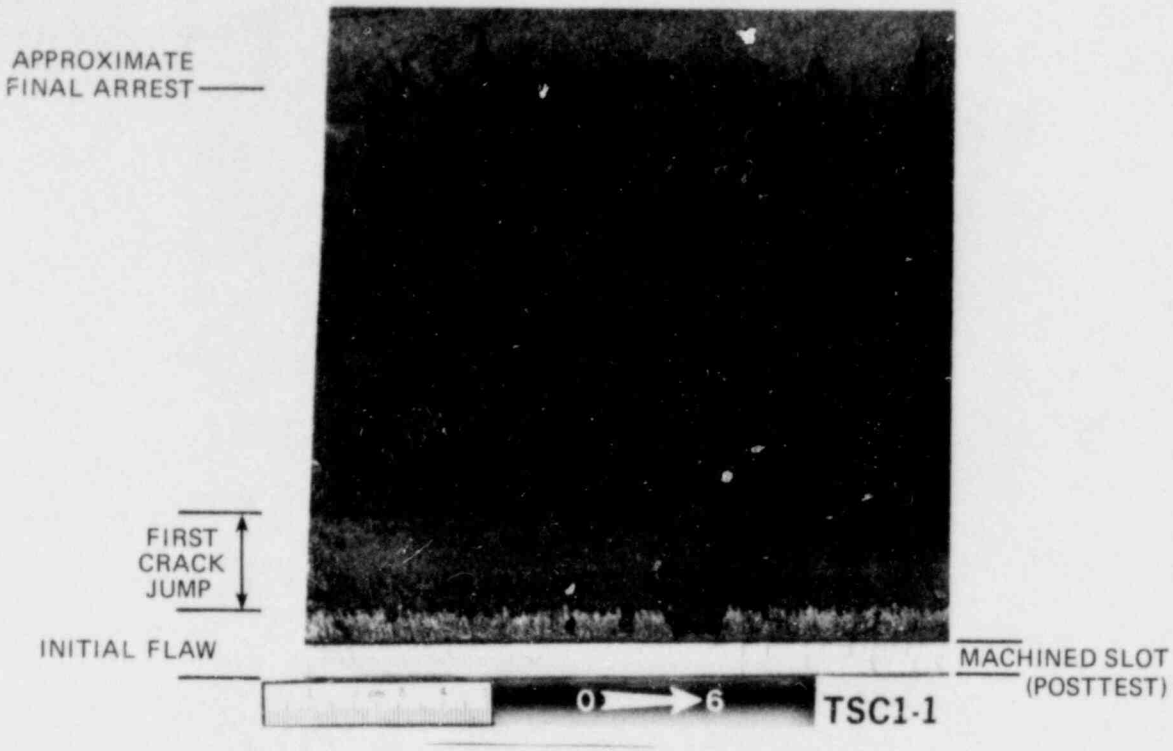

Fig. 6.15. Fracture surface of TSE-5 long axial flaw (posttest).

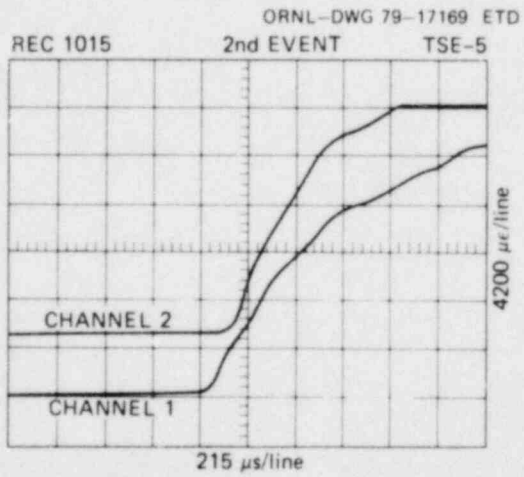

Fig. 6.16. COD (4 and 6) output vs time for second crack jump during TSE-5.

Another event or series of events taking place during TSE-5 may have had an influence on the behavior of the long axial flaw. Following TSE-5 and after the rubber cement coating had been removed from the inner surface of TSC-1, an extensive cracking pattern other than the long axial flaw was discovered on the inner surface. A sketch of the inner surface showing some of the more important features of the cracking pattern is shown in Fig. 6.17. The cracking apparently initiated at a single, small

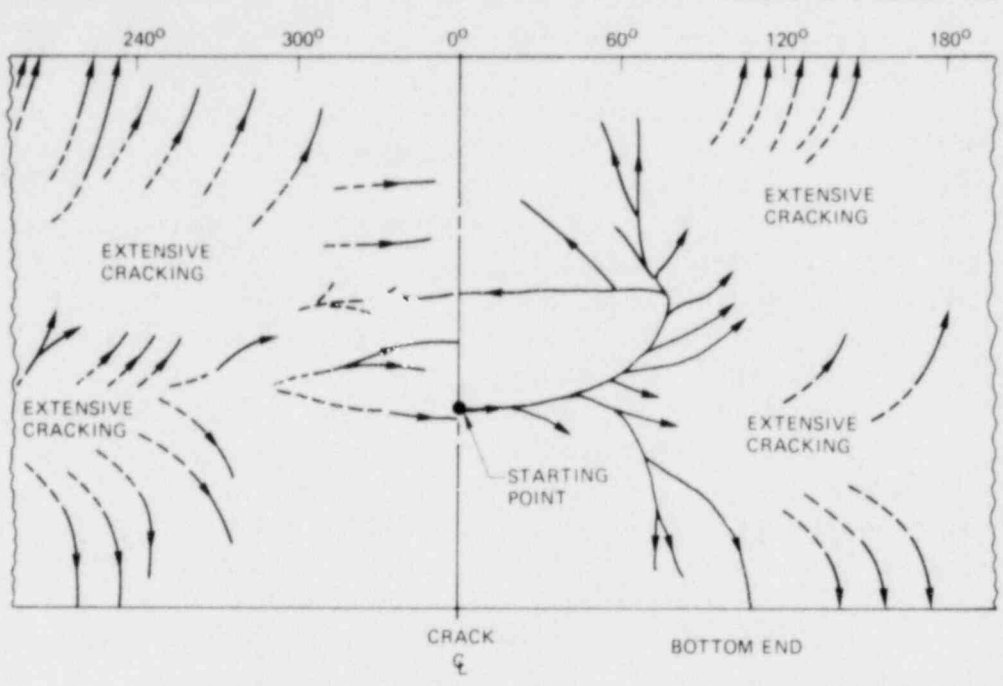

Fig. 6.17. Secondary cracking pattern on inner surface of TSC-1 following TSE-5.

flaw, which existed in the initial axial flaw zone as a cross crack in the EB weld, moved circumferentially, and then branched out over essentially the entire surface. Several branches turned in an axial direction and ran out the ends of the cylinder, while others turned axially and then back to a circumferential direction. Some of the cracking extended a full 360°, returning to the long axial flaw as several circumferential flaws. There is no indication at this time that any of the cracks crossed over the long axial flaw.

TSC-1 was in the process of being cut into numerous pieces for material characterization purposes at the time the secondary cracking was discovered. The resultant cuts have revealed the approximate depth of some of the crack branches. Some of these cracks appear to extend as much as 35% of the way through the wall.

Cross cracking of the EB weld occurred during hydrogen charging of the EB weld and appeared to be very shallow (~1 mm), in which case initiation was not expected. However, the more severe thermal shock increased the chances of very shallow flaws initiating, and, as shown in Fig. 6.10, long flaws with depths as small as ~0.1 mm ($a/w = 0.004$) would initiate. The times of initiation of a cross crack this shallow presumably would be later than the times associated with the long-flaw events. However, if a cross crack were somewhat deeper ($a/w \geq 0.01$), the time of initiation could have been within the time span of the axial-flaw events.

The existence of axial flaws in addition to the intended long axial flaw would tend to reduce the thermal stress relative to that in the absence of the additional flaws and thus would result in lower values of K_I, and COD. Calculated values of COD are somewhat greater than measured, but the calculated K_I values appear reasonable compared with independently determined K_{Ic} and K_{Ia} values (see Sect. 6.7). Another point to consider in this regard is that the areas of very extensive and axial cracking are ~500 mm (20 in.) to either side of the long axial flaw, as shown in Fig. 6.17. Calculations are being made to

determine whether this distance is sufficient to preclude a significant effect of the secondary cracking on the behavior of the long axial flaw.

As mentioned above, the secondary cracking possibly took place after the long flaw experienced one or more of its events. This may be the case because some of the secondary cracking apparently was stopped by the long flaw and none crossed over. However, a more detailed examination of the cracks is required before a firm conclusion can be drawn.

The thermal shock during TSE-5 was more severe than intended, but the axial symmetry in quenching was still very good. The expected and actual surface quench rates are shown in Fig. 6.18, and the degree of axial symmetry is illustrated in Fig. 6.19, which shows near-surface temperatures at five locations along the length of TSC-1 as a function of time. Previous heat transfer experiments[4] with the same equipment indicated that significant asymmetry would result for such a rapid quench. However, just prior to TSE-5, the lower plenum was increased in size by raising the lower stop point for the test cylinder in the LN_2 dunk tank. Apparently, this modification resulted in the more severe quench and in a reduction in asymmetry as a result of an increase in LN_2 flow rate.

Radial temperature distributions were measured during TSE-5 at 15 different locations in the test cylinder (see Fig. 6.2); at each location, 12 radial locations were monitored. Radial temperature distributions for times corresponding to each of the three initiation-arrest events for the long axial flaw are shown in Figs. 6.20 through 6.22. Similar data were recorded at 2-s intervals during the transient and were used in the posttest LEFM-FE analysis for the thermal loadings.

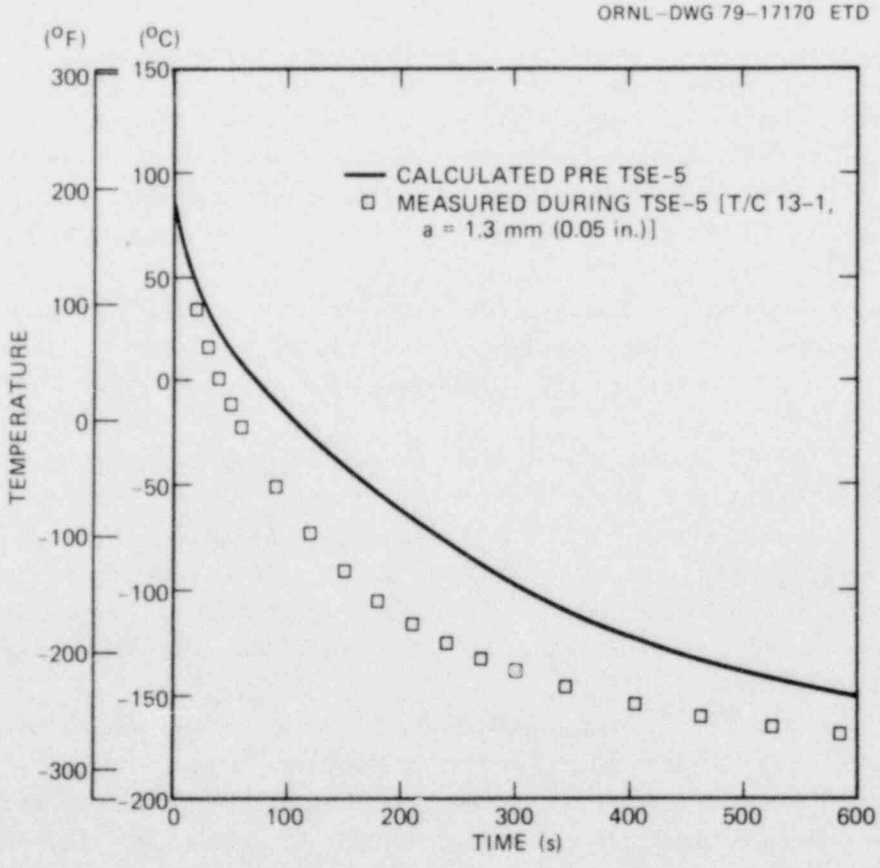

Fig. 6.18. Comparison of calculated (pretest) and measured surface-temperature transient for TSE-5.

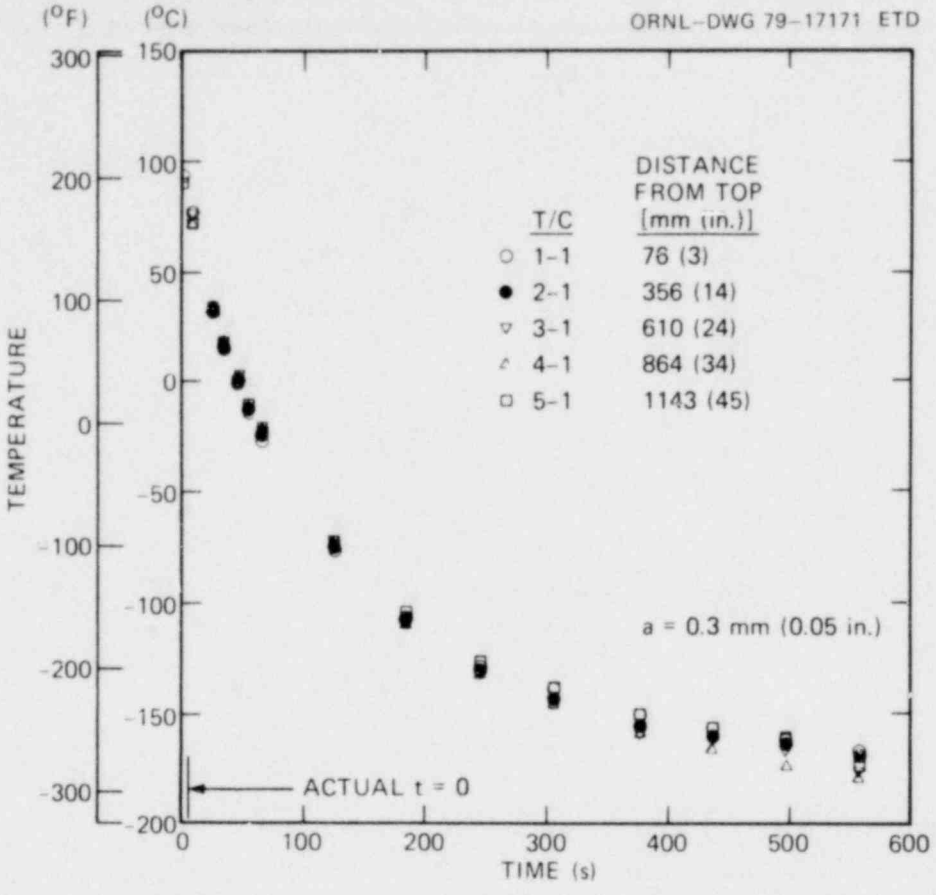

Fig. 6.19. Near-surface temperatures at five elevations in TSC-1 during TSE-5 thermal transient.

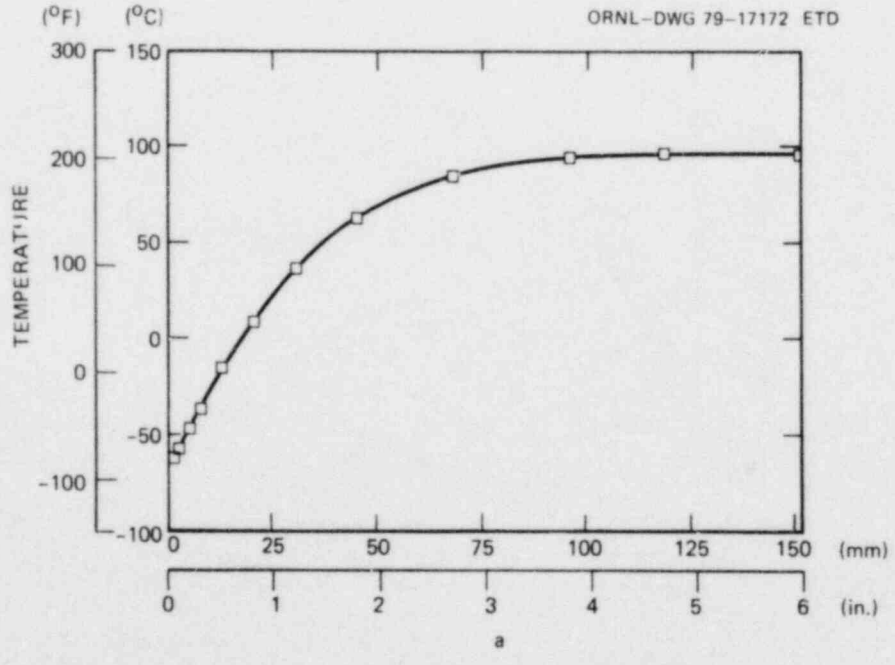

Fig. 6.20. Radial temperature distribution at t = 106 s during TSE-5.

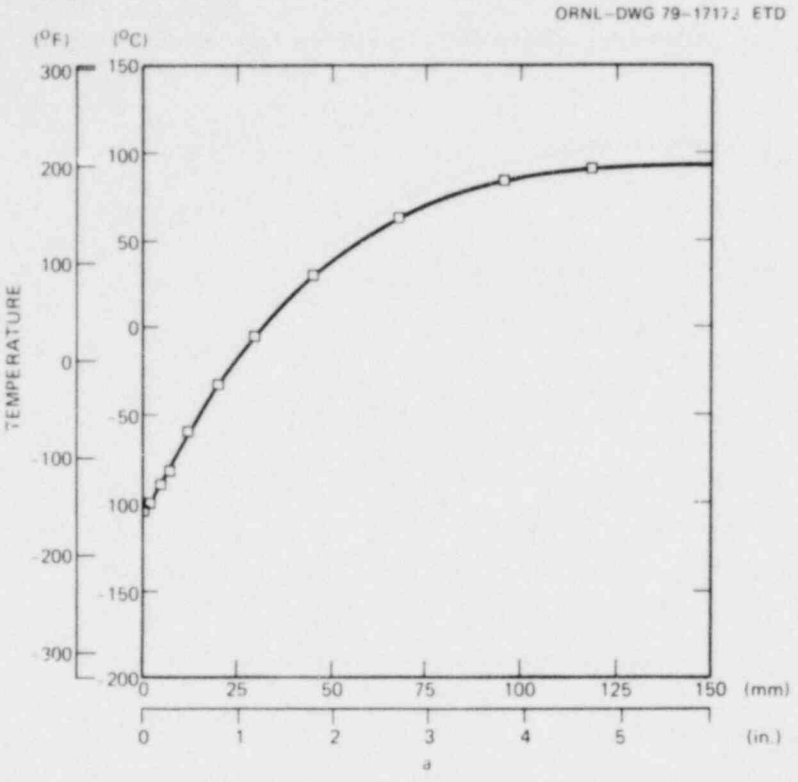

Fig. 6.21. Radial temperature distribution at t = 178 s during TSE-5.

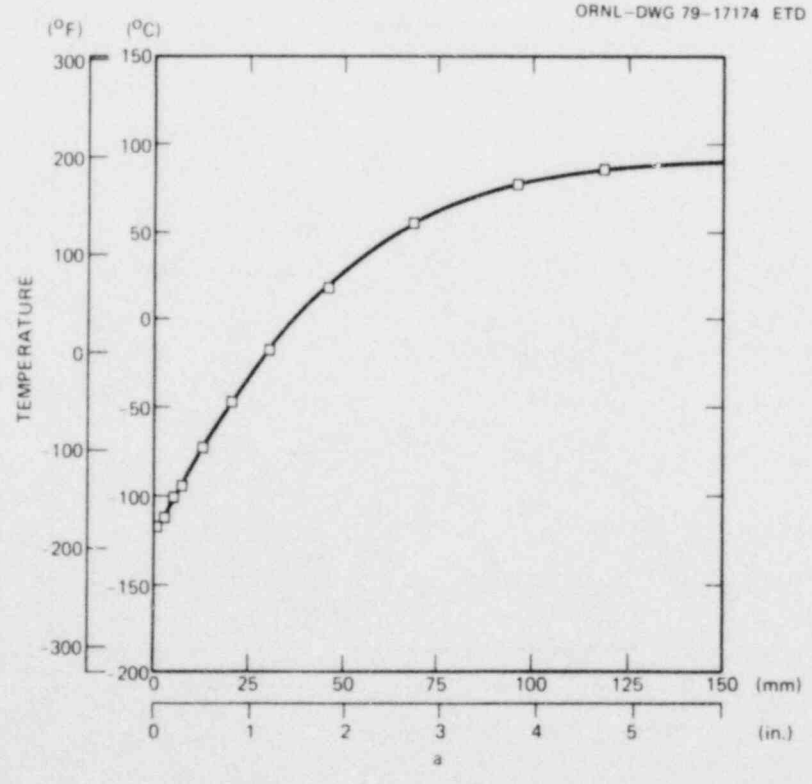

Fig. 6.22. Radial temperature distribution at t = 206 s during TSE-5.

6.6 Residual Stress Studies

The inner and outer surfaces of the rough-machined forging used for TSC-1 and an adjacent narrow annular region experienced very high (nonelastic) tensile strains during the water-quench heat treatment (quenched from 870°C). As a result, high residual stresses remained following the rapid quench to uniform temperature. These stresses (1) were a maximum and compressive at the surfaces, (2) decreased to zero over a short radial distance, and (3) were comparatively low and tensile over the remainder of the wall thickness. This is illustrated in Fig. 6.23 for one of the earlier test specimens (TSV-1).[10] Residual stress studies performed on the prolongations from TSV-1 and -2 showed that the removal of 32 mm (1.25 in.) of material from the inner surface after the quench-only heat treatment would eliminate the residual compressive stress in the inner portion of the wall.

At the time, the TSC-1 forging was subjected to the water-quench heat treatment (May 1975), the ID and OD were 622 and 1070 mm (24.5 and 42.0 in.), respectively, and the prolong was still an integral part of the cylinder forging. Before shipping the cylinder to ORNL, National Forge machined the

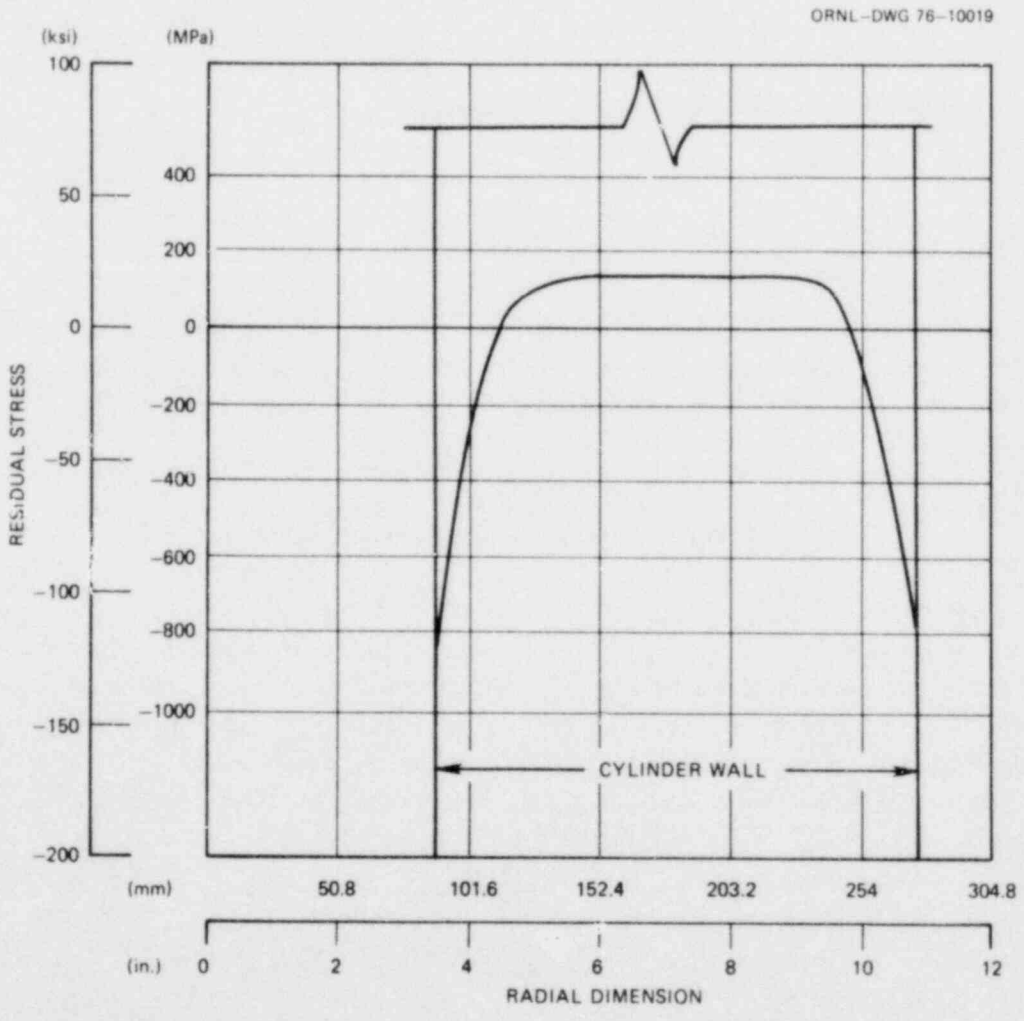

Fig. 6.23. Approximate residual stress distribution in TSV-1 following quench-only heat treatment and prior to final machining.

diameters to 635 and 1041 mm (25.0 and 41.0 in.), leaving a 203-mm (8-in.) wall thickness, and separated the prolong from the test cylinder. Finally, we machined the diameters to 686 and 91 mm (27.0 and 39.0 in.), leaving a 152-mm (6-in.) wall. Thus, 32 mm (1.25 in.) was removed from the inner surface as before, and 38 mm (1.5 in.) was removed from the outer surface. These machining operations should have left the cylinder and prolong essentially stress free.

Subsequently, the cylinder and its prolongation were tempered at 613°C (1135°F) for 4 h and cooled in air. Following this operation, the hole-drilling technique was used to measure residual stresses on the inner and outer surfaces of the TSC-1 prolong without attempting to remove the very shallow residual compressive-stress component caused by machining. The indicated stress on both the inner and outer surfaces was approximately −210,000 kPa (−30,000 psi). Because of the results obtained previously, we believed that most of this residual stress was associated with machining of the surfaces and thus would have little effect on K_I for the initial and deeper flaws.

Following TSE-5, the test cylinder was cut into two cylindrical pieces (as shown in Fig. 6.13), and the lower end was used for residual stress studies. Strain gages were applied to the inner and outer surfaces opposite each other. Small sections of steel with the gages attached were removed by sawing to relieve the residual stresses, except for those induced by machining. The results indicated a residual compressive stress of −120,000 kPa (−18,000 psi) on both the inner and outer surfaces. Thus, the residual stresses induced by machining (and which survived the tempering heat treatment) were apparently about −83,000 kPa (−12,000 psi).

The zone in which the residual stresses were measured (~120° in Fig. 6.17) following TSE-5 had a high density of secondary cracking, and this would seem to have an effect on the determination of pretest residual stresses. However, since the residual stresses are compressive, the secondary cracking would be tightly closed at the time the gages were applied to the surface. Thus, the residual stress would be essentially the same posttest as pretest, and the gages would indicate this.

Since the gradient in residual compressive stress is quite steep, a value of −120,000 kPa (−18,000 psi) on the surface would correspond to a very low tensile stress throughout the major portion of the wall and would have little effect on the calculation of K_I for the initial and deeper flaws.

6.7 Thermal Shock Material Characterization

W. J. Stelzman D. A. Canonico

The results of the thermal shock test TSE-5 indicate that the SA508 class 2 chemical composition steel,* from which the test cylinder was machined, did not recover its fracture toughness in a manner similar to that suggested by the TSE-5 design curve in Fig. 6.24. This behavior is contrary to that previously experienced with SA533 grade B class 1 steel and SA508 class 2 steel; it is contradictory to experience with SA533 grade B steel and SA508 class 2 chemical composition in quenched-only condition.

The selection of a tempering temperature for the thermal shock test cylinder TSC-1 was based on the need to match the design curve shown in Fig. 6.24. The results from 1T compact specimen tests of the prolongation from TSC-1 tempered at 595, 600, and 650°C (1100, 1110, and 1200°F) are shown.

*The steel used in TSC-1 has an ultimate tensile strength in excess of the 725 MPa (105 ksi) limit permitted in the SA508 class 2 specification.

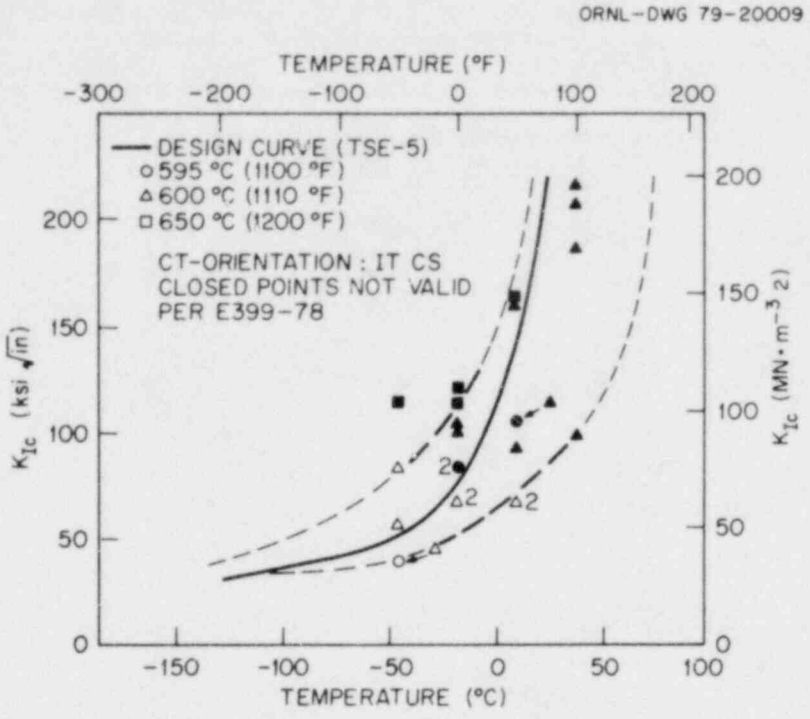

Fig. 6.24. Effect of temperature on static fracture toughness of quenched TSC-1 prolongation after tempering at 595, 600, and 650° C; CT-oriented 1T CS.

The selection of the temper temperature for TSC-1 [615° C (1135° F)] was based on matching the fracture toughness requirement of the solid line at −18° C (0° F). We assumed that the shape of the toughness curve of the tempered cylinder would duplicate that of the design curve. The invalid data points at −46, −18, and 10° C (−50, 0, and 50° F) for the material tempered at 650° C suggested that this tempering temperature was too high to provide a material whose fracture toughness met the solid line in Fig. 6.24. However, the valid K_{Ic} values obtained at −46 and 10° C suggest that the 595° C temper was too low. Figure 6.24 shows that a number of the specimens previously reported as valid are invalid when the geometric requirements of ASTM Standard E 399 are considered.[11]

As indicated earlier in this section, the static fracture toughness properties of the thermal shock cylinder were much lower at ~100° C (210° F) than expected. The experimental results suggest that the toughness did not increase with temperature as projected by the dashed lines in Fig. 6.24 (see Fig. 6.9). This unexpected behavior is further clouded because the three 1T CS machined from material tempered at 600° C (1110° F) and exhibiting high toughness [180 to 220 MPa·$\sqrt{m}$ (165 to 200 ksi$\sqrt{in.}$)] at 38° C (100° F) failed considerably before maximum load was achieved. In the specimen (8SC31) that exhibited 208 MPa·$\sqrt{m}$ (189 ksi$\sqrt{in.}$) at 38° C (100° F), the dimple fracture zone at the crack tip was only 0.25 mm (0.01 in.), a crack extension value that is similar to those used when plotting the blunting line in an R-curve determination in accordance with the procedures suggested by Clarke et al.[12] This information suggests that, although the test is invalid in accordance with ASTM Standard E 399, the specimen did undergo very little ductile tearing prior to fast fracture and some credibility can be placed on that test result. Figure 6.25 contains the scanning electron microscopy (SEM) results obtained from the fractured surface of specimen 8SC31. The region of dimple fracture, which is evident at the fracture initiation area, averages about 0.25 mm (0.01 in.) in width. Figure 6.26 contains the results of an SEM

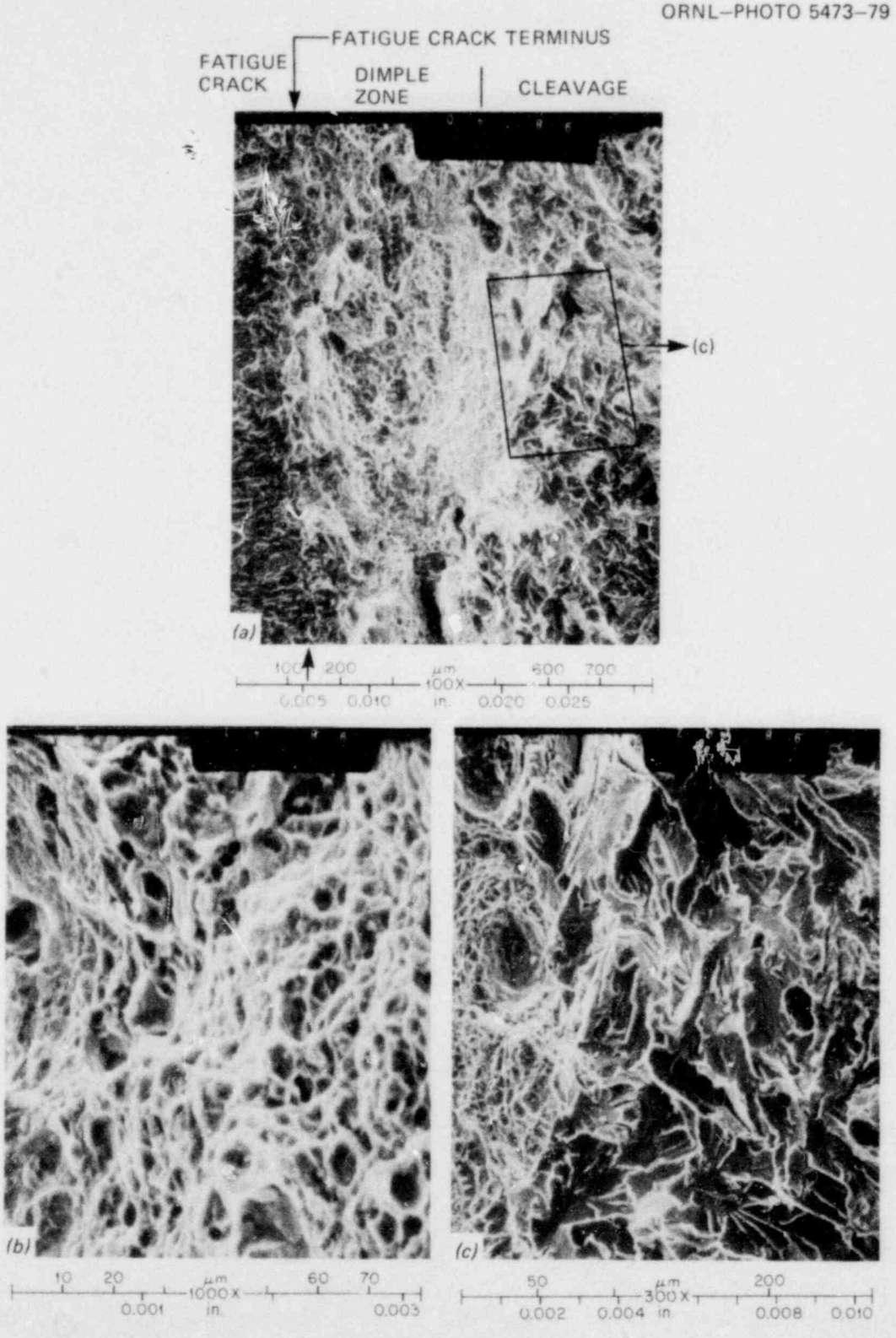

Fig. 6.25. SEM photomicrographs of fracture surface from 1T compact specimen 8SC31 tested at 38°C with a fracture toughness of 208 MPa·$\sqrt{m}$. (a) Fracture morphology at crack propagation site. Initial fracture, which extends for an average of about 0.25 mm, is dimple mode, at which point the continued fracture is by cleavage mode; (b) dimple mode fracture at site of crack initiation; (c) cleavage fracture after dimple fracture. Original reduced 19%.

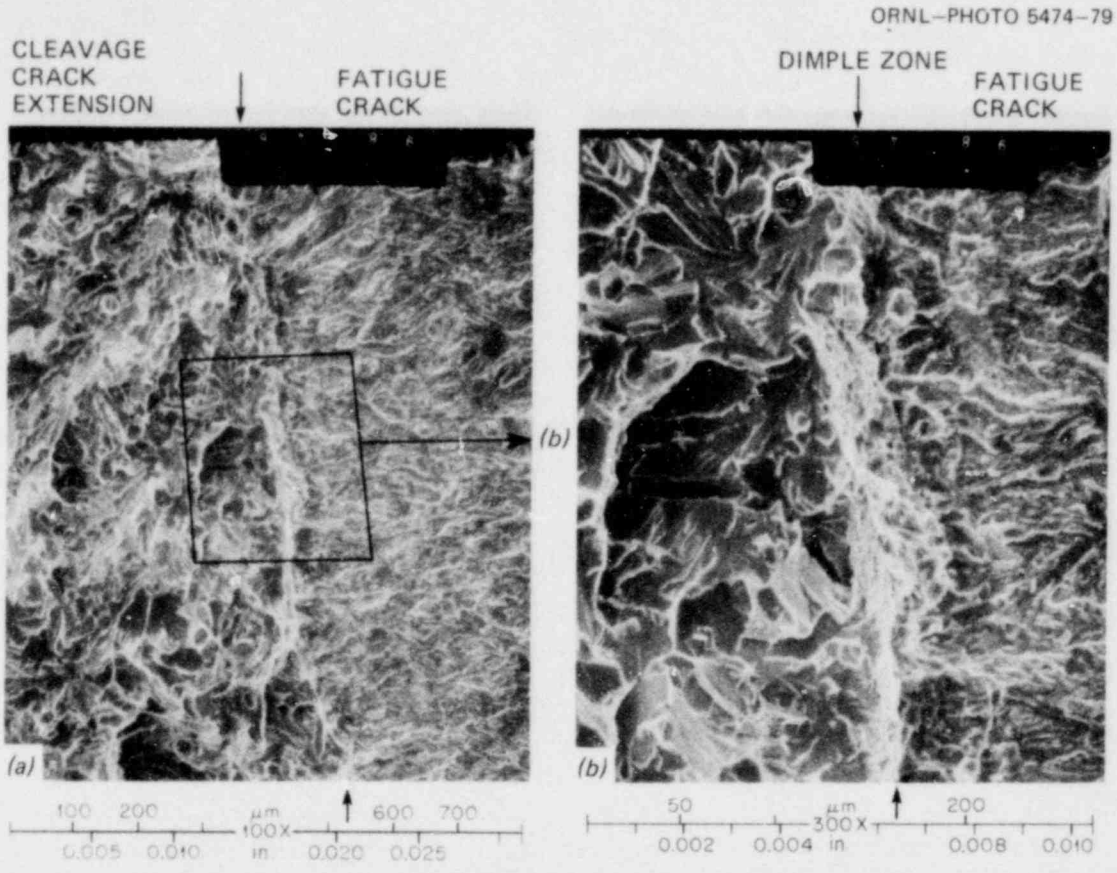

Fig. 6.26. SEM photomicrographs of fracture surface from 1T compact specimen 9SC1 tested at 38°C with a fracture toughness of 98 MPa·$\sqrt{m}$. (a) Fracture morphology at site of crack extension. There is limited dimple mode failure (0.038 mm) prior to the onset of cleavage fracture; (b) region of ductile fracture (dimple mode). Original reduced 15.5%.

study of the same material also tested at 38°C—specimen 9SC1, which exhibited 98 MPa·$\sqrt{m}$ (189 ksi$\sqrt{in.}$); it, too, is invalid because of geometric considerations. However, in this test, the load-displacement curve satisfies that validity criterion in Standard E 399; the width of the dimple band at the fracture site [0.038 mm (0.0015 in.)] indicates a near (if not actual) plane-strain condition at fracture. There is more than a factor of 2 difference in the toughness exhibited by specimens 8SC31 and 9SC1 at the same temperature. Figure 6.27 is included to show the SEM results from a valid test. This specimen, 8SC4, was tested at −46°C (−50°F) and exhibited a toughness of 41 MPa·$\sqrt{m}$ (37 ksi$\sqrt{in.}$). No measurable dimple mode fracture occurs at the initiation site; this is truly a plane-strain failure.

While the specimens were in the SEM, chemical analysis of the dimple region in specimens 9SC1 and 8SC31 was made with an Energy Dispersive Analyzer (EDA). No detectable (within the limits of the EDA) difference was apparent in the chemical composition at the fracture initiation site in the two specimens.

An examination of the microstructure and microhardness near the fracture initiation site was undertaken in an effort to explain the extreme differences in the fracture toughness of the specimens tested at 38°C (100°F). Figure 6.28 contains photomicrographs and hardness readings near the fracture initiation sites in specimens 9SC1 and 8SC31. Although these two specimens exhibited quite different fracture toughness, their microhardness and microstructures are quite similar.

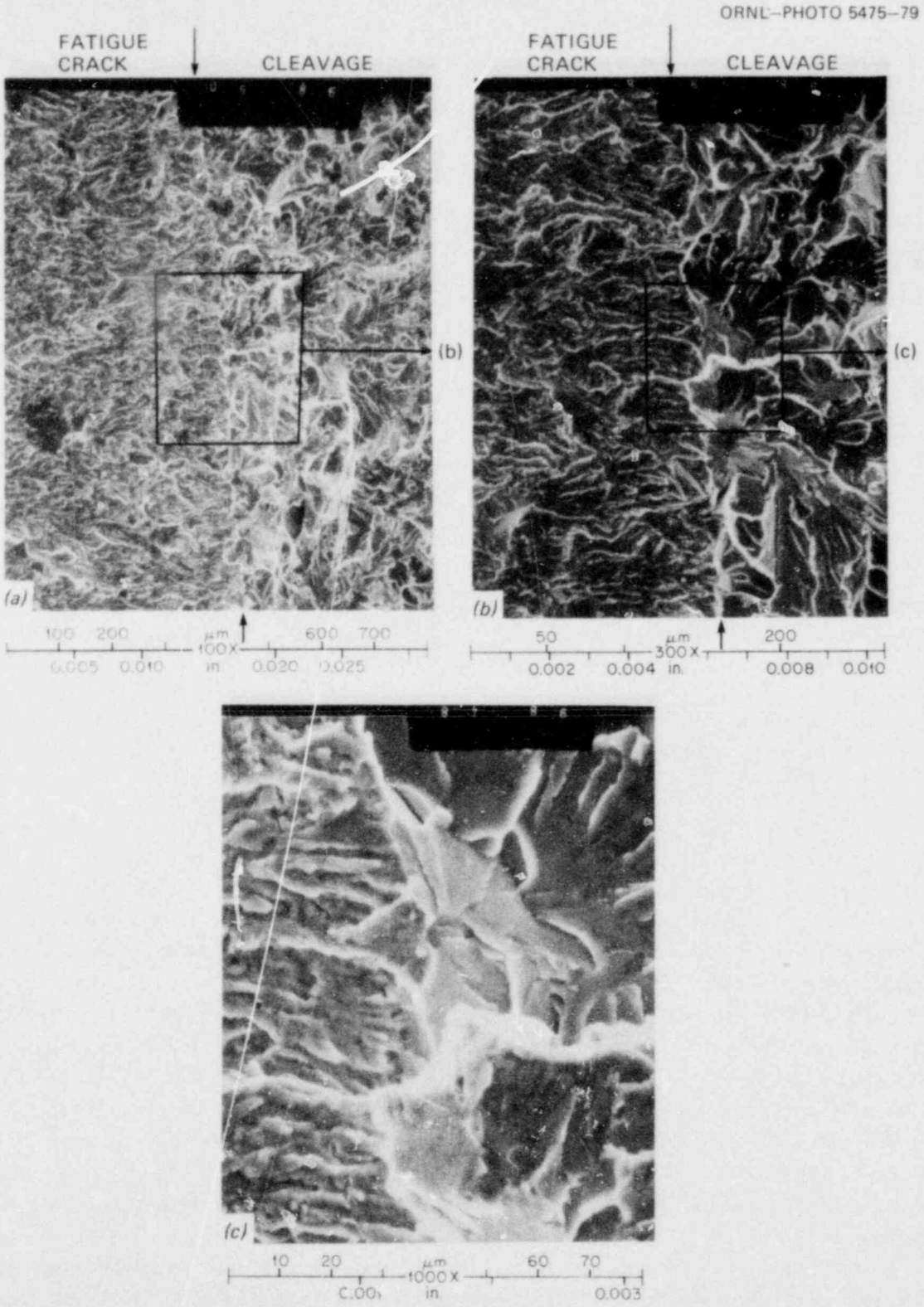

Fig. 6.27. SEM photomicrographs of 1T compact specimen 8SC4 tested at −46° C with a fracture toughness of 41 MPa·$\sqrt{m}$. (a) Site of fracture initiation. There is no evidence of ductile fracture at the terminus of the fatigue crack, as confirmed at higher magnifications in (b) and (c). Original reduced 16.5%.

ORNL–PHOTO 5476–79

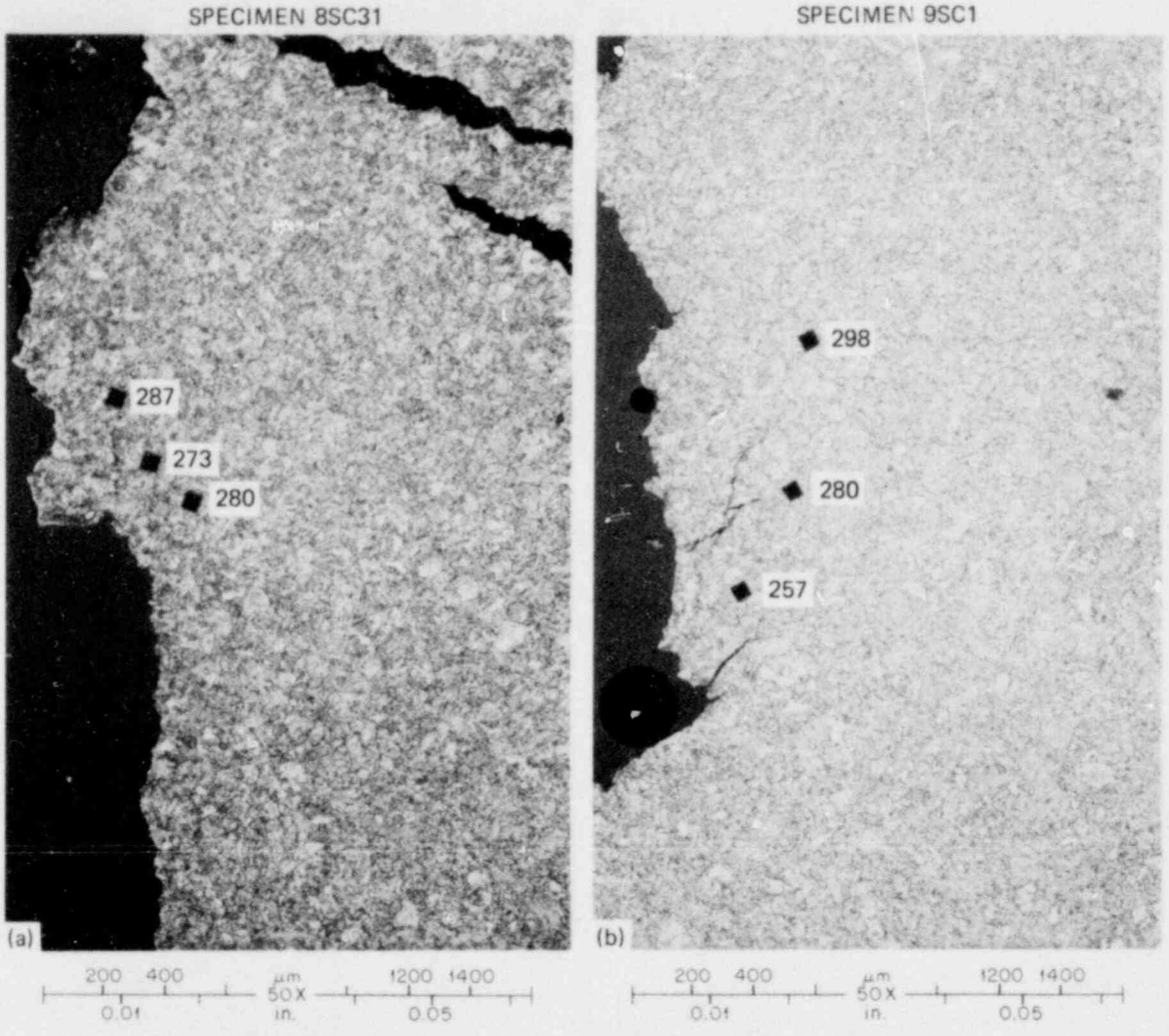

Fig. 6.28. Results of microhardness tests near fracture initiation sites in 1T compact specimens 8SC31 and 9SC1. These specimens, which were tested at 38°C, exhibited 208 and 98 MPa·$\sqrt{m}$, respectively. (a) 1T compact specimen 8SC31; (b) 1T compact specimen 9SC1. Numbers shown on photomicrographs are diamond pyramid hardness values for associated indentations. Indentor load was 9.8 N (1000 g). Original reduced 18.5%.

References

1. P. P. Holz, "TSC-1 Flawing Development," *Heavy-Section Steel Technology Program Quart. Prog. Rep. April-June 1979*, NUREG/CR-0980 (ORNL/NUREG/TM-347), pp. 67–68.

2. R. D. Cheverton, "Thermal Shock Investigations," *Heavy-Section Steel Technology Program Quart. Prog. Rep. January-March 1979*, NUREG/CR-0818 (ORNL/NUREG/TM-342), pp. 91–94.

3. R. D. Cheverton and S. E. Bolt, *Pressure Vessel Fracture Studies Pertaining to a PWR LOCA-ECC Thermal Shock: Experiments TSE-3 and TSE-4 and Update of TSE-1 and TSE-2 Analysis*, ORNL/NUREG-22 (December 1977).

4. R. D. Cheverton, "Thermal Shock Investigations," *Heavy-Section Steel Technology Program Quart. Prog. Rep. April-June 1979*, NUREG/CR-0980 (ORNL/NUREG/TM-347), pp. 63–67.

5. R. D. Cheverton, "Thermal Shock Investigations," *Heavy-Section Steel Technology Program Quart. Prog. Rep. April-June 1979*, NUREG/CR-0980 (ORNL/NUREG/TM-347).

6. W. O. Shabbits et al., *Heavy-Section Steel Technology Program Technical Report No. 6, Heavy-Section Fracture Toughness Properties of A533 Grade B Class 1 Steel Plate and Submerged-Arc Weldment*, WCAP-7414 (December 1969).

7. *ASME Boiler and Pressure Vessel Code*, Section XI, Appendix A.

8. Flaw Evaluation Procedures: ASME Section XI, EPRI NP-719-SR, pp. 0–2 (August 1978).

9. R. D. Cheverton, "Thermal Shock Investigations," *Heavy-Section Steel Technology Program Quart. Prog. Rep. July–September 1978*, NUREG/CR-0476 (ORNL/NUREG/TM-275), pp. 81–82.

10. R. D. Cheverton, *Pressure Vessel Fracture Studies Pertaining to a PWR LOCA-ECC Thermal Shock: Experiments TSE-1 and TSE-2*, ORNL/NUREG/TM-31 (September 1976), p. 45.

11. W. J. Stelzman and D. A. Canonico, "Thermal Shock Temper Study," *Heavy-Section Steel Technology Program Quart. Prog. Rep. April–June 1979*, ORNL/NUREG/TM-347, pp. 68–73.

12. G. A. Clarke et al., "A Procedure for the Determination of Ductile Fracture Toughness Values Using J-Integral Techniques," *J. Test. Eval.* **7**(1), 49-56 (January 1979).

Appendix A

INDIVIDUAL RESULTS FOR FATIGUE SPECIMEN TESTS COMPLETED DURING THIS REPORT PERIOD

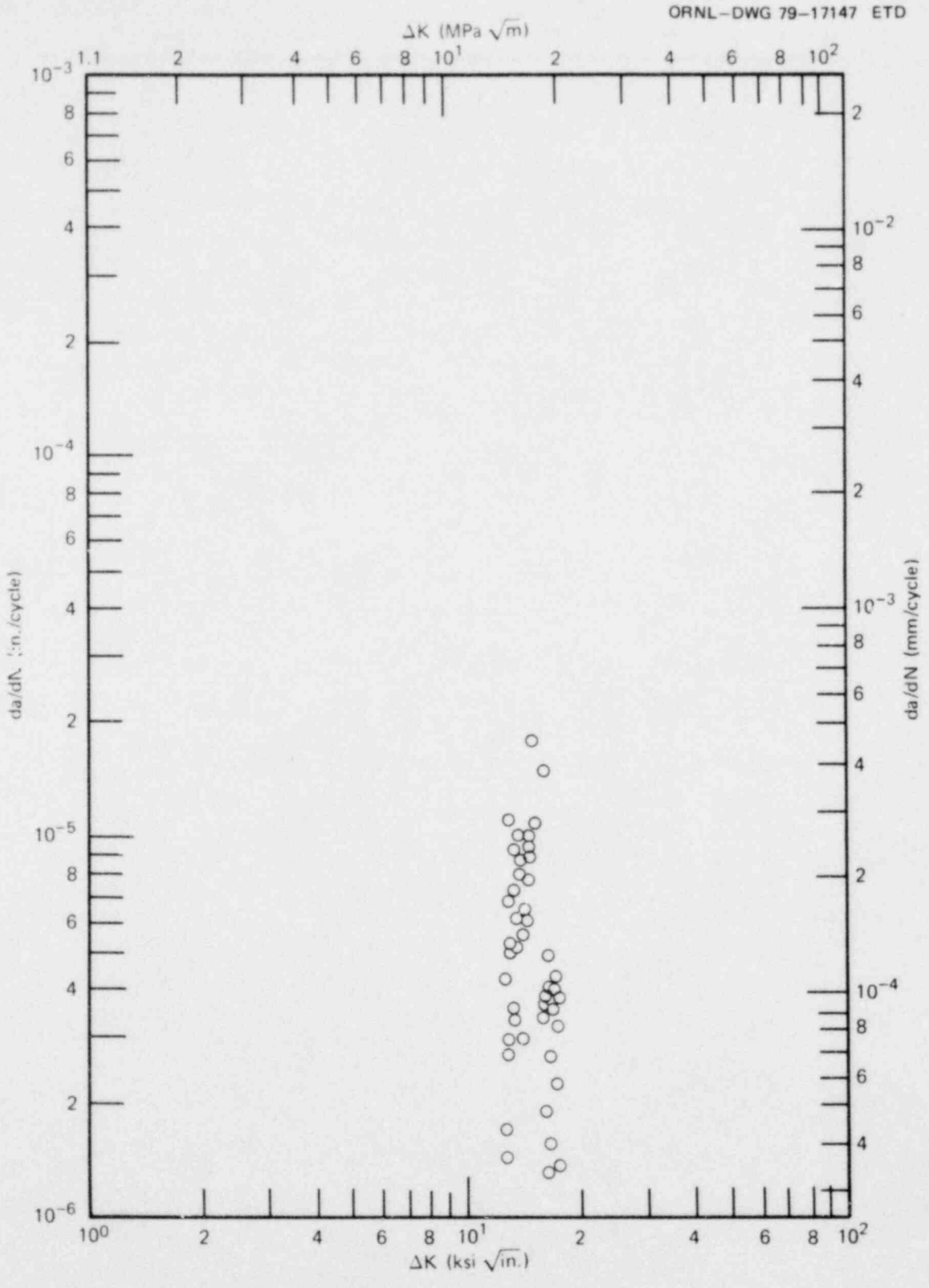

Fig. A.1. Crack growth rate test results for specimen C8.

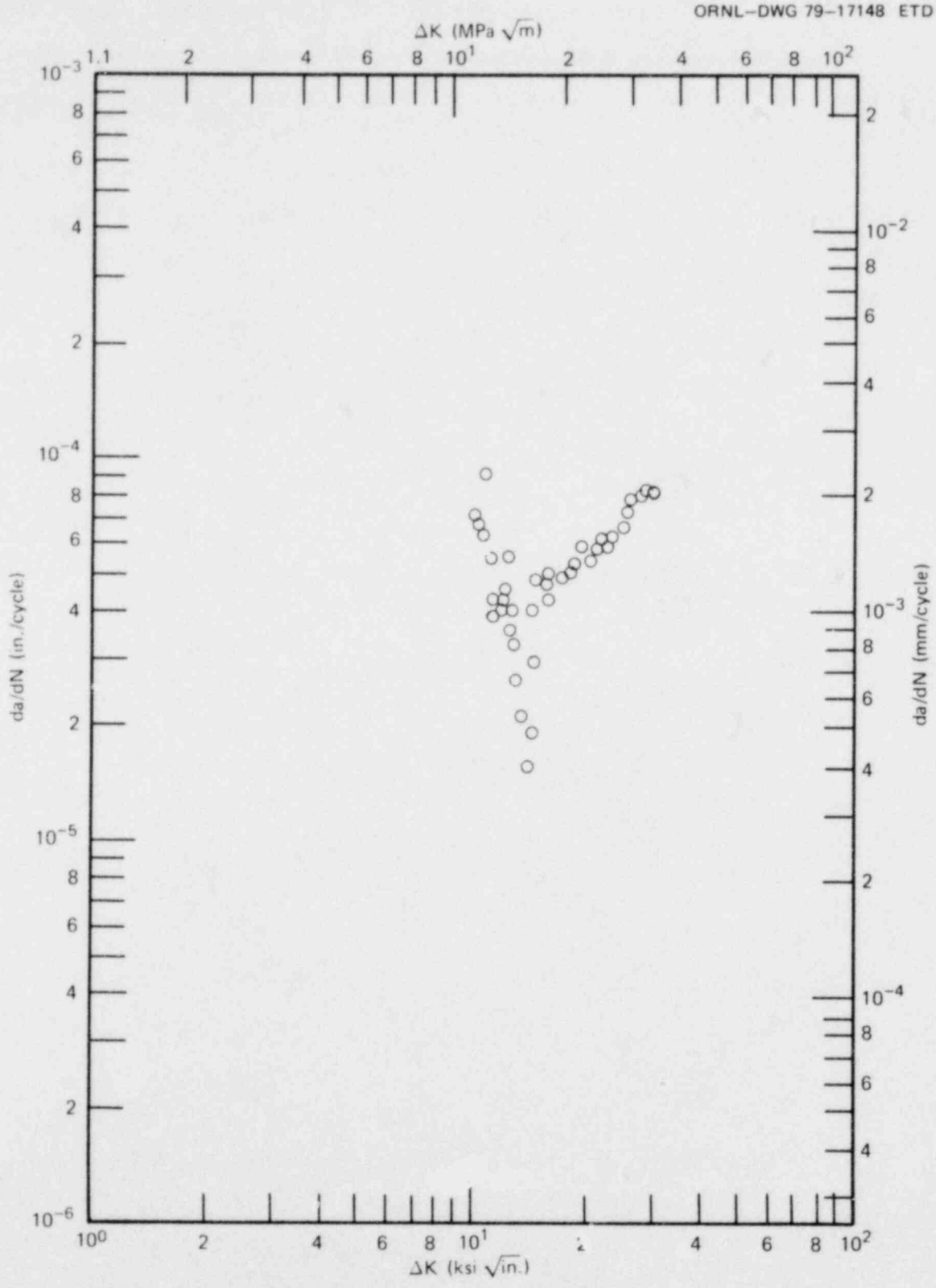

Fig. A.2. Crack growth rate test results for specimen C10.

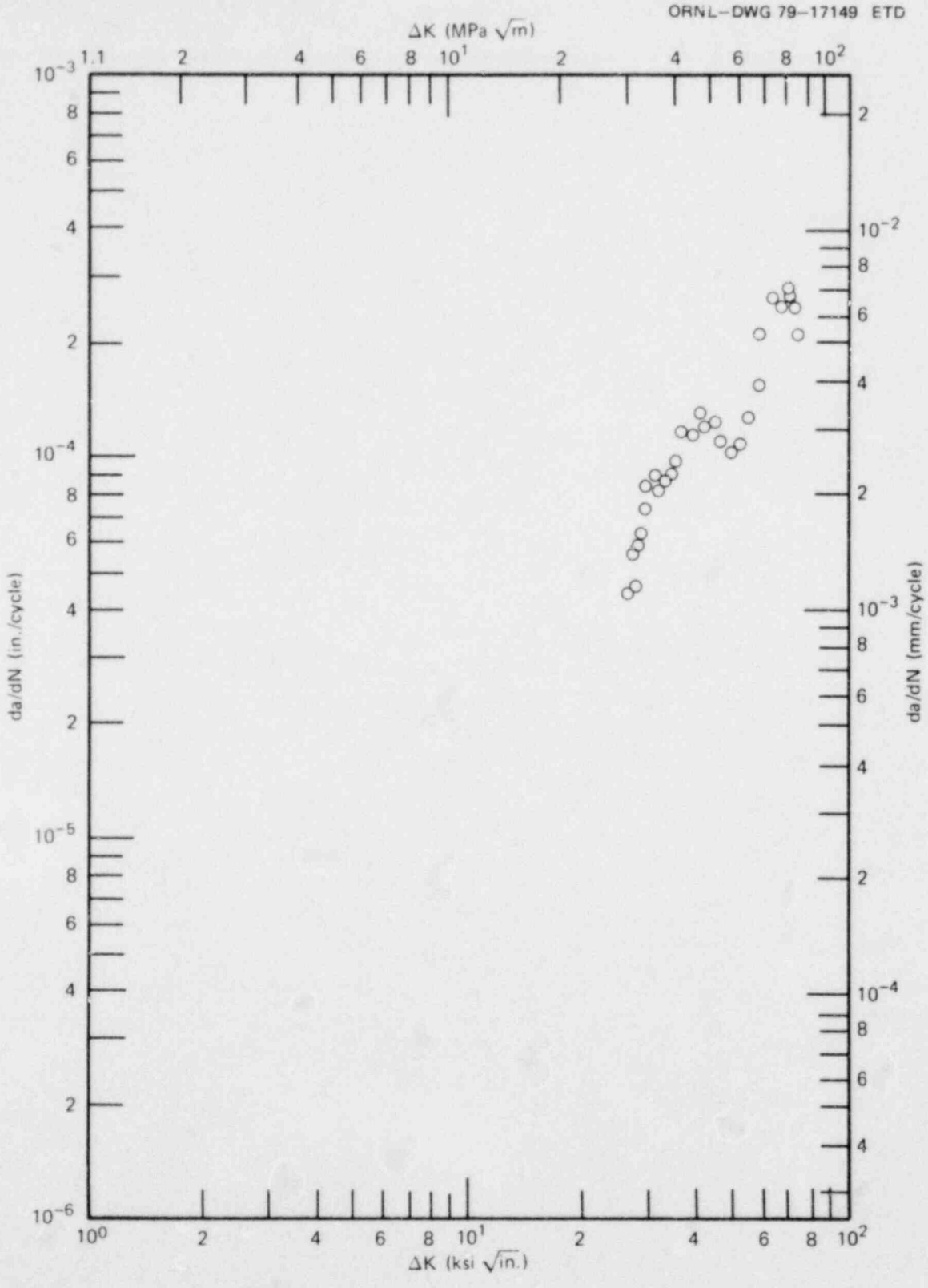

Fig. A.3. Crack growth rate test results for specimen C24 HAZ 1.

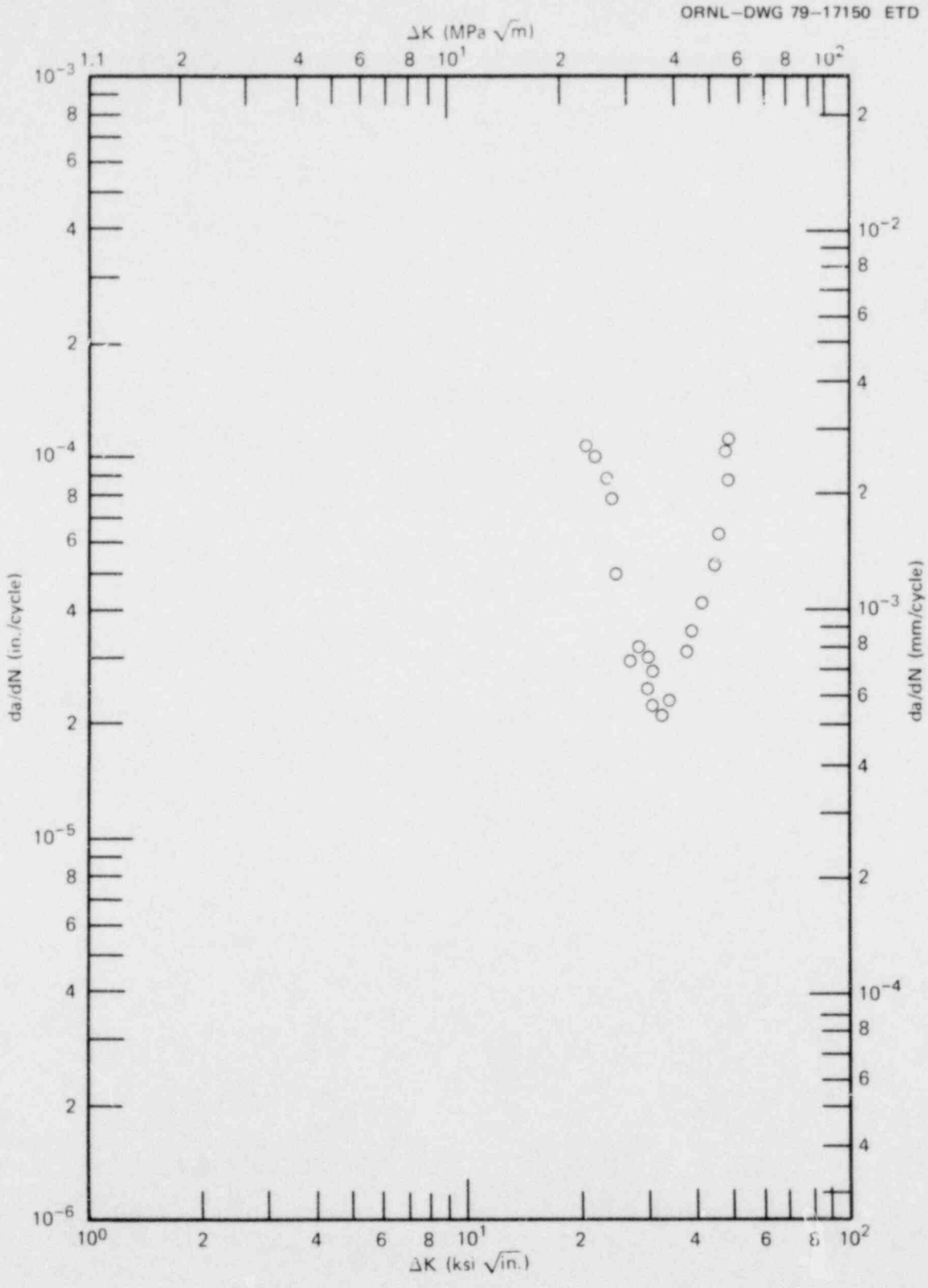

Fig. A.4. Crack growth rate test results for specimen C1 WLD.

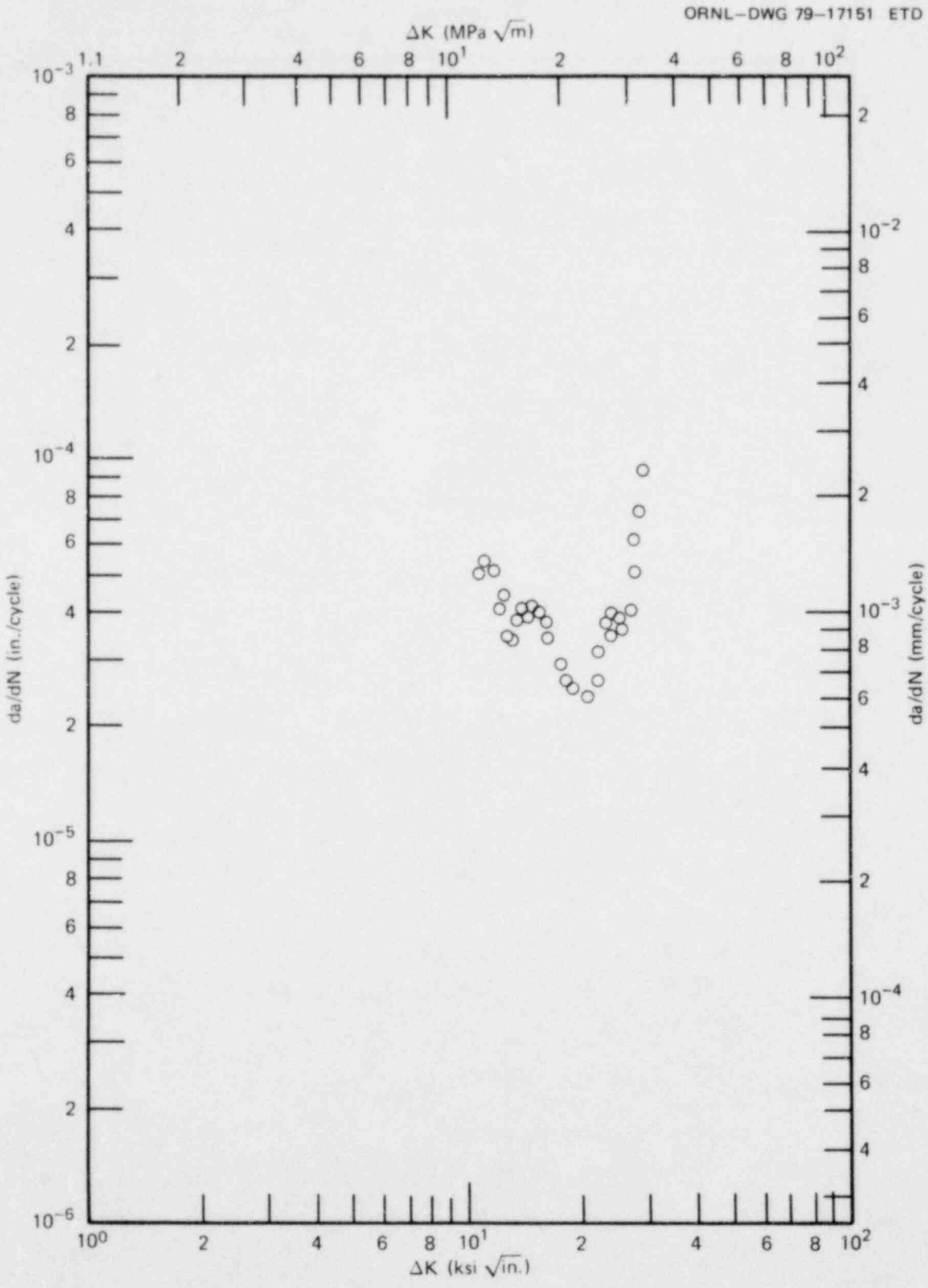

Fig. A.5. Crack growth rate test results for specimen C2 WLD.

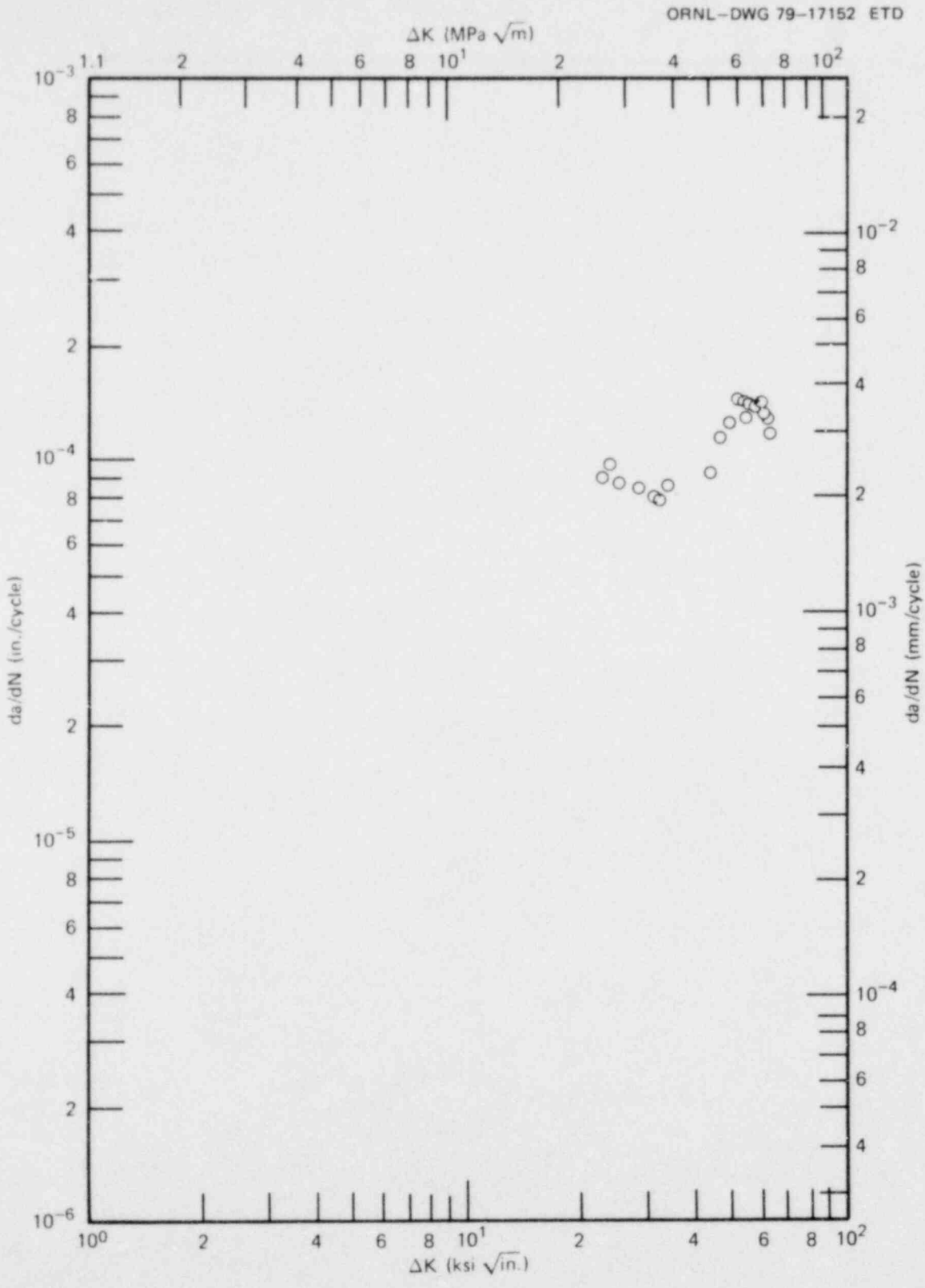

Fig. A.6. Crack growth rate test results for specimen C3 WLD.

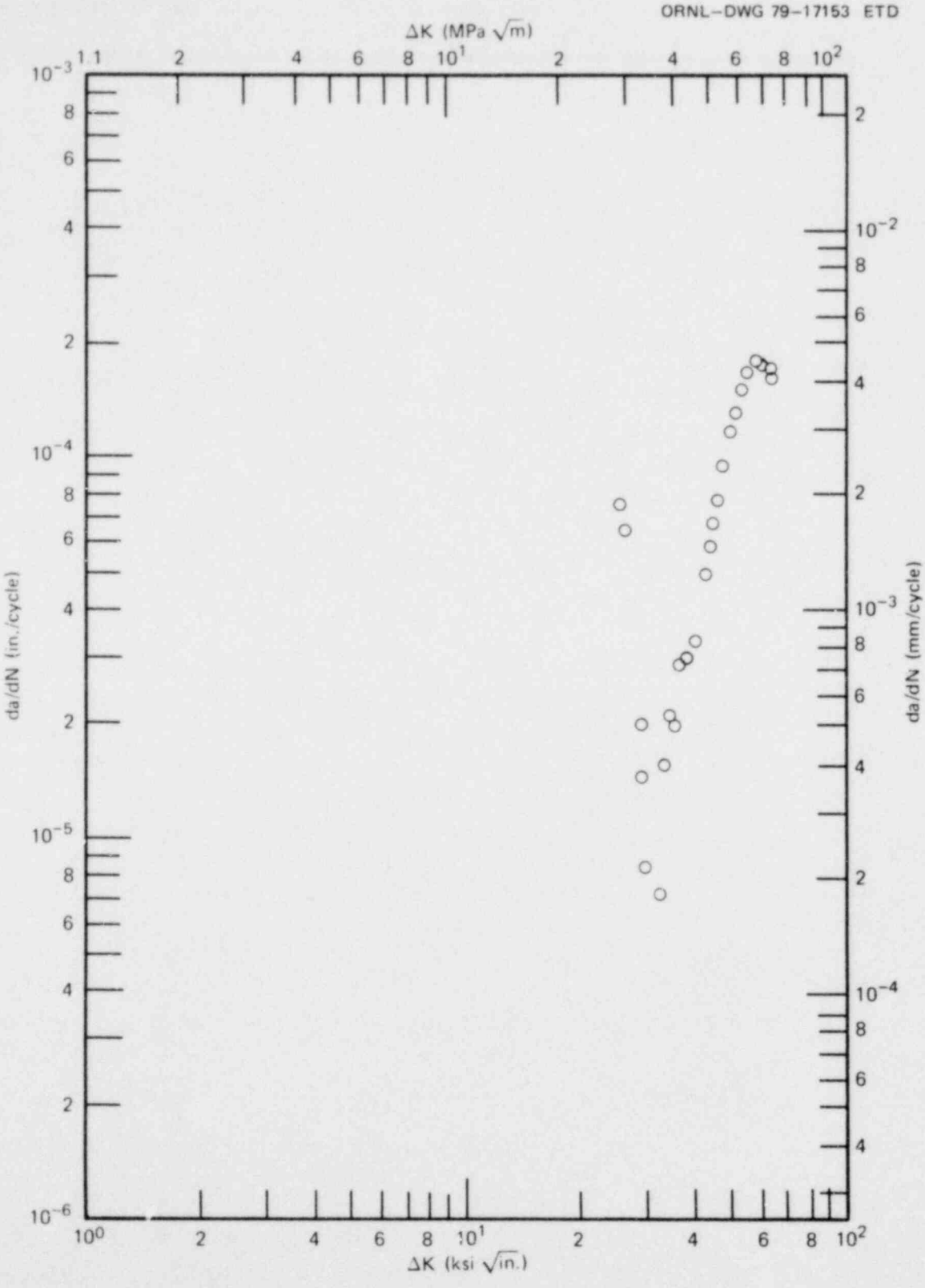

Fig. A.7. Crack growth rate test results for specimen C1 HAZ.

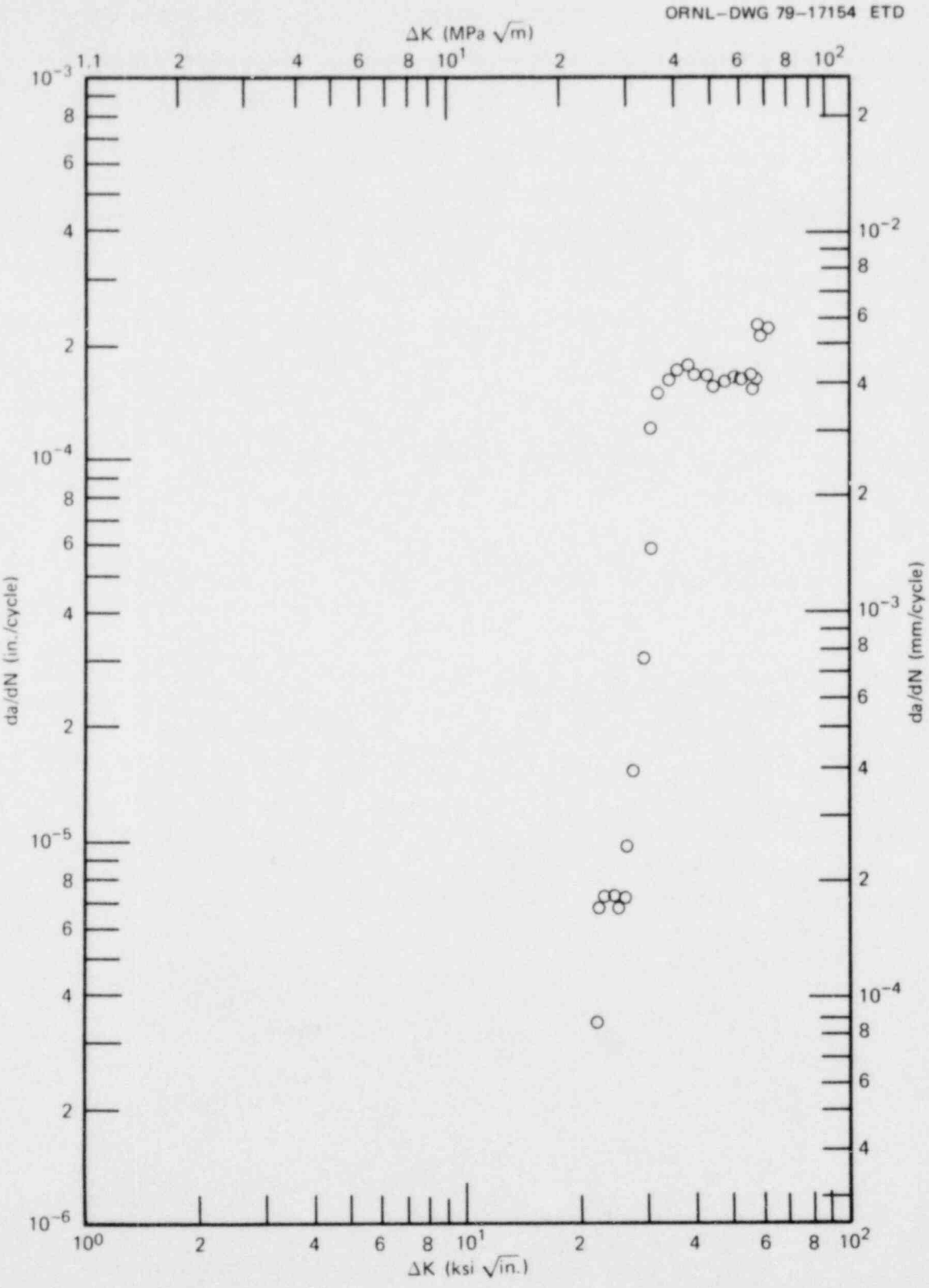

Fig. A.8. Crack growth rate test results for specimen 04AE11.

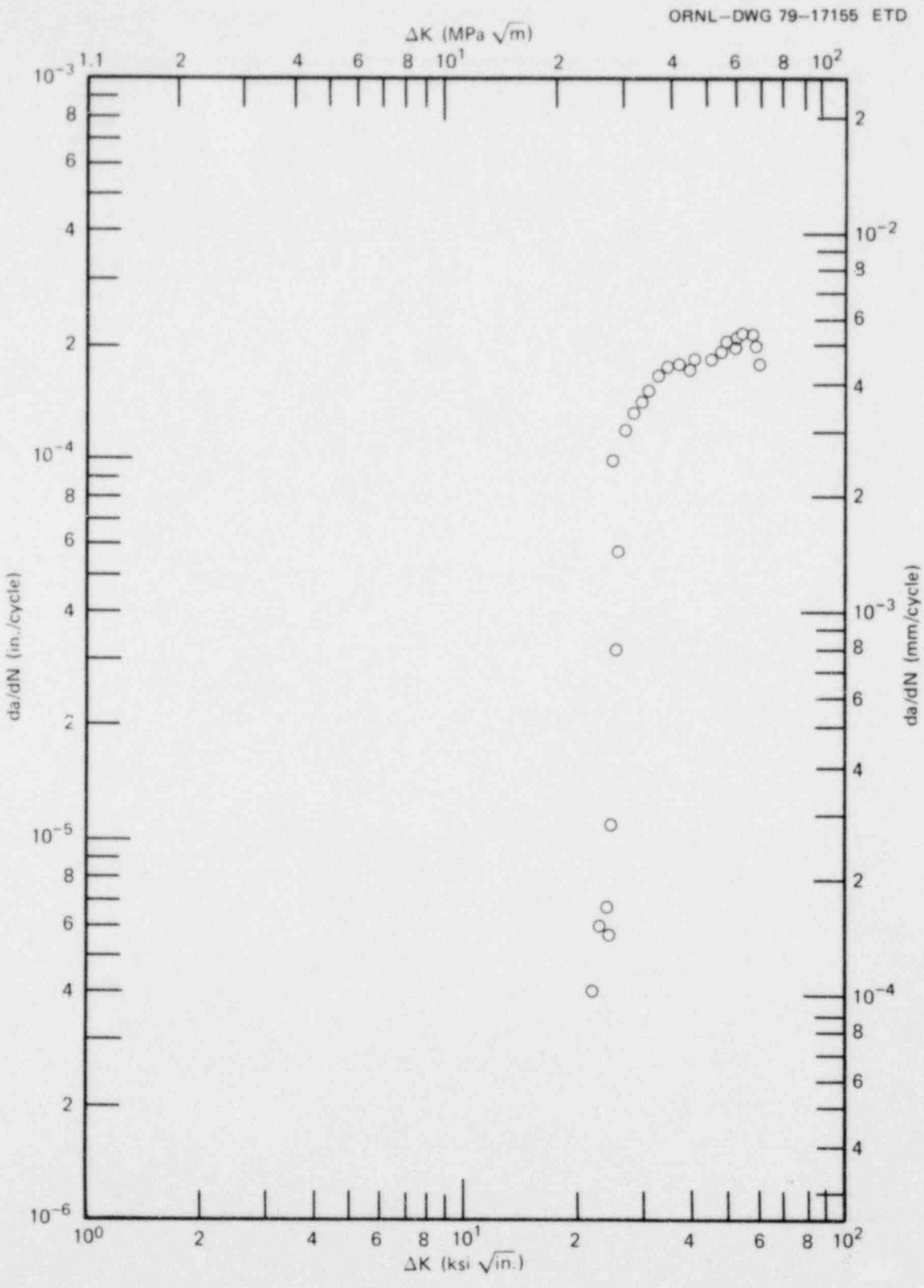

Fig. A.9. Crack growth rate test results for specimen 04AE12.

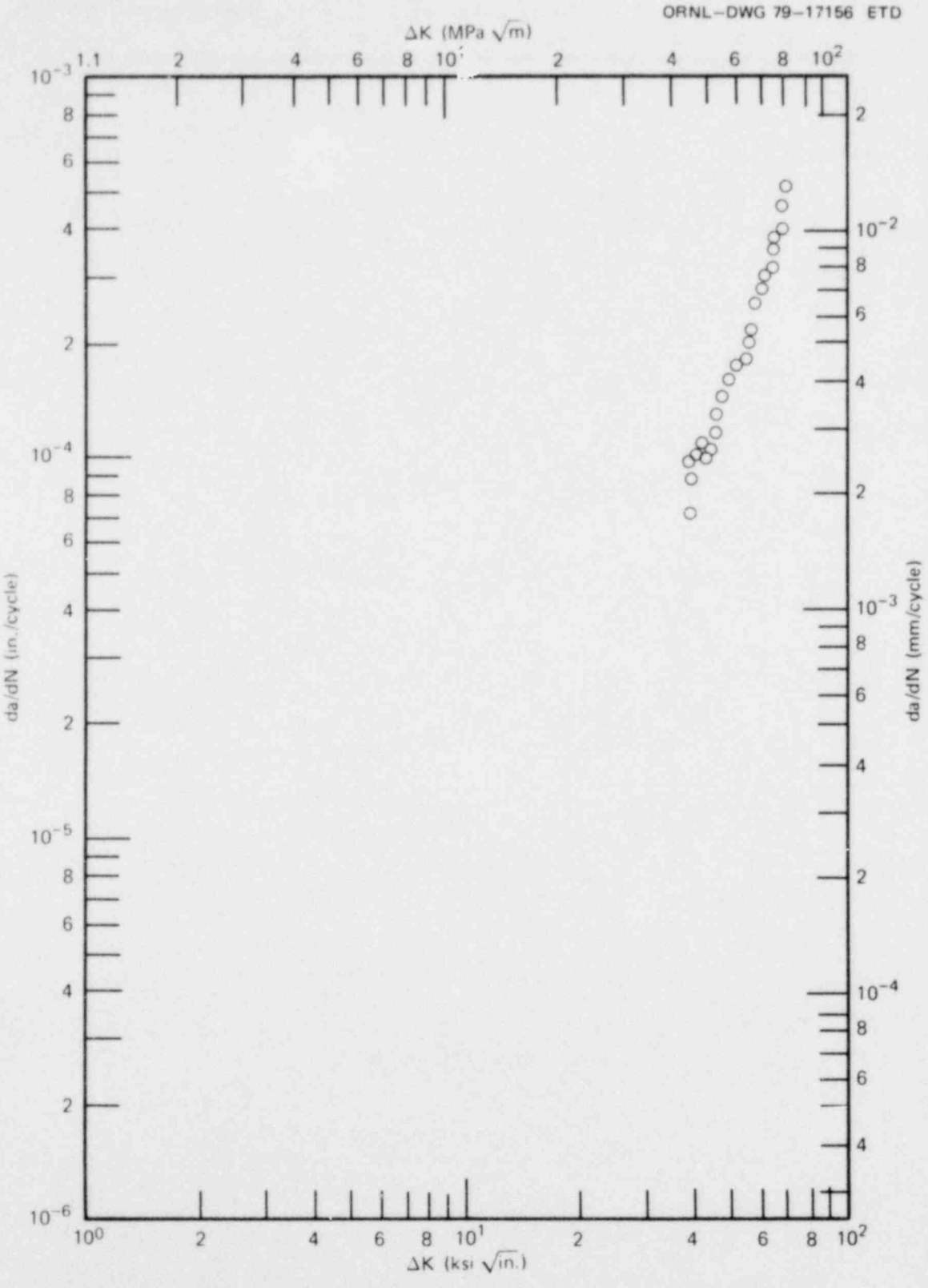

Fig. A.10 Crack growth rate test results for specimen 04AE13.

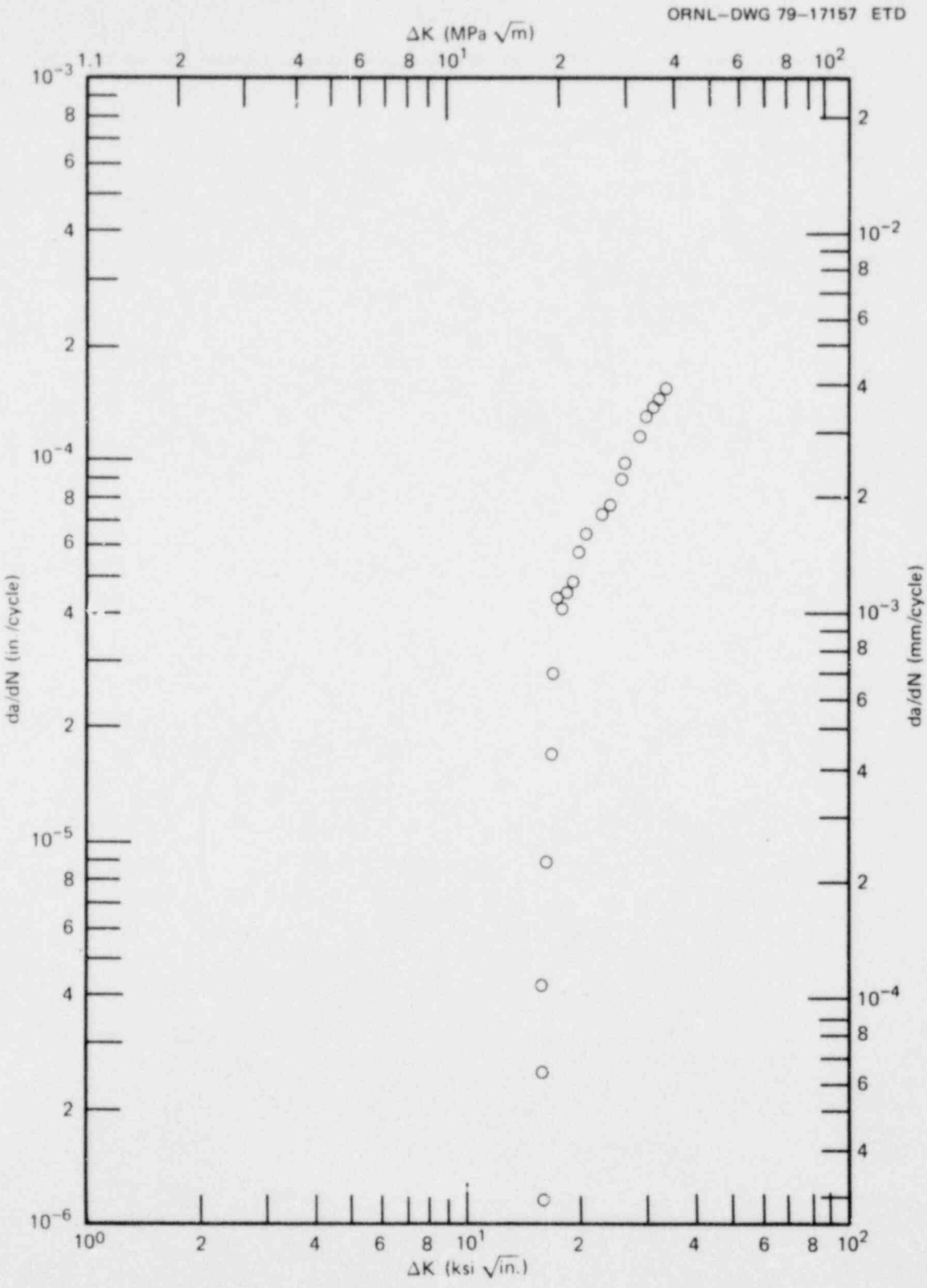

Fig. A 11. Crack growth rate test results for specimen 04AE14.

Conversion Factors[a]

SI unit	English unit	Factor
mm	in.	0.0393701
cm	in.	0.393701
m	ft	3.28084
m/s	ft/s	3.28084
kN	lb_f	224.809
kPa	psi	0.145038
MPa	ksi	0.145038
$MN \cdot m^{-3/2}$ ($MPa \cdot \sqrt{m}$)	$ksi\sqrt{in.}$	0.910048
J	ft-lb	0.737562
K	°F or °R	1.8
kJ/m^2	$in.\text{-}lb/in.^2$	5.71015
$W \cdot m^{-2} \cdot K^{-1}$	$Btu/hr\text{-}ft^2\text{-}°F$	0.176110
$T(°F) = 1.8\ T(°C) + 32$		

[a]Multiply SI quantity by given factor to obtain English quantity.

NUREG/CR-1197
ORNL/NUREG/TM-370
Dist. Category RF

Internal Distribution

1. R. G. Beiggren
2. S. E. Bolt
3-7. R. H. Bryan
8. J. W. Bryson
9. D. A. Canonico
10-14. R. D. Cheverton
15. J. M. Corum
16. W. B. Cottrell
17. W. L. Greenstreet
18. R. C. Gwaltney
19. P. P. Holz
20. S. K. Iskander
21. K. K. Klindt
22-25. J. G. Merkle
26. C. A. Mills
27. S. E. Moore
28. F. R. Mynatt
29. D. J. Naus
30. F. H. Neill
31. J. L. Rich
32. G. C. Robinson
33. G. M. Slaughter
34. J. E. Smith
35. W. J. Stelzman
36. H. E. Trammell
37-41. G. D. Whitman
42. ORNL Patent Office
43-44. Central Research Library
45. Document Reference Section
46. Laboratory Records Department
47. Laboratory Records (RC)

External Distribution

48. C. Z. Serpan, Reactor Safety Research, Nuclear Regulatory Commission, Washington, DC 20555
49. M. Vagins, Reactor Safety Research, Nuclear Regulatory Commission, Washington, DC 20555
50. Office of Assistant Manager, Energy Research and Development, DOE, ORO
51–52. Technical Information Center, DOE
53–462. Given distribution as shown in category RF (NTIS—10)

☆U.S. GOVERNMENT PRINTING OFFICE: 1980-640-245/004